Breaking Ground on the Moon and Mars:

Reconstructing Lunar Tectonic Evolution and Martian Central Pit Crater Formation

by

Nathan Robert Williams

A Dissertation Presented in Partial Fulfillment
of the Requirements for the Degree
Doctor of Philosophy

Approved April 2016 to the
Graduate Supervisory Committee:

James Bell, Chair
Mark Robinson
Philip Christensen
Jack Farmer
Manoochehr Shirzaei

ARIZONA STATE UNIVERSITY

May 2016

ABSTRACT

Understanding the structural evolution of planetary surfaces provides key insights to their physical properties and processes. On the Moon, large-scale tectonism was thought to have ended over a billion years ago. However, new Lunar Reconnaissance Orbiter Camera (LROC) Narrow Angle Camera (NAC) high resolution images show the Moon's surface in unprecedented detail and show many previously unidentified tectonic landforms, forcing a re-assessment of our views of lunar tectonism. I mapped lobate scarps, wrinkle ridges, and graben across Mare Frigoris – selected as a type area due to its excellent imaging conditions, abundance of tectonic landforms, and range of inferred structural controls. The distribution, morphology, and crosscutting relationships of these newly identified populations of tectonic landforms imply a more complex and longer-lasting history of deformation that continues to today. I also performed additional numerical modeling of lobate scarp structures that indicates the upper kilometer of the lunar surface has experienced 3.5-18.6 MPa of differential stress in the recent past, likely due to global compression from radial thermal contraction.

Central pit craters on Mars are another instance of intriguing structures that probe subsurface physical properties. These kilometer-scale pits are nested in the centers of many impact craters on Mars as well as on icy satellites. They are inferred to form in the presence of a water-ice rich substrate; however, the process(es) responsible for their formation is still debated. Previous models invoke origins by either explosive excavation of potentially water-bearing crustal material, or by subsurface drainage of meltwater and/or collapse. I assessed radial trends in grain size around central pits using thermal inertias calculated from Thermal Emission Imaging System (THEMIS) thermal infrared

images. Average grain size decreases with radial distance from pit rims – consistent with pit-derived ejecta but not expected for collapse models. I present a melt-contact model that might enable a delayed explosion, in which a central uplift brings ice-bearing substrate into contact with impact melt to generate steam explosions and excavate central pits during the impact modification stage.

ACKNOWLEDGMENTS

TABLE OF CONTENTS

LIST OF FIGURES

INTRODUCTION

Examination of landforms on planetary surfaces provides critical insight to fundamental geologic processes under a wider range of conditions than is observable on Earth. Extensive remote sensing of our solar system via robotic exploration is providing a wealth of information to assess geologic and environmental histories across the eons. This dissertation examines specific landform structures to address fundamental questions about the properties and processes responsible for surface deformation on the Moon and Mars. Where do these features occur? When did they form? What are the driving forces involved?

First, I examine the distribution and timing of tectonism on the Moon. Nearside basin-related extensional tectonism on the Moon was thought to have ended by about 3.6 billion years ago and mare basin-localized contractional deformation ended by about 1.2 billion years ago. Lunar Reconnaissance Orbiter Camera (LROC) high resolution (50-200 cm/pixel) images show the Moon's surface in unprecedented detail and have enabled us to find many previously unidentified tectonic landforms, forcing a re-assessment of our views of tectonism in the maria. The morphology and stratigraphic relationships of these newly identified populations of tectonic landforms imply a more complex and longer-lasting history of deformation. I selected Mare Frigoris as an ideal location to perform a mapping survey where excellent imaging conditions, abundant tectonic landforms, and restricted mascon allow us to unravel the mare's tectonic evolution. Similar to previous surveys, I find that tectonism in the eastern basin of Mare Frigoris was controlled by ancient mascon induced flexure. In the western basin, however, I identify a parallel set of ancient compressional wrinkle ridges across the basin that is inconsistent with an origin

by basin-centric mascon flexure or influence from the Mare Imbrium mascon. Instead, my results imply an ancient, regional, non-isotropic stress field over western Mare Frigoris. I also identify young wrinkle ridges and show that they have likely been active within the last 1 billion years, and some ridges as recently as within 40 million years. Finally, I identify a 300 km long series of lobate scarps coincident with one of the shallow moonquakes recorded during Apollo and use geodetic strain from the mapped global population of young lobate scarps to predict a level of seismicity consistent with the shallow moonquakes recorded during Apollo. In tandem with similarly young lobate scarps and small graben, as well as recorded shallow moonquakes, these young wrinkle ridges imply that some tectonism in and around Mare Frigoris has occurred in the geologically recent past and likely still continues today.

Second, I model the subsurface geometry of compressional lobate scarp faults and near-surface stress state of the Moon. Before the launch of the Lunar Reconnaissance Orbiter (LRO), known characteristics of lobate scarps on the Moon were limited to studies of only a few dozen scarps revealed in Apollo-era photographs within ~20° of the equator. The Lunar Reconnaissance Orbiter Camera (LROC) now provides meter-scale images of more than 100 lobate scarps, as well as stereo derived topography of about a dozen scarps. High resolution digital terrain models (DTMs) provide unprecedented insight into scarp morphology and dimensions. Here, I analyze images and DTMs of the Slipher, Racah X-1, Mandel'shtam A, Feoktistov, Simpelius-1, and Oppenheimer F lobate scarps. Parameters in fault dislocation models are iteratively varied to provide best fits to DTM topographic profiles to test previous interpretations that the observed landforms are the result of shallow, low-angle thrust faults. Results suggest that these

2

faults occur from the surface down to depths of hundreds of meters, have dip angles of

35-40°, and have typical maximum slips of tens of meters. These lunar scarp models are

comparable to modeled geometries of lobate scarps on Mercury, Mars, and asteroid 433

Eros, but are shallower and ~10° steeper than geometries determined in studies with

limited Apollo-era data. Frictional and rock mass strength criteria constrain the state of

global differential stress between 3.5 and 18.6 MPa at the modeled maximum depths of

faulting. My results are consistent with thermal history models that predict relatively

small compressional stresses that likely arise from cooling of a magma ocean.

Third, I investigate the morphologic and thermophysical characteristics of central

pit craters on Mars. Kilometer-scale pits are nested in the centers of many impact craters

on Mars as well as on icy satellites. They have been inferred to form in the presence of a

water-ice rich substrate; however, the process(es) responsible for their formation is still

debated. Previous models invoke origins by either explosive excavation of potentially

water-bearing crustal material, or by subsurface drainage of meltwater and/or collapse. If

explosive excavation forms central pits, pit-derived ejecta should be draped around the

pits, whereas internal collapse should not deposit significant material outside pit rims.

Using visible wavelength images from the Mars Reconnaissance Orbiter (MRO) Context

Camera (CTX) and High Resolution Imaging Science Experiment (HiRISE) instruments

and thermal infrared images from the Odyssey Thermal Emission Imaging System

(THEMIS) instrument, I conducted a survey to characterize, in detail, the global

population of central pits in impact craters ≥10 km in diameter. I specifically examined

the morphology and thermophysical characteristics of the pits for evidence of pit ejecta.

My analysis of thermal images suggests that coarse-grained materials are distributed

proximally around many central pits on the floors of their host craters. The decrease in average grain size with distance from pit rims is consistent with pit-derived ejecta. These observations and interpretations better support an explosive origin for central pits on Mars than they do an origin of subsurface meltwater drainage and collapse of the overlying substrate. A major weakness to previous explosive central pit formation models is the inability for them to form pit late enough in the impact process to be preserved. To address this, I present an alternative "melt contact model" where a central uplift brings ice-bearing substrate into contact with impact melt to generate steam explosions and excavate central pits during the impact modification stage. Theoretical calculations show that more than enough thermal energy is available via impact melt from the host crater to form central pits by steam explosions, and such explosions would require only a modest amount (2-6% by volume) of uplifted water-ice. I therefore propose that central pits on Mars could have formed explosively by the interaction of impact melt and subsurface water-ice.

1. EVIDENCE FOR RECENT AND ANCIENT FAULTING AT MARE FRIGORIS AND IMPLICATIONS FOR LUNAR TECTONIC EVOLUTION

Motivation

Tectonism in the lunar maria was largely thought to be controlled by flexure and induced subsidence to compensate large mascons – or mass concentrations [Melosh, 1978; Solomon and Head, 1979, 1980]. Previous studies also concluded that tectonism in the lunar maria occurred long ago, with extension ceasing by ~3.6 billion years ago and compression by ~1.2 billion years ago [Lucchitta and Watkins, 1978; Solomon and Head, 1979, 1980; Hiesinger et al., 2003]. However, some mare-filled basins that lack large super-isostatic (unequilibrated) mascons are observed to have compressional tectonic landforms that do not conform to the classical mascon-related patterns. Additionally, some mare tectonic landforms have remarkably crisp morphologies not previously observed, suggestive of more recent activity. Understanding the occurrence of these features via their distribution and morphology is therefore essential to reconstructing the thermal-tectonic-magmatic evolution of the Moon.

The enigmatic Mare Frigoris (Fig. 1), located north of Mare Imbrium is an irregularly-shaped large mare basin. The western two-thirds of the basin lack a large super-isostatic load, while the eastern third of the basin has a large central super-isostatic load. Yet, the entire basin exhibits abundant examples of each type of lunar tectonic landform (i.e., wrinkle ridges, lobate scarps, and graben; see details in the following section). Some of the landforms also interact with each other both spatially and temporally, providing greater insight to their respective and sometimes linked origins.

Mare Frigoris's diverse suite of landforms and spatially variable mascon flexure

influence make it an ideal location to study the occurrence of these features. In this study,

I map the tectonic landforms in Mare Frigoris and the adjacent highlands to reconstruct

the tectonic history of Mare Frigoris as a type area – unraveling the distribution, controls,

and timing of tectonic activity to serve as a baseline for understanding its many

analogous tectonic landforms elsewhere on the Moon.
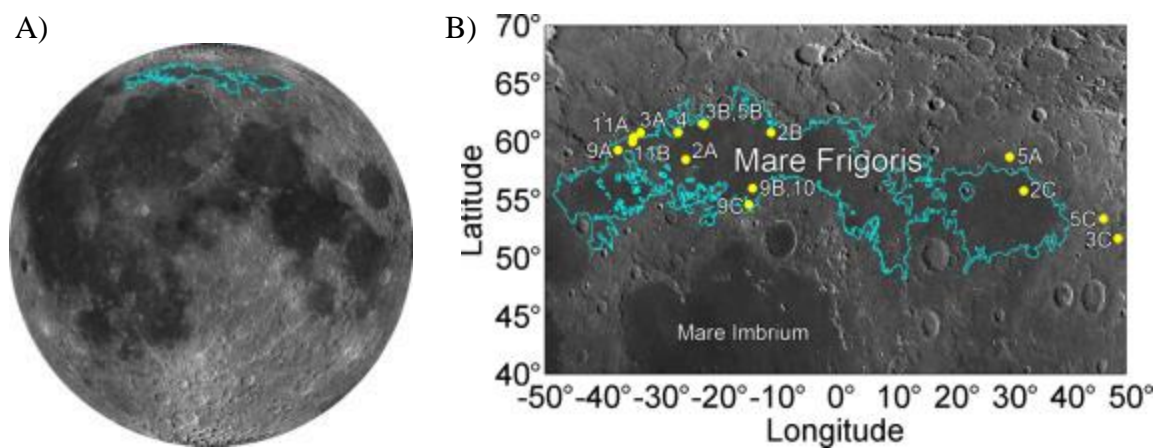
Fig. 1: A) LROC Wide Angle Camera [Robinson et al., 2010] global mosaic orthographic projection centered at the sub-Earth point (0°N, 0°E) showing the location of Mare Frigoris (basin boundary outlined in teal) on the northern nearside [Nelson *et al*., 2014]. B) LROC Wide Angle Camera global mosaic equirectangular projection map showing locations of tectonic landform examples in the following figures.

Background

Tectonic landforms on the Moon are expressed through three principal

morphologic classifications: wrinkle ridges, lobate scarps, and graben. Wrinkle ridges are

curvilinear to sinuous raised relief landforms comprised of a broad arch with a

superimposed narrow crest (Fig. 2) [e.g., Gilbert, 1893; Lucchitta, 1976; Plescia and

Golombek, 1986; Watters and Johnson, 2010]. Wrinkle ridge heights reach up to several

hundred meters and lengths reach up to over a hundred kilometers [Watters, 1988; Golombek *et al*., 1991; Watters and Johnson, 2010]. They occur exclusively in mare deposits and have been interpreted to be surface expressions of complex thrust faulting and folding, although the subsurface structure is debated [Golombek et al., 1991; Watters, 1992; Schultz, 2000; Golombek et al., 2001; Mueller and Golombek, 2004; Watters, 2004]. In large impact basins like Imbrium, wrinkle ridges typically occur radial or concentric to the center of the basin and have been proposed to form as a result of flexure from isostatic compensation soon after emplacement of mare basalts [Melosh 1978; Solomon and Head, 1979, 1980].
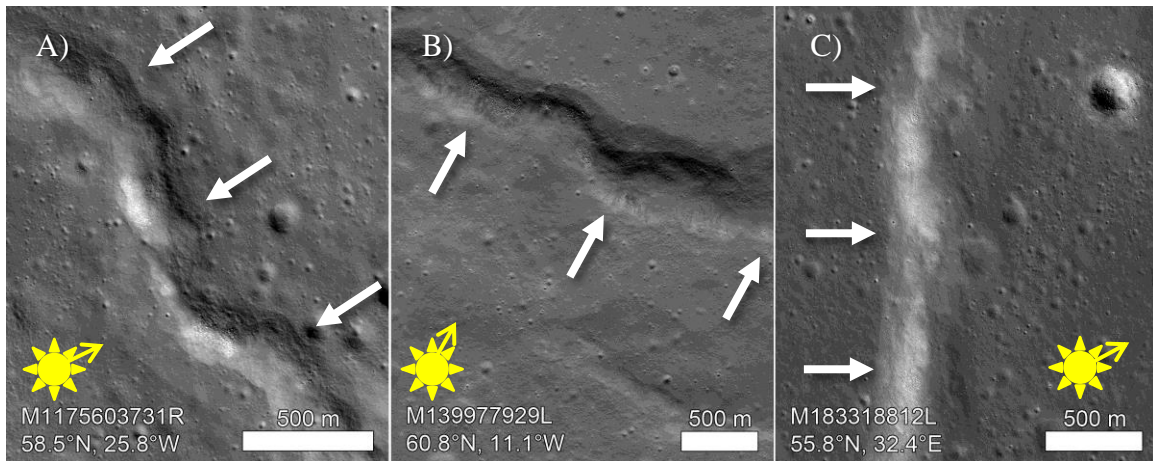
Fig. 2: Examples of degraded lunar wrinkle ridge crests (white arrows) in Mare Frigoris.

Lunar lobate scarps are curvilinear to arcuate raised relief landforms, but in contrast to wrinkle ridges, lobate scarps have simple asymmetric morphologies consisting of one steep face and a gently sloping back limb (Fig. 3) [e.g., Binder and Gunga, 1985; Banks *et al*., 2012]. They are also interpreted to be surface expressions of thrust faults, but simpler and with much less folding than wrinkle ridges [Binder and Gunga, 1985;

Watters *et al*., 2010; Williams *et al*., 2013]. Lobate scarps have typical heights of tens of meters with some over a hundred meters in relief. Typical lengths of individual lobate scarps are only a few to tens of kilometers, although grouped series of scarps collectively can have much greater extents, some spanning several hundreds of kilometers [Binder and Gunga, 1985; Banks *et al*., 2012]. They occur throughout the highlands at all latitudes and are observed in the maria, except at mare-highland boundaries where lobate scarps sometimes transition to more complex wrinkle ridge morphologies (Fig. 4) [Howard and Muehlberger, 1973; Lucchitta, 1976; Watters, 1988; Watters *et al*., 2010]. For example, the Lee-Lincoln scarp in the valley of Taurus-Littrow near the Apollo 17 landing site is a well-documented lobate scarp that transitions into a more complex wrinkle ridge-like morphology on the mare-filled valley floor [Schmitt and Cernan, 1973; Scott, 1973; Lucchitta, 1976; Watters and Johnson, 2010].
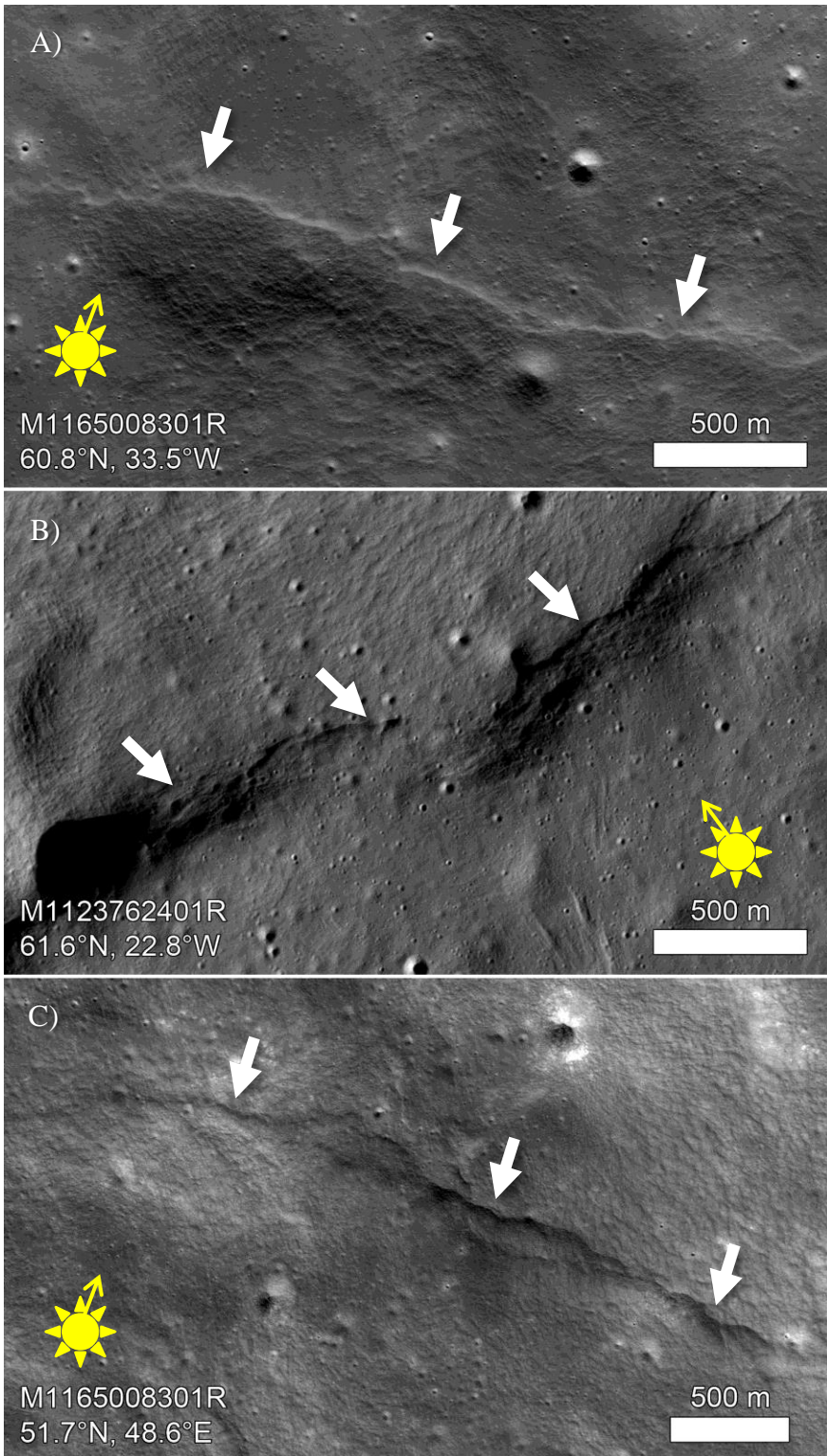
Fig. 3: Examples of lunar lobate scarps (white arrows) in the highlands adjacent to Mare Frigoris.
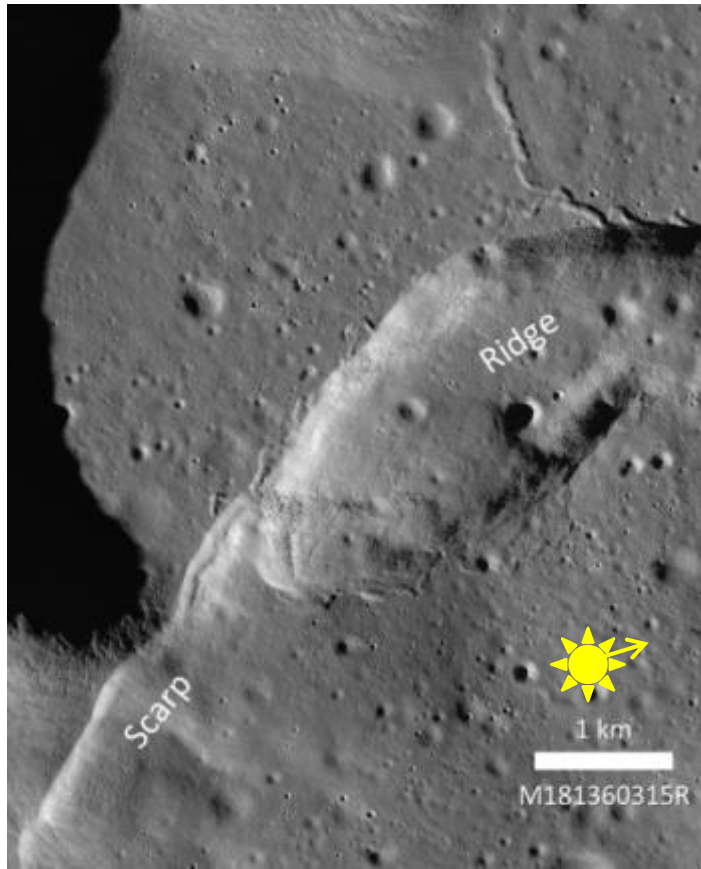
Fig. 4: LROC NAC image showing a wrinkle ridge transitioning to a lobate scarp along the mare-highland boundary in northwestern Mare Frigoris (60.8°N, 27.1°W).

Lunar graben (also called "linear rilles" in some literature) are linear to arcuate negative relief landforms consisting of two steep sides creating a trough, typically with a flat floor (Fig. 5) [McGill, 1971; Golombek, 1979]. Large graben have typical depths of several hundred meters, widths of hundreds of meters to over a kilometer, and lengths of up to several hundred kilometers [Watters and Johnson, 2010]. These large graben occur in both the maria and the neighboring highlands, and typically have basin-concentric or basin-radial orientations [McGill, 1971; Golombek, 1979; Wilhelms, 1987]. Large graben are therefore inferred to form as a result of flexure from isostatic compensation as the extensional counterpart to compressional wrinkle ridges [Melosh, 1978; Solomon and

Head, 1979, 1980]. Recently, a globally distributed population of very small graben has been discovered using LROC NAC images [Watters *et al*., 2012]. Small graben globally have typical depths and widths of only a few to a few tens of meters (average 26 m) and lengths of hundreds of meters (average 179 m) [Watters *et al*., 2012; French *et al*., 2015]. Based on infilling rates of 2-8 cm/million years for shallow depressions in lunar regolith [Arvidson et al., 1975], a ~1 m deep graben should be filled within ~12.5-50 million years. These small-scale graben commonly occur in clusters and are often associated with wrinkle ridges and lobate scarps [Watters *et al*., 2012; French *et al*., 2015].
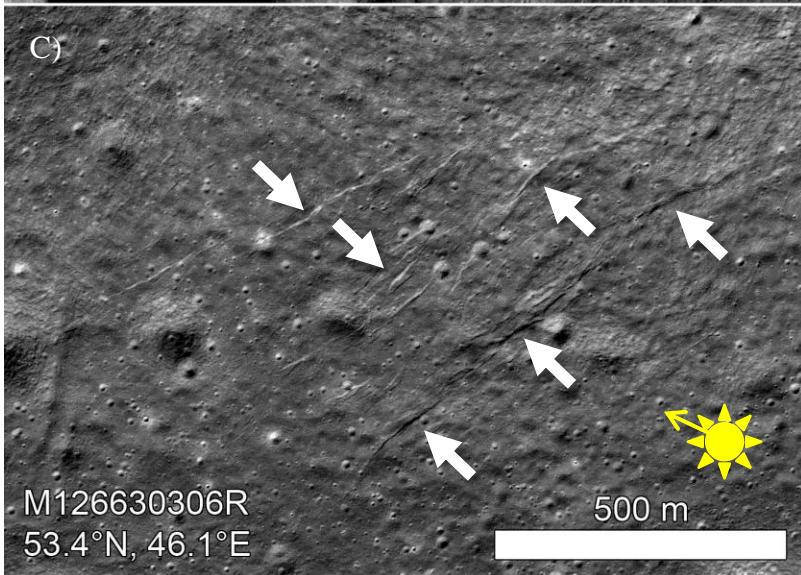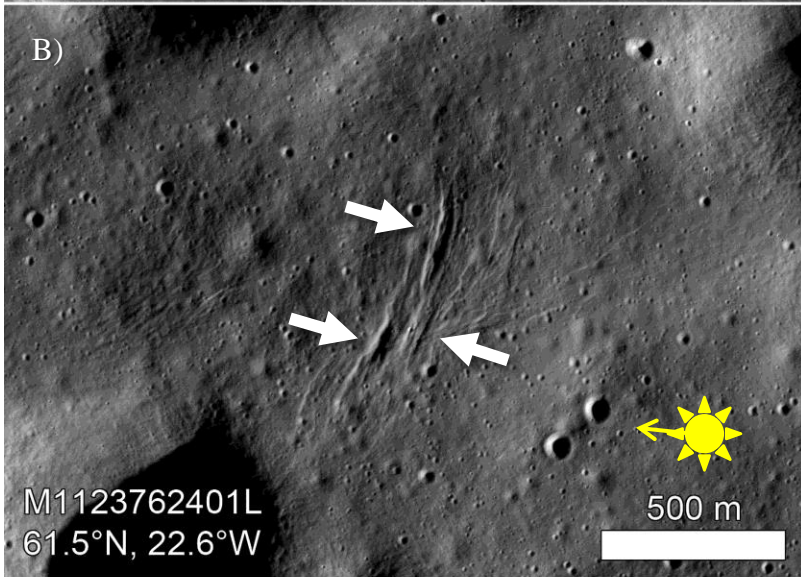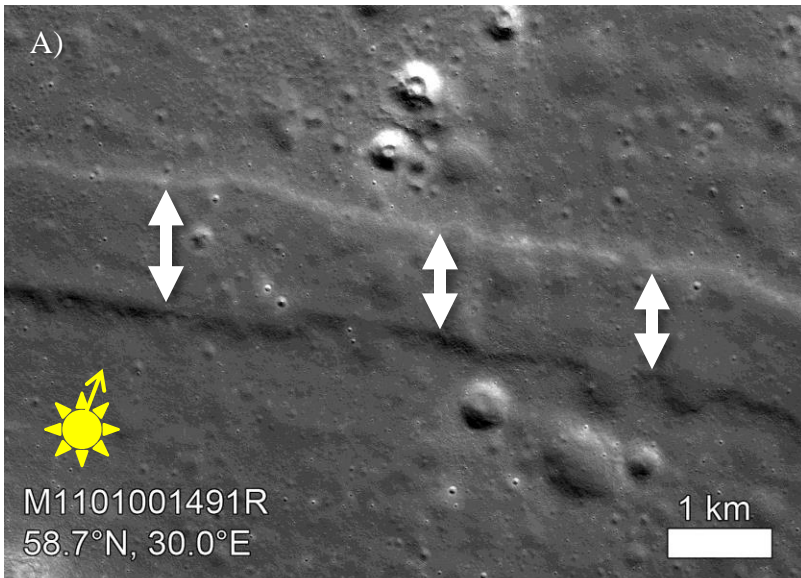
Fig. 5: Examples of a large graben (A, white arrows span width) and two clusters of small graben (B and C, white arrows) in Mare Frigoris.

Mare Frigoris is an excellent site to study the aforementioned landforms, as all occur in or around the basin and in areas with variable influence from mascon flexure. Mare Frigoris is filled with mare basalts ranging in age from ~2.6-3.8 billion years old, with most being ~3.4-3.8 billion years old [Hiesinger *et al.*, 2010]. Basalts in the eastern part of the basin tend to be older (mostly ~3.6-3.8 billion years old) while basalts in the western part of the basin tend to be somewhat younger (mostly ~3.4-3.6 billion years old). Many mare basins are circular or slightly elliptical in shape and formed during large impacts [Wilhelms *et al.*, 1987]. In contrast, the highly elongate and irregular shape of Mare Frigoris does not support an origin as a single impact basin [Whitford-Stark, 1990].

Cadogan [1974, 1975] and Whitaker [1981] proposed that the Mare Frigoris topographic depression is the remnant edge of an ancient (pre-Nectarian) gargantuan impact basin bounded by northern Mare Frigoris, western Oceanus Procellarum, southern Mare Cognitum, and southeastern Mare Vaporum. Such an old, large basin would be consistent with the prevalence of mare volcanism on the lunar nearside, thinner nearside crust, distribution of KREEP materials, and low Al/Si ratio in Imbrium basin ejecta.

The putative Procellarum basin boundary is discontinuous and lacks a diagnostic impact signature such as a central mascon. Using GRAIL gravity gradiometry, Andrews-Hanna *et al.* [2014] identified a polygonal zone of density contrasts along the previously proposed boundaries of the Procellarum basin. A polygonal boundary is not expected for large impacts which should be circular or elliptical. To explain the polygonal structure, Andrews-Hanna *et al.* [2014] proposed that the Procellarum basin, including Mare Frigoris, may instead be part of a rift system flooded with mare basalts. Such a rift system should produce primarily extensional structures sub-parallel to the main spreading center.

In contrast to Procellarum-related hypotheses, Whitford-Stark [1981, 1990] proposed that the topographic depression of western Mare Frigoris might instead have formed by collapse of a large highlands block into the Imbrium impact cavity. A preferential development of wrinkle ridges in thicker mare deposits along the northern boundary of western Mare Frigoris would be consistent with block rotation in support of a collapse model. Whitford-Stark also noted that tectonic structures in the eastern part of Mare Frigoris have a pattern consistent with an impact basin, highly degraded and infilled with mare basalts continuous in extent with the mare fill in the non-impact western part of the basin.

Previous studies of Mare Frigoris, however, were limited by the availability of high resolution images at optimal lighting conditions. Whitford-Stark [1990] previously performed a tectonic survey of the basin with limited Lunar Orbiter and Earth-based photographs. High resolution Apollo images were not available due to those missions' equatorial orbits. The Lunar Orbiter photographs for Mare Frigoris, particularly of the eastern basin, were of poor quality in both resolution and lighting that limited morphologic discrimination. Study of high latitude areas of Mare Frigoris were also limited by the highly oblique angles of Earth-based imaging. As a result, many tectonic landforms, especially small-scale examples, could not be identified and their numbers, stratigraphic relationships, and spatial distribution within Mare Frigoris were poorly understood. Two decades later, new imaging has enabled us to resurvey and better understand the distribution and character of tectonic landforms in Mare Frigoris.

Data and Methods

In 2009, NASA's Lunar Reconnaissance Orbiter was launched into orbit of the Moon. Onboard, the Lunar Reconnaissance Orbiter Camera (LROC) Narrow Angle Cameras (NACs) acquire high resolution (50-200 cm/pixel from 50-200 km altitude, resp.) panchromatic images of the lunar surface [Robinson *et al*., 2010]. Due to the spacecraft's polar orbit, LROC can acquire images at all latitudes and variable lighting conditions. The polar orbit also allows for more frequent flyovers and image acquisitions at higher latitudes. At ~60°N, Mare Frigoris occurs far enough north that it has nearly complete image density, but is not too high latitude to suffer from extreme solar incidence and shadows that limit morphological studies.

I selected over 12,000 LROC NAC images across Mare Frigoris to gain nearly complete (~99%) coverage over the basin and the adjacent highlands. Image selection was restricted by solar incidence angle (55°-85°) and excluded any images acquired during large off-nadir slews by the spacecraft. The selected images were then calibrated, map projected, and resampled to 3 m/pixel using the United States Geological Survey's Integrated System for Imagers and Spectrometers [Anderson *et al*., 2004]. I imported and mosaicked images in a graphical information system and performed a survey of the selected LROC NAC images (for image coverage, see masked area in Fig. 6). Features associated with Mare Imbrium, specifically wrinkle ridges interior to Mare Imbrium and Valles Alpes, were excluded from this survey.

Polyline shapefiles were created for each landform classification: wrinkle ridge, lobate scarp, large graben, and small graben. Polylines for wrinkle ridge segments were drawn along the center of the ridge crest. Polylines for lobate scarps were drawn at the

15

base of the scarp face. Polylines for both large and small graben were drawn along the middle of the trough floor. Polylines for all the different tectonic landforms types were drawn with variable lengths to best capture continuous segments of each landform with a nearly constant azimuth.

In the results maps below, I used a 100 m/pixel LROC Wide Angle Camera (WAC) global mosaic [Robinson *et al*., 2010] and stereo digital elevation model [Scholten *et al*., 2012] (Fig. 6), and a degree and order 900c Gravity Recovery and Interior Laboratory (GRAIL) free air anomaly map [Lemoine *et al*., 2014] (Fig. 8).

Results

Tectonic patterns differ greatly between the eastern and western parts of Mare Frigoris (Figs. 6-8) with a change in tectonic regime around the 15°E meridian. East of ~15°E, wrinkle ridges (red lines in Fig. 6) occur in a polygonal pattern at the center of the basin. Large linear to arcuate graben (yellow lines in Fig. 6) occur to the north and east of the wrinkle ridges, with most oriented concentric to the center of the wrinkle ridge cluster. These eastern basin tectonic landforms tend to be degraded with broadly undulating topography, shallow slopes, numerous superimposed impact craters, and few small craters (<100 m diameter) that appear crosscut. A few wrinkle ridges in eastern Mare Frigoris also appear to have superposed small troughs interpreted as small-scale graben (indicated by short green lines in Fig. 6), and also appear to be degraded as their morphology is not as crisp as that of other small graben identified in western Mare Frigoris or globally.

16
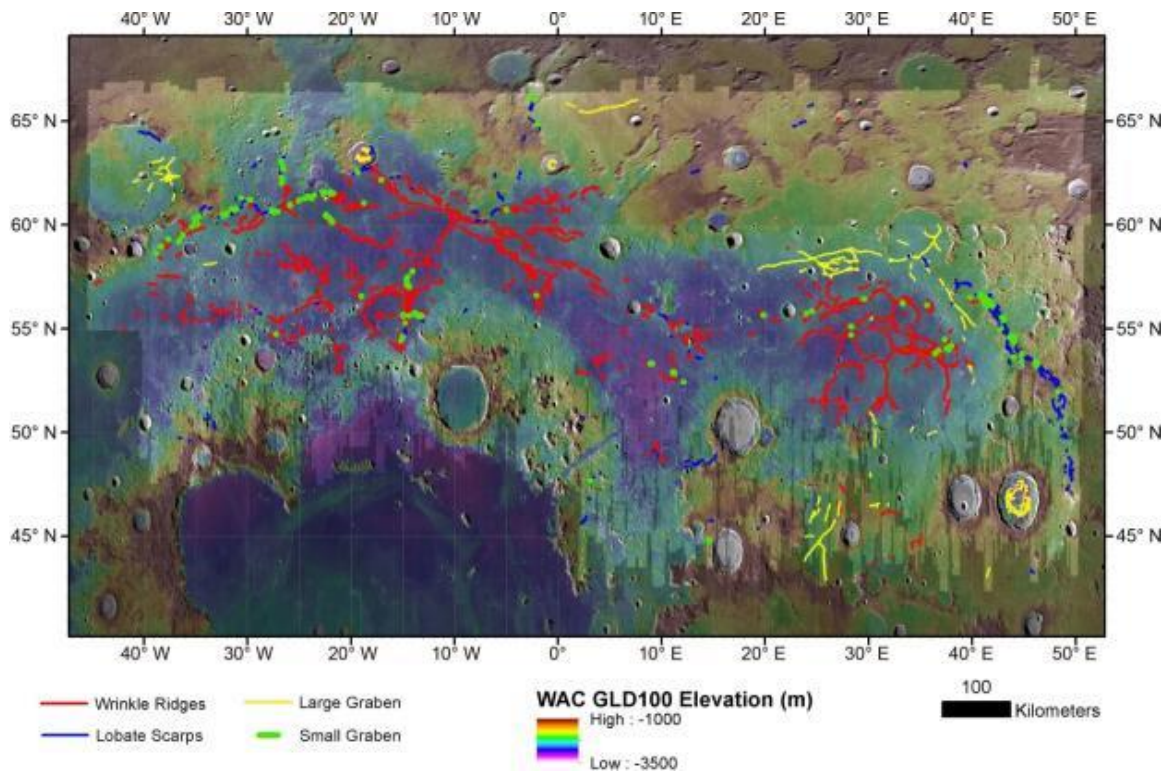
Fig. 6: Tectonic map of Mare Frigoris over LROC WAC GLD100 colorized shaded relief. Shaded mask indicates the boundary of LROC NAC image coverage used in this survey.
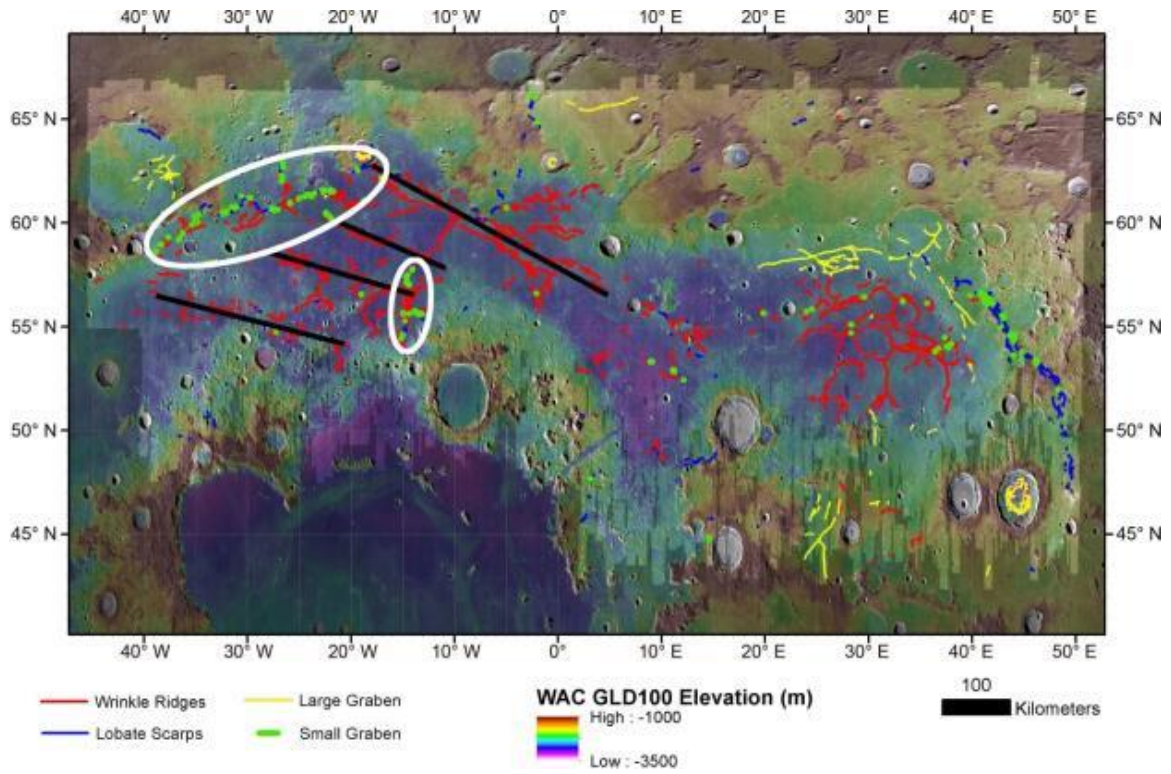
Fig. 7: Tectonic map (same as seen in Fig. 6) with black line overlays indicating parallel sets of degraded wrinkle ridges in western Mare Frigoris, and white circle overlays indicating crisp, young wrinkle ridges.
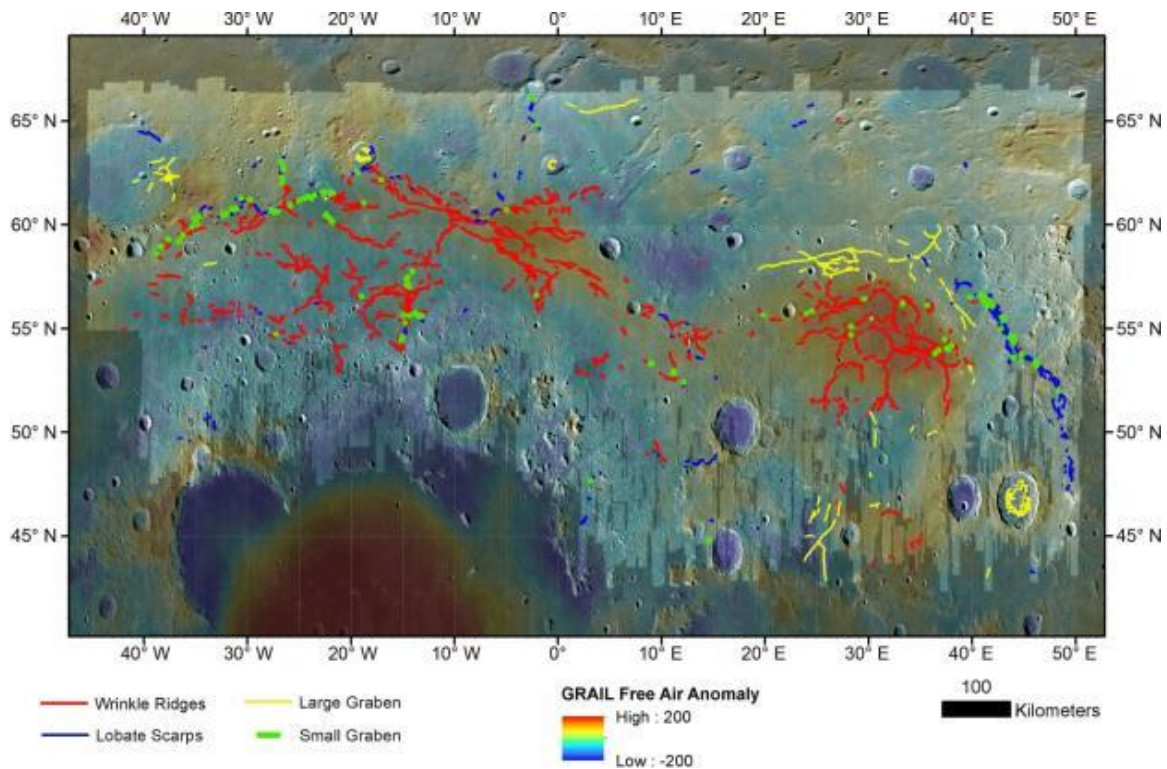
Fig. 8: Tectonic map overlain on GRAIL free-air anomaly map with shaded relief [Zuber *et al*., 2013; Lemoine *et al*., 2014]. Free-air anomalies are due to excess mass, typically from topography and/or variable crustal density.

In contrast to the eastern basin, the area west of ~15°E in Mare Frigoris has two assemblages of tectonic landforms. The first is a set of subparallel wrinkle ridges trending northwest-southeast across the basin (black lines in Fig. 7). Similar to the wrinkle ridges in eastern Mare Frigoris, they appear more degraded with broadly undulating topography, shallow slopes, numerous superimposed impact craters, and no small (<100 m diameter) crosscut craters. The northeasternmost strands of wrinkle ridges in this set have the greatest relief and are the most continuous, whereas the southwesternmost strands are discontinuous and appear to have lower relief.

Western Mare Frigoris also has a distinct population of wrinkle ridges with crisp morphologies (white circles in Fig. 7, examples in Fig. 9) that were not well resolved

and/or well illuminated in previous studies. These wrinkle ridges have relatively steep slopes with abrupt changes in slope (for example, Fig. 10 shows a wrinkle ridge with a 17° slope with a sharp break at the base of its crest), few large (>400 m diameter) superimposed impact craters, and crosscut ~70 small (<100 m diameter) craters. The morphologically crisp wrinkle ridges tend to occur near the mare-highland boundary, but can extend over 60 km into the mare. Their preferred orientation by length-weighted circular mean is 283°/103° measured clockwise from north and is statistically significant with p value of <0.05 calculated using a circular Student's t-test (Fig. 11) [Berens, 2009]. At the mare-highland boundary, these wrinkle ridges sometimes transition to simpler lobate scarp morphologies that continue into the highlands (Fig. 4).
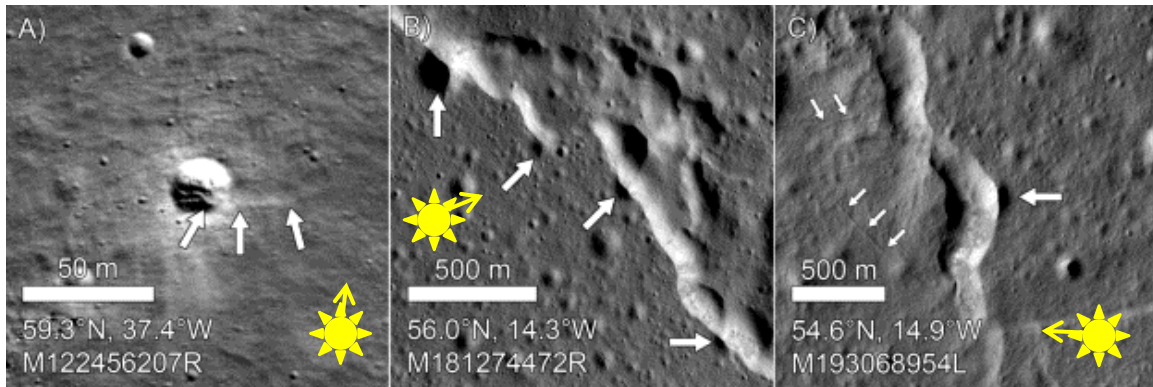
Fig. 9: LROC NAC images showing wrinkle ridges crosscutting small craters. A) A very small wrinkle ridge (arrows) crosscuts a 21 meter diameter crater with bright ejecta. B) A larger wrinkle ridge crosscuts craters (arrows) with diameters of 190 m, 90 m, 100 m, and 80 m from left to right. C) A ~150 m diameter crater (larger white arrow) with an indistinct rim almost completely thrust over by a wrinkle ridge with small shallow graben along the ridge flank (smaller white arrows).
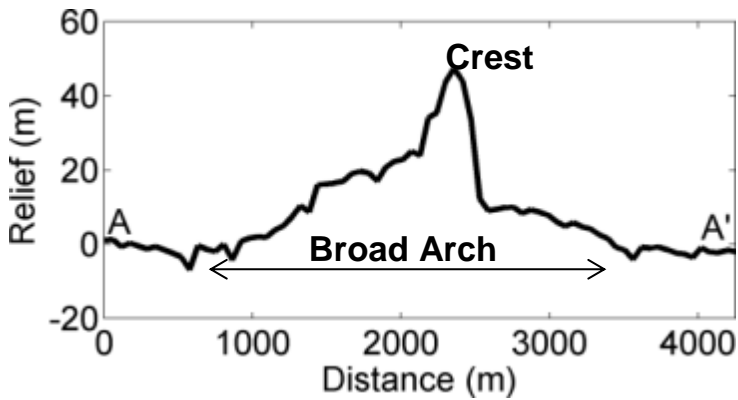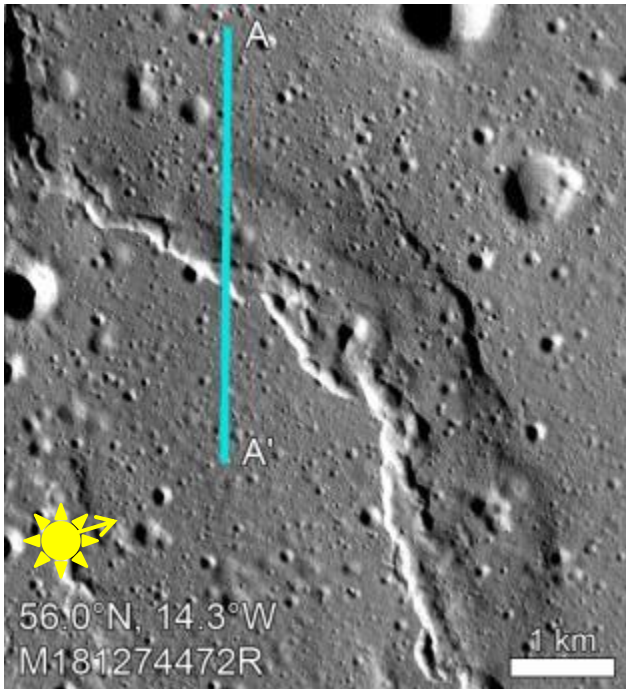
Fig. 10: LROC NAC image showing mare wrinkle ridges with crisp morphologies. A topographic profile from the Lunar Orbiter Laser Altimeter [Smith *et al*., 2010], indicated as A-A' in teal, shows wrinkle ridge relief consisting of a sharp crest superimposed atop a broad arch (after subtraction of the regional slope). Vertical exaggeration of the plot is 25x. True slope on the ridge face is ~17°.
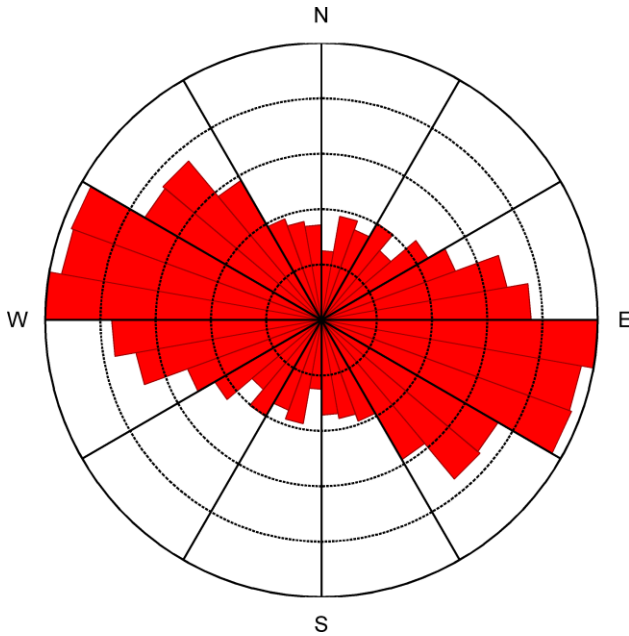
Fig. 11: Rose diagram showing length-weighted distribution of wrinkle ridge orientations in Mare Frigoris west of the 15°E meridian.

Lobate scarps are also observed in the highlands around Mare Frigoris, both transitioning from mare wrinkle ridges and as independent landforms (blue lines in Fig. 6), that were not identified in previous studies. These lobate scarps, like other lobate scarps globally, are very crisp in morphology having steep slopes with sharp changes in slope, few superimposed large (>400 m diameter) craters, and numerous small (<100 m diameter) crosscut craters. The largest series of lobate scarps occurs just east of Mare Frigoris from 57°N, 40°E to 47°N, 50°E. It is over 300 km long and generally split along two paired subparallel strands of scarp segments with opposite asymmetries with scarp faces oriented predominantly outwards from the scarp series' central axis.

Over 500 small graben in Mare Frigoris are exclusively associated with lobate scarps and wrinkle ridges (with distances < 5 km), particularly the crisp wrinkle ridges in western Mare Frigoris (white circles in Fig. 7). Small graben in Mare Frigoris typically

have widths of only a few meters across and lengths of tens to a few hundred meters.

Their depths are not clearly resolved in available stereo topography from LROC

[Robinson *et al*., 2010] or altimetry from LOLA [Smith *et al*., 2010]. Assuming ~60°

dips for the bounding normal faults, I estimate that these small graben have maximum

depths of at most a few meters. The graben have preferred orientations either

perpendicular or parallel to the nearest ridge or scarp, with relatively fewer having

oblique geometries (Figs. 12 and 13).
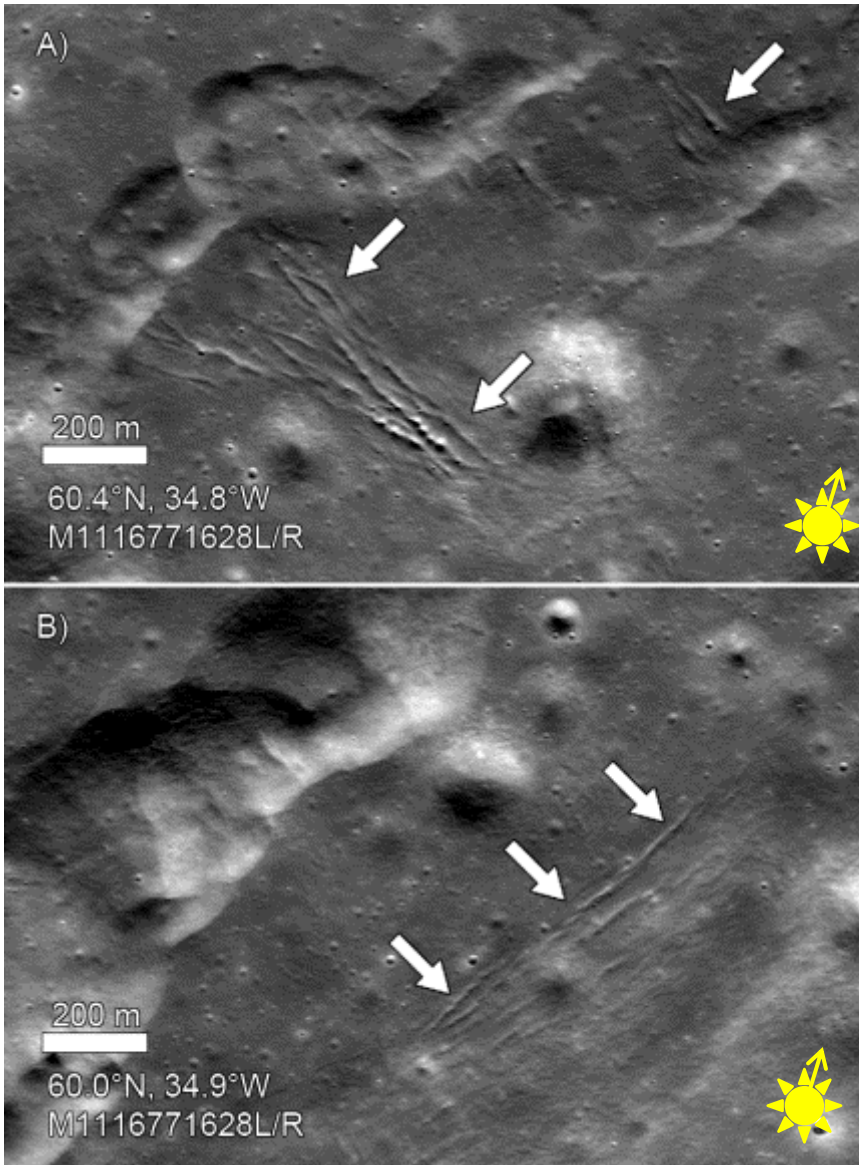
Fig. 12: LROC NAC images showing small graben (arrows) associated with wrinkle ridges. The graben in A) are nearly perpendicular to the associated wrinkle ridge [French *et al.*, 2015], and the graben in B) are nearly parallel to the associated wrinkle ridge.
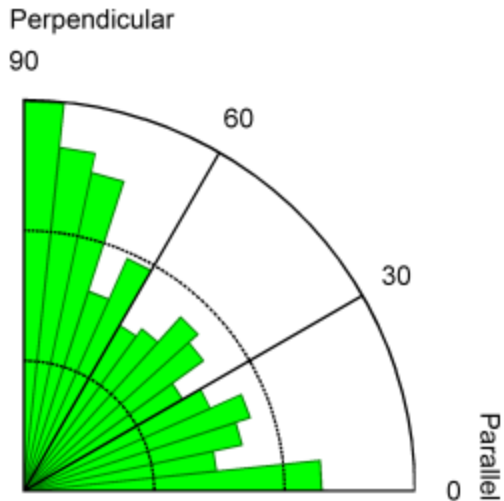
Fig. 13: Azimuthal angle differences between graben and nearest ridge/scarp. Preferred orientations are perpendicular and to a lesser extent parallel.

Discussion

Eastern Mare Frigoris, with its central polygonal pattern of ridges and more distal large concentric graben, is consistent with classic mascon tectonics [see Melosh, 1978; Solomon and Head, 1979, 1980; Whitford-Stark, 1990; Freed *et al*., 2001]. There is no clear circular topographic ring indicative of an impact, but a moderate positive gravity anomaly does occur (Fig. 8) [Zuber *et al*., 2013]. This may have been enabled by mantle uplift under a now heavily degraded ancient impact basin, by thick infilling of mare basalt, or by significant intrusion of high-density magmas. The heavily degraded appearance of both the wrinkle ridges and large graben in this area is consistent with flexure having occurred long ago. In particular, the occurrence of degraded large graben in Mare Frigoris is notable. Based on global crosscutting relations, large-scale graben formation stopped globally ~3.6 billion years ago due to a change from net global expansion to contraction [Solomon and Head, 1979, 1980; Kirk and Stevenson, 1989; Pritchard and Stevenson, 2000]. I therefore infer that a significant proportion of isostatic

flexure in eastern Mare Frigoris occurred prior to 3.6 billion years ago. The lack of large

graben and relatively sparser wrinkle ridges along the southeastern edge of Mare Frigoris

suggests that either flexure may have been limited there, perhaps due to greater structural

rigidity or lithospheric thickness closer to Mare Imbrium and/or Mare Serenitatis

[Wieczorek *et al*., 2013]. Alternatively, the younger (<3.6 billion year old [Hiesinger,

2010]) lavas in southeastern Mare Frigoris may have buried any pre-existing structures,

particularly infilling topographically lower large graben that are thought to have formed

before 3.6 billion years ago.

In contrast, I find that wrinkle ridges in western Mare Frigoris do not support an

origin by mascon induced flexure. Horizontal principal stress components for mascon

induced flexure should be oriented concentric and/or radial to the basin interior [Melosh,

1978; Solomon and Head, 1979, 1980; Freed *et al*., 2001]. Instead, the parallel wrinkle

ridges across western Mare Frigoris (black lines in Fig. 7) have a significant preferred

orientation of 283°/103° (Fig. 11) which indicates that the greatest compressional

horizontal principal stress component across the basin was oriented perpendicular to the

ridges (NE-SW) at the time of fault formation. The typical degraded appearance of these

parallel wrinkle ridges is similar to that of the degraded wrinkle ridges in eastern Mare

Frigoris, as well as many other wrinkle ridges elsewhere on the Moon, suggesting that

they are a similar ancient age and most likely formed soon after emplacement of the mare

basalts.

The northeasternmost of the parallel wrinkle ridges is approximately tangential to

Mare Imbrium. This was previously cited to argue that the Frigoris topographic basin

may represent a depression resulting from collapsing a highlands block into Imbrium's

impact cavity to the south [Whitford-Stark, 1990]. This crustal block collapse predicts wrinkle ridges preferentially on the northern boundary of the Mare Frigoris, but many of the old parallel wrinkle ridges occur all the way across Mare Frigoris and argue against crustal collapse into Imbrium. The parallel wrinkle ridges farther west across Mare Frigoris also have highly oblique orientations with respect to the rim of Mare Imbrium. These non-tangential and non-radial orientations are also inconsistent with flexure induced by Mare Imbrium's mascon.

Wrinkle ridges in the parallel set have decreasing relief and continuity away from the northeasternmost ridge, which suggests that they formed in the same regional, non-isotropic stress regime but with decreasing contractional strain with distance towards the south and west. Such a large-scale stress field could be accomplished, for example, by a gargantuan impact structure [Whitaker, 1981] or by rifting [Andrews-Hanna *et al*., 2014]. I do not find evidence directly suggesting a giant impact control, such as the "Procellarum basin" [Whitaker, 1981]. Some positive gravity anomalies in Oceanus Procellarum are proposed to be basalt-filled rift valleys with very large wrinkle ridges formed over them, possibly in response to flexure from a super-isostatic load of locally thicker basalts [Andrews-Hanna *et al*., 2014]. A similar but smaller linear positive gravity anomaly is located slightly east of and parallel to the northeasternmost and largest wrinkle ridge in western Mare Frigoris. However, the other wrinkle ridges in the parallel set that are farther west across Mare Frigoris do not show significant associated positive gravity anomalies. This may be due to a resolution issue with the available GRAIL gravity data, or the wrinkle ridges are not underlain by thicker basalts. Without a thick

27

basaltic fill to drive flexure in western Mare Frigoris, faulting could be relatively more sensitive to distal and global stresses.

In addition to the parallel series of degraded wrinkle ridges in western Mare Frigoris are two groups of wrinkle ridges with crisp morphologies (white circles in Fig. 7, also Figs. 9 and 10). The difference in morphological crispness (compare Figs. 2 and 9) suggests a relative age difference, with the crisper ridges being younger than the degraded parallel set. Absolute age estimation by areal crater size frequency distributions is not applicable for small curvilinear features or variable slopes, but crosscutting relationships with small craters can be used to constrain absolute ages of curvilinear landforms. Specifically, craters ~80-100 m in diameter or smaller degrade and infill within ~1 billion years [Trask, 1971; Moore et al., 1980], and can provide maximum age constraints on crosscutting landforms such as wrinkle ridges. Most notably among the ~70 small crosscut craters I identified is a 21 m diameter crater, with bright ejecta, bisected by a small splay off a wrinkle ridge (Fig. 9A). Based on previous crater degradation calibrations, this crater has a modeled age of ~40 million years [Moore et al., 1980]. Seismic shaking by the crosscutting fault presumably enhances degradation, so model degradation ages are likely overestimates for small craters crosscut by faults. Since these two groups of crisp wrinkle ridges crosscut small craters <100 m in diameter, these crisp mare wrinkle ridges have been active within the past 1 billion years, and some of these wrinkle ridges have likely been active as recently as within the past ~40 million years.

The distribution and orientations of small graben in Mare Frigoris suggest that they formed as a secondary effect of thrust faulting in wrinkle ridge and lobate scarp

formation [Plescia and Golombek, 1986; Watters, 1988; Watters et al., 2012; French *et al*., 2015]. During wrinkle ridge development, antiformal flexural bending and uplift enhances extension of upper-surface material in the same direction as compression on an underlying thrust fault, such that graben can preferentially form with their long axes parallel to their host wrinkle ridges. Alternatively, dilation of regolith is a more likely mechanism for forming perpendicular graben. Specifically, a perpendicular preference in orientation can come from an extensional principal stress component orthogonal to the direction of compression on the wrinkle ridge. Non-preferred, intermediate orientations are also possible due to regolith complexity, pre-existing structures or weaknesses in the substrate, and fault tip effects [Stein, 1999].

The preservation and incomplete filling of such small features in the lunar regolith implies that not only are the graben very young, but also that wrinkle ridge faults causing the associated flexure must have been active within the past few tens of millions of years, and indeed could still be active today. Small graben have also been identified in association with some lobate scarps in the highlands, and some wrinkle ridges in other mare basins [Watters *et al*., 2012; French *et al*., 2015] implying that recent wrinkle ridge activity is not restricted to Mare Frigoris. Although a comparable high resolution (few meters/pixel) tectonic mapping campaign has not yet been performed covering all maria and wrinkle ridges globally, I predict that young wrinkle ridge activity is widespread.

A young age for the crisp wrinkle ridges is further supported by the transitions between some wrinkle ridges and young (<1 billion years old) lobate scarps at mare-highland boundaries. These transitions occur both in Mare Frigoris (*e.g*., Fig. 4) and at other locations globally including the Lee-Lincoln scarp [Schmitt and Cernan, 1973;

Scott, 1973; Lucchitta, 1976; Watters and Johnson, 2010]. Thrust faults that underlie both wrinkle ridges and lobate scarps are probably continuous where they cross the mare-highland boundary. Slip on segments of a continuous fault surface likely deform overlaying material on both sides of the mare-highland boundary. Young mare wrinkle ridges at transitions are therefore inferred to deform contemporaneously with highland lobate scarps, consistent with the young ages implied by small crosscut craters and within the established scarp age range of <1.0 billion years [Binder and Gunga, 1985; Watters *et al.*, 2010]. The difference in surface expressions between wrinkle ridges and lobate scarps most likely represents a change in material properties due to layering [Lucchitta, 1976; Watters, 1988, 1991]. Based on lobate scarps' and wrinkle ridges' similar ages and examples of continuous transitions between the two morphologic endmembers across geologic terrains, I propose that both lobate scarps and the young subset of wrinkle ridges (white circles in Fig 7) form from the same compressional stress resulting from the same process.

The young apparent age (<1 Ga) of crisp wrinkle ridges in western Mare Frigoris does not fit the classical mascon flexure model. In addition, the strong preferred orientations are inconsistent with mascon flexure. The greatest isostatic compensation occurs soon after basalt emplacement, which in Mare Frigoris mostly occurred between ~3.4-3.8 billion years ago, with the youngest remnant volcanism ceasing by ~2.6 billion years ago [Hiesinger *et al.*, 2010]. Although early flexure induced subsidence is a possible explanation for the initiation of some faults, such ancient flexure is expected to be insufficient to result in significant recent additional displacement. However, a small

30

component of the total stress contributed by subsidence cannot be excluded and could locally influence orientations of some young wrinkle ridges.

Although the primary focus of this study was structures internal to Mare Frigoris, I identified numerous lobate scarps in the highlands adjacent to the mare (blue lines between 40°E-50°E in Fig. 6). These lobate scarps have crisp morphologies and crosscut small (<100 m diameter) craters consistent with a young age (<1 billion years), similar to observations of other lobate scarps observed in Mare Frigoris and globally as reported in previous studies [Binder and Gunga, 1985; Watters *et al*., 2010; Banks *et al*., 2012]. No overall spatial pattern is observed for the lobate scarps in the limited highlands area surveyed, with the exception of the large series of lobate scarps just to the east of the basin (Figs. 6, 8). Series of similarly trending lobate scarps are common on the Moon, but the particularly large cumulative length (>300 km) and sub-parallel paired structure comprising this series east of the basin are noteworthy. The preferential outward-facing scarp faces suggest that the thrust faults dip inwards towards the center of the series. Numerous small graben occur in the back limbs and in between the scarps indicating localized secondary extension; the spatial correlation further supports a young age for lobate scarps. Such long, paired thrust faults are suggestive of deeper structural control; however, no evidence of such an underlying structure in visible images, topography, or gravity anomaly data was found.

The Apollo lunar seismic network recorded 28 shallow "moonquakes" between 1971 and 1976, distinguished from numerous deep-sourced events and impacts by the shallow quakes' high frequencies. The moment magnitude 2.7 [Oberst, 1987] shallow moonquake recorded on Dec. 6th, 1972, presents an interesting case. Nakamura [1979]

located this moonquake epicenter at 51°N, 45°E, after assuming a 100 km depth,

although the event could have been closer to the surface. This places it to within 65 km

(~2°) of the 300 km long series of lobate scarps east of Mare Frigoris. The locations of

the reported epicenter are not precise to 1°, but should be accurate within a few degrees.

The spatial and temporal correlation of this shallow moonquake with these very crisp

lobate scarps is consistent with ongoing surface tectonism on the Moon.

Energy released from recorded shallow seismic events and observed strain from

lobate scarps can be compared to test if the observed young tectonic landforms could

have produced the recorded level of shallow seismicity on the Moon. Strain and seismic

energy release are empirically related by $M_0 = 2\mu dA\varepsilon$, where M_0 is the geodetic moment,

μ is the shear modulus, d is fault depth, A is surface area, and ε is strain [Savage and

Simpson, 1997]. Modeling indicates that lobate scarps are shallow with depths d of ~1

km [Williams et al., 2013]. A is calculated as the surface area of a sphere with a radius r

of 1,737.4 km by $A = 4\pi r^2$. The strain ε observed from globally mapped lobate scarps is

estimated to be between 0.003% (lower limit) [see Watters *et al*., 2015] and 0.01% (upper

limit) [Watters *et al*., 2010]. The shear modulus can be derived from the shear wave

velocity and density by $\mu = V_s^2\rho$, where at 1 km depth, seismic shear wave velocity V_s is

2.8 km/s [Nakamura *et al*., 1982] and density ρ is 2550 kg/m^3 [Zuber *et al*., 2013].

Dividing the total geodetic moment by estimates for the lifetime of the lobate scarp

population of 1 billion years [Binder and Gunga, 1985; Watters *et al*., 2010] and 50

million years [Watters *et al*., 2015] yields estimated annual seismic energy releases of

1.5×10^{14} N-m to 3×10^{15} N-m for 0.01% strain, and 4.5×10^{13} N-m to 9×10^{14} N-m for

0.003% strain. These two estimated ages of strain release bound the observed average

seismic energy release of 6.6×10^{14} N m recorded by Apollo [Nakamura, 1979; Oberst *et al*., 1987]. Strain from the mapped global population of young lobate scarps predicts a level of seismicity consistent with the shallow moonquakes recorded during Apollo. Future studies such as a modern seismic network should be directed to detect activity at these young lunar tectonic landforms.

The global population of lobate scarps, predominantly in the highlands, suggests that the Moon's surface is under several MPa of net compressive stress resulting from a small amount of global thermal contraction [Binder and Gunga, 1985; Pritchard and Stevenson; Watters *et al*., 2010; Williams *et al*., 2013] with a lesser contribution of a few kPa by tidal stresses [Watters *et al*., in review] and possibly local stresses from isostatically uncompensated terrain indicated by free-air gravity anomalies [Zuber *et al*., 2012]. The concurrent timing of wrinkle ridges and lobate scarps and the occurrence of ridge–scarp transitions at mare–highland boundaries strongly suggests a shared stress source between associated landforms. We propose that these new young mare wrinkle ridges – akin to highland lobate scarps – also accommodate stress and strain from primarily global thermal contraction with secondary contributions from tidal stresses.

2. FAULT DISLOCATION MODELED STRUCTURE OF LOBATE SCARPS FROM LUNAR RECONNAISSANCE ORBITER CAMERA DIGITAL TERRAIN MODELS

Background

Lobate scarps are linear or curvilinear topographic rises that have been observed on all of the terrestrial planets except Venus. To date, lobate scarps have been identified in nearly 100 different locations on the Moon in both the mare and highlands, including over 20 scarps and scarp complexes at latitudes greater than 60° [Binder and Gunga, 1985; Banks *et al*., 2012], and appear to be globally distributed [Watters *et al*., 2010]. Lobate scarps are interpreted as shallow, low-angle thrust fault scarps with hanging walls moved up relative to footwalls [Lucchitta, 1976; Binder, 1982; Binder and Gunga, 1985]. Lunar scarps are typically ~10-20 kilometers in length or less, tens to hundreds of meters in width, and up to ~150 meters in relief [Binder and Gunga, 1985; Banks *et al*., 2012]. In cross-section, they appear asymmetric with steep scarp faces (~5°-29°), crests typically a few tens of meters high, and gently-sloping back-limbs [Binder and Gunga, 1985; Watters and Johnson, 2010; Banks *et al*., 2012]. The vergence direction of many scarps is oriented up-slope, but vergence direction sometimes reverses along strike [Schultz, 1976]. Scarp complexes or groups often include en-echelon stepping segments in parallel or sub-parallel orientations [Binder and Gunga, 1985].

Prior to Lunar Reconnaissance Orbiter (LRO) observations, lobate scarps were only identified in equatorial regions due to limited high-resolution Apollo Panoramic Camera and Lunar Orbiter image coverage with optimal lighting (less than 10% of the lunar surface) [Binder, 1982; Binder and Gunga, 1985; Watters and Johnson, 2010].

Maximum relief of a limited number of lobate scarps was determined with photoclinometry or shadow measurements [Binder and Gunga, 1985; Watters and Johnson, 2010].

Lobate scarp morphologies are usually crisp and relatively undegraded by impact craters. They are interpreted as some of the youngest endogenic landforms on the Moon, with maximum age estimates of less than 1 billion years based on transected small (<50 m) diameter fresh craters [Binder and Gunga, 1985; Watters *et al*., 2010]. The scarps are thought to have formed as a result of late-stage global radial contraction of the Moon [Binder, 1982; Binder and Gunga, 1985; Watters *et al*., 2010; Watters and Johnson, 2010]. Radial contraction of the Moon is inferred from the shortening across lobate scarps globally and estimated at ~100 m [Watters *et al*., 2010].

The Hinks Dorsum lobate scarp on asteroid 433 Eros [Watters *et al*., 2011] is comparably-sized to lunar scarps, with a maximum relief of 60 meters. Lobate scarps on Mercury [Strom *et al*., 1975; Watters *et al*., 2009; Solomon *et al*., 2008] and Mars [Watters, 2003], however, can be up to an order of magnitude larger and may have over a kilometer of relief. Fault dislocation models constrained by topographic observations of lobate scarps on Mars, Mercury, and asteroid 433 Eros indicate that the underlying faults are likely planar [Schultz and Watters, 2001; Watters and Schultz, 2002; Watters *et al*., 2002; 2011]. However, subsurface fault geometries and mechanical properties of the lunar crust and lithosphere remain poorly understood [Binder and Gunga, 1985; Watters and Johnson, 2010].

Topography derived from Lunar Reconnaissance Orbiter Camera (LROC) stereo images provides new constraints on mechanical and kinematic models for the formation

of tectonic landforms on the Moon. Here, morphology and regional context are described for six lunar lobate scarps for which high resolution LROC stereo images and derived digital terrain models (DTMs) are currently available: Slipher, Racah X-1, Mandel'shtam A, Feoktistov, Simpelius-1, and Oppenheimer F (informally named for nearby impact craters) (Fig. 14). Fault dislocation models are created and compared to DTM topography to constrain the dips, depths, and displacements of the faults underlying these lobate scarps. The modeled geometries are then used to constrain the current state of stress in the lunar crust using frictional sliding and cohesive rock failure criteria.
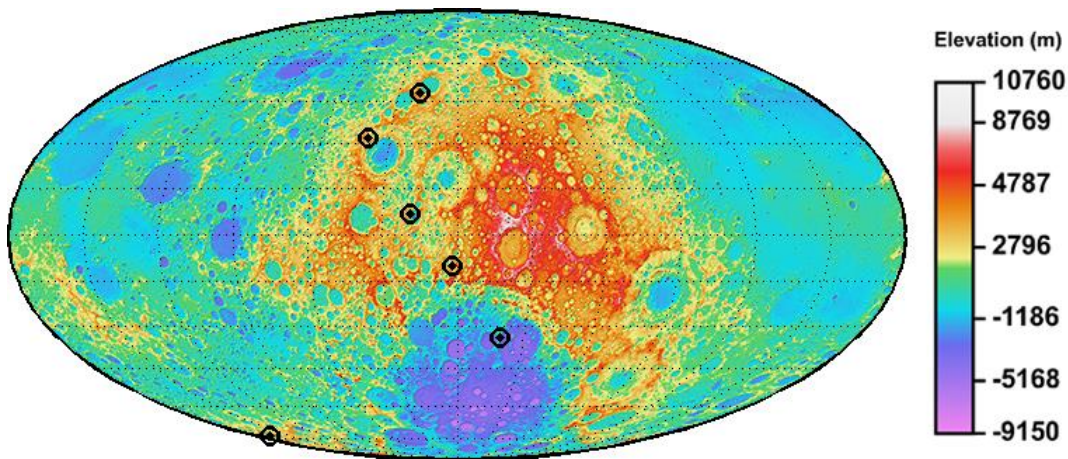
Fig. 14: Locations of scarps examined in this study (black circles) overlain on a Mollweide equal area projection map of LROC WAC global 64-pixel-per-degree topography centered on the anti-Earth point [Scholten *et al*., 2011].

Data and Methods

LROC consists of two Narrow Angle Cameras (NACs) and one Wide Angle Camera (WAC) [Robinson *et al*., 2010]. From its nominal 50 km altitude orbit, the NACs acquire images with resolutions as high as 50 cm/pix across an approximately 5 km swath, whereas the WAC acquires images with a coarser resolution of ~100 m/pix but a

~104 km wide field of view, providing regional and global context. LROC obtains stereo

NAC observations by acquiring at least two NAC images of the same area but from

different angles by rolling the spacecraft off-nadir on a subsequent orbit. High-resolution

(~2 m/pix, typically 1-3 m vertical precision) DTMs are derived using SOCET-SET

software by performing image correlation and edge matching for every pixel in stereo

NAC image pairs [Tran *et al.*, 2010].

Derived terrain is tied to absolute elevations from Lunar Orbiter Laser Altimeter

(LOLA) ranging profiles that cross the scene [DeVenecia *et al.*, 2007; Tran *et al.*, 2010].

LOLA ranging orbital tracks run approximately north-south with slightly lower

horizontal resolutions along-track than LROC NAC stereo derived DTMs. LOLA ranging

has small vertical uncertainties, but can have horizontal uncertainties of 50 and 300 m

(with and without crossover analysis, resp.), and tracks typically do not provide

continuous coverage along the entire length of the scarp [Tran *et al.*, 2010]. LOLA

profiles are thus best suited for coarse morphological analyses of east-west trending

scarps [Banks *et al.*, 2012] while profiles from LROC NAC DTMs can be extracted with

any orientation, and where pre-existing topographic variations are minimized such that

the expression of the scarp is the primary feature in the local topography. For these

reasons, I exclusively use NAC stereo derive DTMs for the analyses in this study. The

linear regional slope along each profile is subtracted to detrend and isolate scarp

morphology from the surrounding terrain.

Fault dislocation models are created using the Coulomb software package [Lin

and Stein, 2004; Toda et al., 2005] based on stress and material displacement functions

for an elastic half-space [Okada, 1992]. An elastic modulus (*E*) of 40 to 80 GPa and

Poisson's ratio (*v*) of 0.25 are assumed for the lunar crust, comparable to values for

Earth's crust [Turcotte and Schubert, 1982; Bürgmann *et al*., 1994] and assumed similar

for Mercury, Mars, and asteroid 433 Eros [Schultz and Watters, 2001; Watters *et al*.,

2002; Watters and Schultz, 2002; Watters, 2011]. Pritchard and Stevenson (2000) suggest

the elastic modulus and Poisson's ratio might be 10-100 times less than normal values

because of the heavy impact damage; however, decreasing these parameters in Coulomb

by a factor of 100 has a negligible influence on modeled displacements. Fault geometry

and fault slip are the dominant controls of scarp topography. The fault surface is defined

as a dipping rectangular plane, suggested for lobate scarp models by Watters and Schultz

(2002) (Fig. 15). The maximum slip *S* on the fault is first estimated from the maximum

relief of the scarp *h* to provide the vertical scale for a model profile (Fig. 16A). Maximum

depth of faulting *T* is determined to a first order using the width of the scarp and an

approximate fault dip angle (Fig. 16B). Fault dip angle *θ* primarily influences the shape

of the scarp's back limb, with higher dip angles leading to greater relief in the back-limb

and eventually creating a hunched-back (Fig. 16C). Near the edges of the fault plane, slip

is allowed to taper from its maximum value to zero in 5 steps over a distance *u* from the

edge to avoid unrealistically large stress concentrations at the fault tips. Increasing the

taper (*u*) primarily decreases the slope of the scarp face, rounds off the scarp crest and

shifts it towards the back limb (Fig. 16D). Fault dip, depth, slip, and taper are varied

iteratively to create forward-modeled profiles with similar reliefs and slopes to the scarps

in the detrended topographic profiles. As discussed below, solutions are non-unique, but

suggest narrow ranges for geometric parameters. Fault dislocation models were fit to

profiles across the Slipher, Racah X-1, Mandel'shtam A, Feoktistov, Simpelius-1, and

Oppenheimer F lobate scarps. Parameter ranges are determined such that the resulting

model does not significantly and consistently deviate (by a value ~20% of the maximum

relief over a 100 m baseline) from the detrended profile atop the scarp's face, crest, or

back-limb, unless the variation in topography is attributed to a landform not associated

with deformation on the main scarp, such as an impact crater or a secondary scarp.
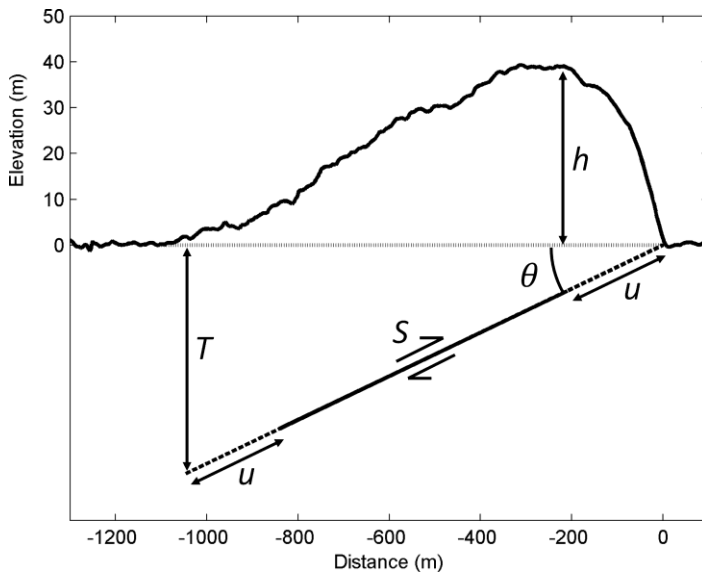
Fig. 15: Model parameters for an example lobate scarp profile (Mandel'shtam A). T is the maximum depth of faulting, h is the maximum relief of the scarp, θ is the fault dip angle, S is the slip, and u is the taper distance where slip decreases from a maximum value of S in the middle of the fault to 0 at the tips. The depth of faulting is not to scale.
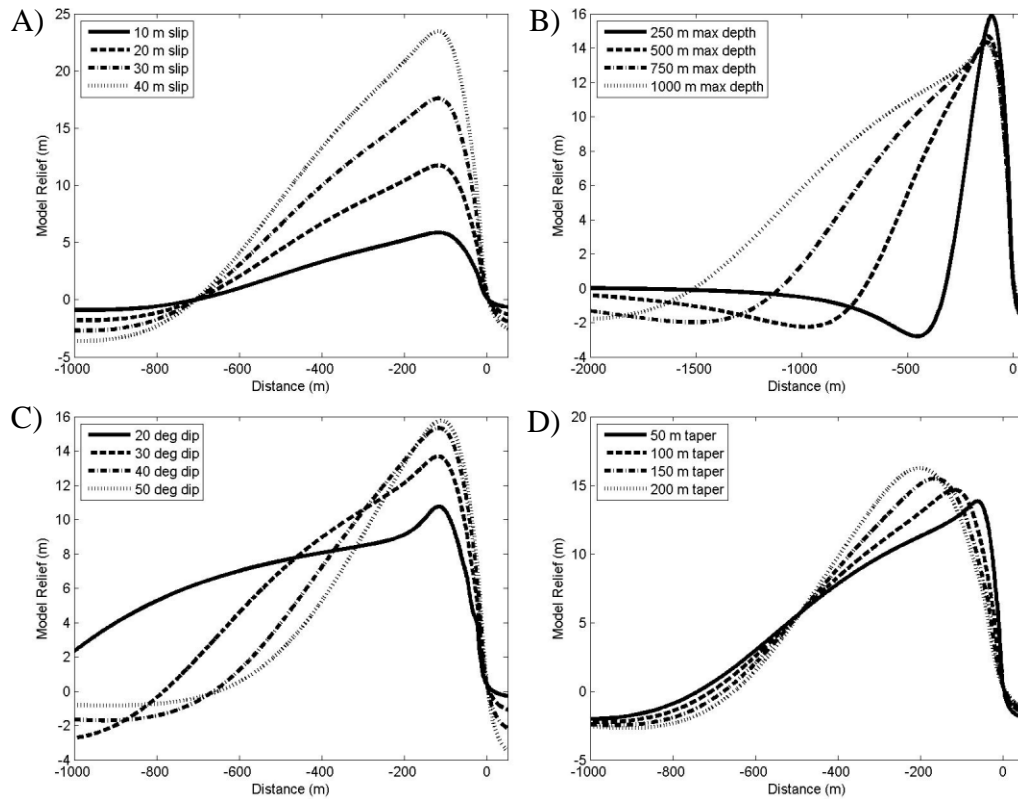
Fig. 16A-D: Sensitivity curves for variables in fault dislocation modeling. Unless stated otherwise, fault slip is 25 m, maximum depth is 500 m, dip angle is 35°, and the fault slip is tapered within 100 m of its edges.

The Slipher scarp (48.2°N, 160.8°E) occurs along a bench in the southern wall of the impact crater Slipher (Figs. 17A,18A). The main scarp is oriented E-W with its steepest slope (vergent side) facing south. It also has numerous smaller sub-parallel scarps that splay or branch off the primary one, and sometimes face in the opposite direction (antithetic). A portion of the Slipher scarp also contains small linear graben or troughs superposed on and parallel to the crest of the scarp, possibly indicating localized layer-parallel extension due to flexure of material atop the scarp [Watters *et al*., 2010; Watters *et al*., 2012]. The main scarp in Slipher is ~20 kilometers long and continues over 100 kilometers east as part of a larger cluster of en echelon stepping scarps along the

southern rim of D'Alembert crater. However, high resolution LROC NAC images are not continuous to the east of D'Alembert crater, so the scarp's full extent has not yet been determined. Its maximum detrended relief within Slipher crater has been measured as ~21 meters [Banks *et al.*, 2012], but may be greater in the D'Alembert section.
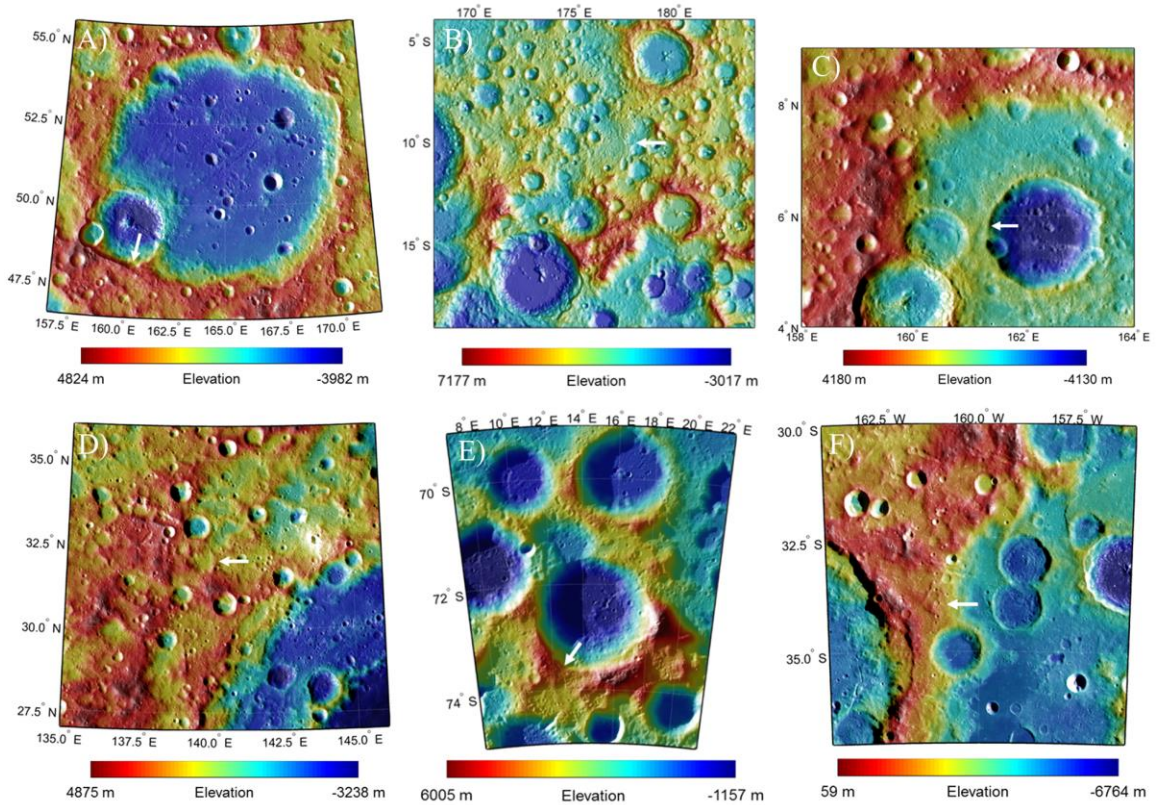
Fig. 17: LROC WAC colorized shaded relief mosaics [Scholten *et al.*, 2011] of: A) Slipher, B) Racah X-1, C) Mandel'shtam A, D) Feoktistov, E) Simpelius-1, and F) Oppenheimer F. White arrows point to the locations of scarps examined in this study.
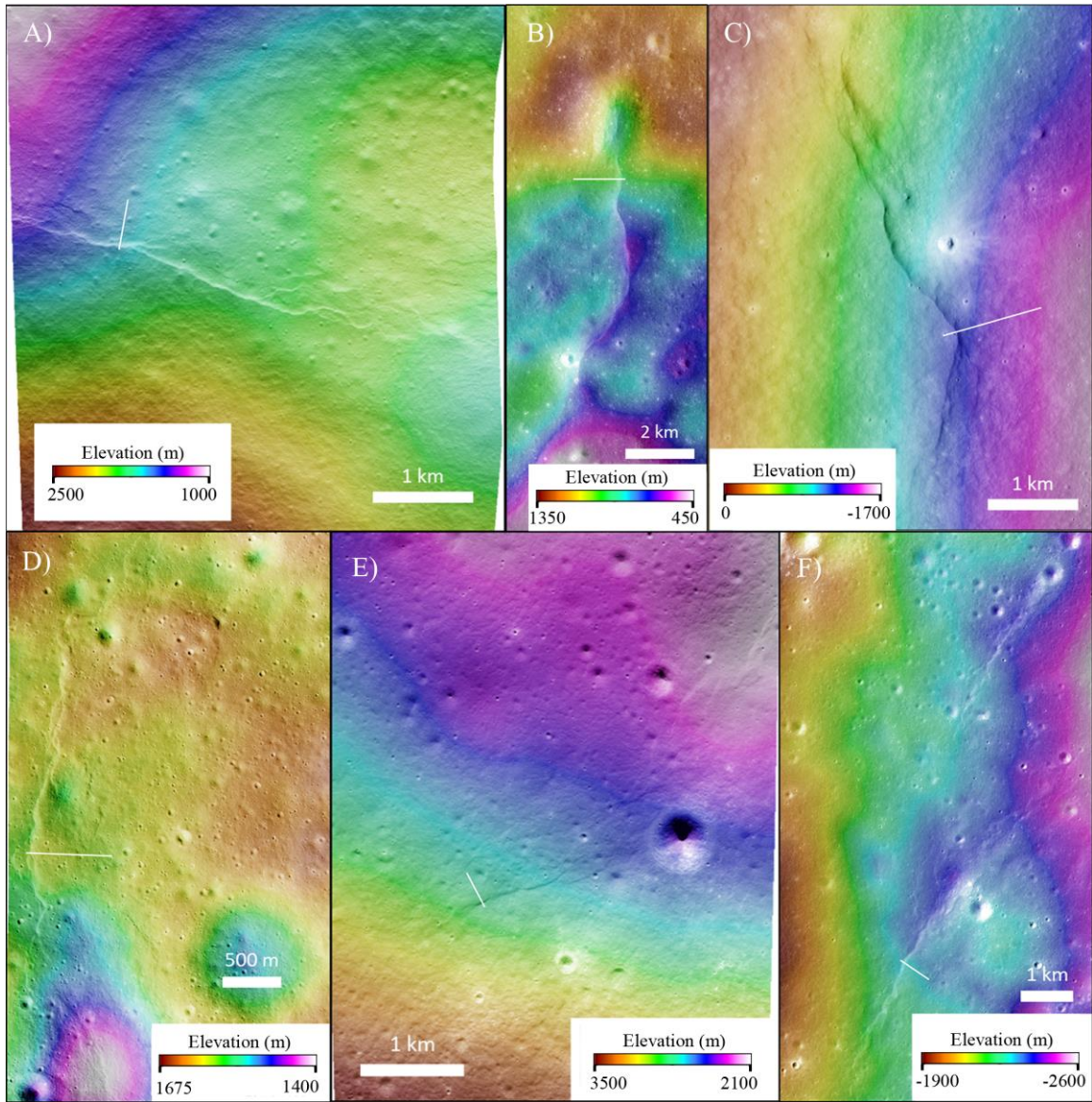
Fig. 18: LROC NAC DTM colorized shaded relief images of: A) Slipher, B) Racah X-1, C) Mandel'shtam A, D) Feoktistov, E) Simpelius-1, and F) Oppenheimer F. Profiles from Fig. 6 were taken along locations indicated by narrow white lines.

The Racah X-1 scarp (10.1°S, 178.1°E) has the largest maximum relief (~150 m) of any lunar lobate scarps measured to date [Banks *et al*., 2012] (Figs. 17B, 18B). The main scarp cuts across several tens of kilometers of undulating, densely-cratered highland terrain, making characterization of its morphology difficult. Several en echelon scarps

continue farther north of the DTM coverage up to and into Daedalus crater. At its northern end, the scarps transition into more complex wrinkle ridges on the flat floor of Daedelus. Such a morphologic transition is likely due to the contrast in mechanical properties, especially the presence of layering in mare basalts in Daedelus [Watters, 1991]. The en echelon complex also continues southward from the DTM area towards Aitken crater. Scarps in the Racah X complex typically trace N-S, with the main scarp face (vergent side) and many other segments oriented eastward. Like Slipher, small flat-floored troughs are present near and atop the Racah X-1 scarp [Banks et al., 2012].

The Mandel'shtam A lobate scarp (6.8°N, 161°E) was first identified in Apollo Panoramic Camera images (Figs. 17C, 18C) [Binder and Gunga, 1985]. It is one member of an arcuate scarp complex in Mandel'shtam crater starting in Mandel'shtam A crater and continuing 80 km north along the floor of Mandel'shtam. Scarps in this cluster typically trace N-S with scarp faces oriented westward. Maximum detrended relief of the Mandel'shtam A scarp is measured in the DTM at ~38 m. Some portions of the scarp face are terraced, indicating possible splay faults at each end.

The Feoktistov scarp (32°N, 140.6°E) is located in the highlands north of the small crater Feoktistov and approximately 60 km northwest of the outer rim of Mare Moscoviense (Figs. 17D, 18D). The main scarp trace appears braided and has a few antithetic scarps, indicating that the fault splays near the surface. The main scarp trends N-S with the vergent side of scarp oriented to the west. A small cluster of meter-scale troughs or graben occur in the hanging wall near the middle of the scarp, and are oriented at a high angle to the scarp face. The maximum relief of Feoktistov within the DTM is ~22 m, measured near the scarp's southern terminus.

Simpelius-1 (73.5°S, 13°E) is a cluster of relatively small, kilometer long, low-relief scarps on the wall and floor of the south side of Simpelius crater (Figs. 17E, 18E). The southern portion of the scarp cluster is covered by the available DTM and traces E-W along the wall of Simpelius crater. The vergent side of the scarp faces uphill to the south. Its maximum relief is approximately 13 m within the portion covered by the DTM [Banks et al., 2012].

Finally, Oppenheimer F (34°S, 160.9°W) is a simple en echelon complex of parallel linear scarps located north of the Oppenheimer F crater (Figs. 17F, 18F). The scarps trend NNE-SSW along the degraded outer rim of Apollo crater on the northern side of the South Pole-Aitken basin. The vergent sides of the scarps face to the west. Typical lengths of individual scarps are less than 5 km, and the en echelon complex of scarps continues for at least 60 km before continuous NAC image coverage ends.

Modeling Results

Profiles across representative sections of each scarp were extracted from NAC stereo derived DTM's. Faults are interpreted to dip from the base of a scarp face downward under the gently sloping back-limb. Coulomb fault dislocation models were iteratively created and compared to detrended profiles (Fig. 19) to determine sets of parameter values that predict similar scarp reliefs and slopes. Parameter ranges for each scarp profile are listed in Table 1. Best-fit dip angles range from 35-40°, depths range from 220-900 m, taper increments (for 5 steps) range from 50-250 m, and slips range from 18-62 m along the profiles modeled. Fault geometry is therefore dominant in controlling scarp topography.

44
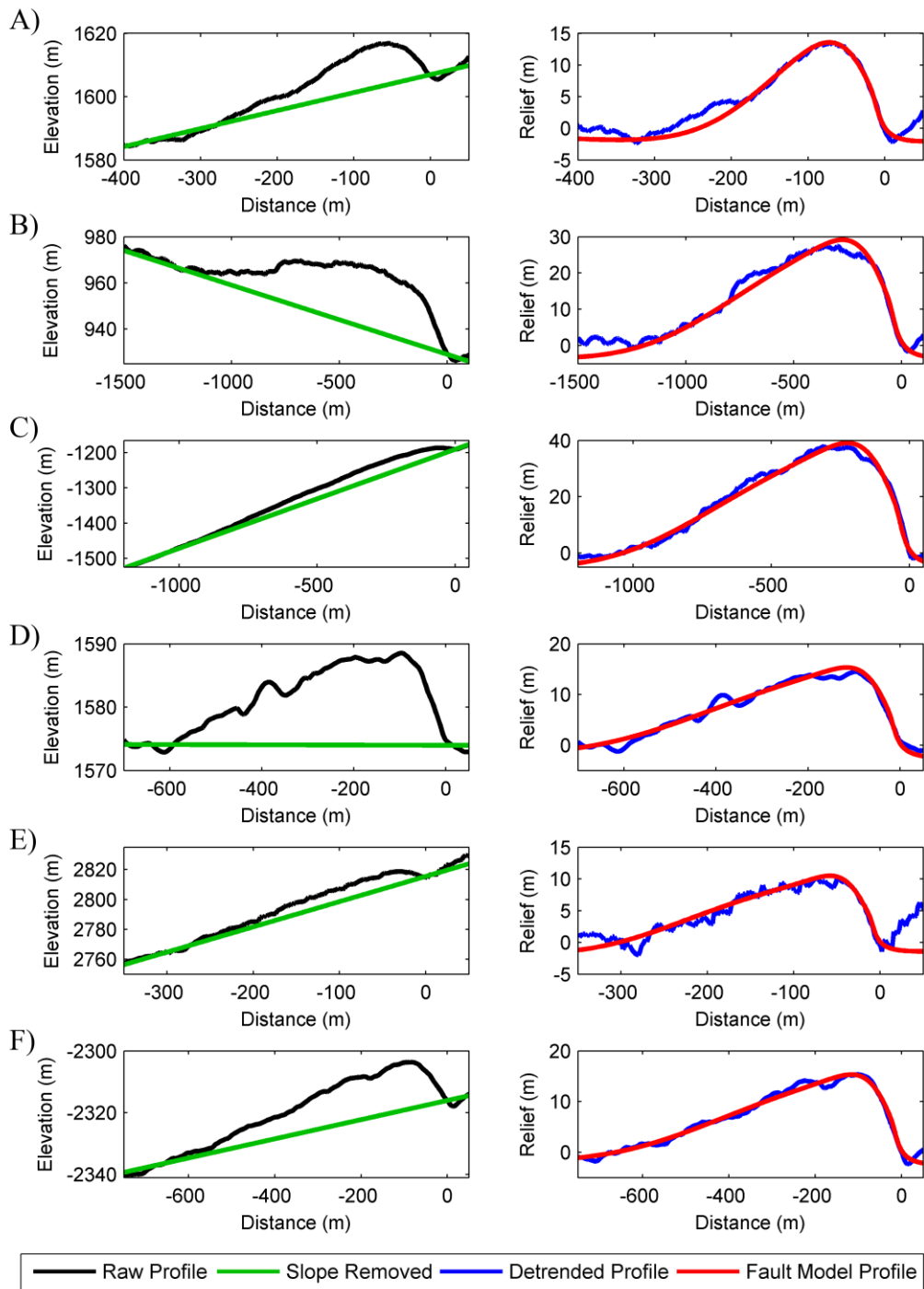
Fig. 19: Raw profiles, regional slopes removed, detrended profiles and best-fit fault dislocation models for profiles of: A) Slipher, B) Racah X-1, C) Mandel'shtam A, D) Feoktistov, E) Simpelius-1, and F) Oppenheimer F.

Scarp	Slip (m)	Dip (°)	Depth (m)	5-step taper increment (m)
Slipher	21±1	38±2	250±50	75
Racah X-1	45±2	38±3	900±50	250
Mandel'shtam A	62±3	37±2	770±25	200
Feoktistov	25±2	40±4	500±50	100
Simpelius-1	18±2	35±3	220±25	50
Oppenheimer F	25±2	40±3	500±50	100

Table 1: Best-fit model parameter results for profiles across scarps.

These ranges of lunar lobate scarp fault dips also constrain previous estimates of horizontal shortening across lunar lobate scarps. Banks *et al*. [2012] determined reliefs of scarps globally range from ~5-150 m, and assuming dip angles of 20-40°, predicted individual scarps may accommodate up to ~410 m of horizontal shortening. Lower limits of horizontal shortening (S_H) can be calculated via a simple kinematic model using measured maximum scarp reliefs (*h*) and fault plane dip angles (*θ*) [Wojtal, 1996; Watters and Robinson, 1999; Watters *et al*., 2000]:

$$S_H = h / tan(\theta) \ . \qquad (1)$$

Using a maximum measured scarp relief of 150 m [Banks *et al*., 2012] and my modeled range of fault plane dip angles of 35-40°, I estimate horizontal shortening of up

to 215 m across individual lunar lobate scarps, nearly half of the up to ~410 m shortening estimated by Banks *et al*. [2012] using smaller fault plane dig angles.

Stress State

The presence of a global population of near-surface faults on the Moon constrains the current state of lunar lithospheric stress [Binder and Gunga, 1985; Watters *et al*., 2010]. The compressional stress necessary to initiate thrust faulting can be determined by the Moon's near-surface strength. At least two approaches can be used to evaluate the near-surface shear strength of the lunar crust: frictional and rock mass criteria. Frictional strength is controlled by the resistance to brittle failure by sliding on randomly oriented, through-going fractures. Such fractures are likely in the heavily impacted upper crust of the Moon. The minimum horizontal stress required to initiate faulting can be given by:

$$\Delta\sigma_{xx} = (2*\mu_s*(\rho*g*z - p_w)) / ((1+\mu_s^2)^{1/2} - \mu_s) \ , \qquad (2)$$

where μ_s is the coefficient of static friction, ρ is the average rock density, g is gravitational acceleration, z is depth, and p_w is the pore pressure, which for the Moon is zero [Turcotte and Schubert, 2002]. The coefficient of static friction μ_s is estimated to be 0.85 by the empirical fit known as Byerlee's Law [Byerlee, 1978]. Using a density (ρ) of 2700 kg/m^3 and gravitational acceleration (g) of 1.624 m/s^2 [Binder and Gunga, 1985], I estimate the minimum frictional strength ($\Delta\sigma_{xx}$) in rock exceeded at modeled depths from 220 m and 900 m to be between 3.5 and 14.5 MPa (Fig. 20).
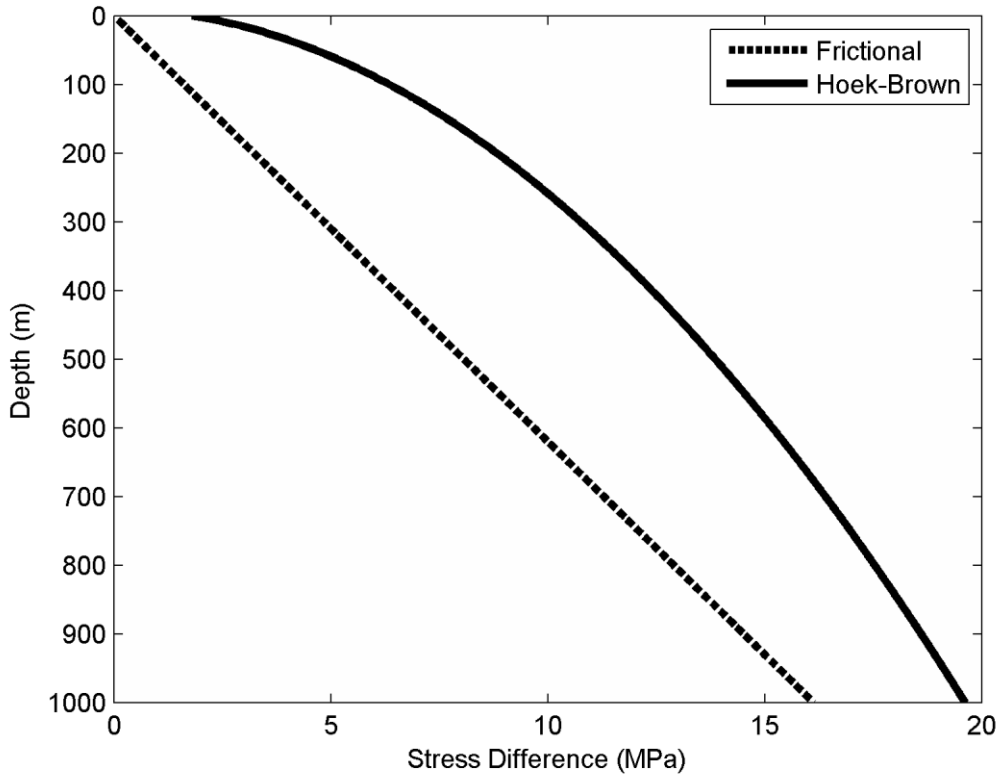
Fig. 20: Strength envelopes near the lunar surface. The frictional strength envelope was determined using the Turcutte and Schubert (2002) method. The Hoek-Brown strength envelope for non-zero cohesion was determined with material constants consistent with a highly disturbed anorthosite.

The frictional strength criterion assumes rocks have no cohesive strength, so it should be regarded as a minimum stress requirement. Rocks with cohesive strength may be better represented by the Hoek-Brown failure criteria [Hoek, 2001; Hoek *et al.*, 2002; Hoek and Diederichs, 2006]:

$$\sigma_1 = \sigma_3 + \sigma_{ci}*(m_b*\sigma_3/\sigma_{ci} + s)^a \ , \qquad (3)$$

$$\Delta\sigma_{xx} = \sigma_1 - \sigma_3 \ , \qquad (4)$$

48

such that σ_1 is the greatest compressional principal effective stress, σ_3 is the least

compressional principal effective stress, σ_{ci} is the intact rock strength, and m_b, m_i, a, and s

are material constants related to the Geological Strength Index (*GSI*) and the disturbance

factor *d* by:

$$m_b = m_i * e^{(GSI\text{-}100)/(28\text{-}14d)} \quad , \quad (5)$$

$$s = e^{(GSI\text{-}100)/(9\text{-}3d)} \quad , \quad (6)$$

$$a = {}^1\!/_2 + (e^{-GSI/15} - e^{-20/3})/6 \quad . \quad (7)$$

Using GSI = 45 consistent with highly jointed rock mass [Hoek *et al*., 2002; Watters *et*

al., 2011]; σ_{ci} = 190 MPa as an upper limit for anorthosite [Hustrulid and Bullock, 2001]

consistent with the 100-250 MPa expected for a typical very good quality hard rock mass

[Hoek, 2001]; medium-textured felsic igneous rock m_i =25 [Hoek, 2001]; and disturbance

factor *d* = 1.0 (where 0 is undisturbed and 1 is very disturbed/heavily fractured) [Hoek *et*

al., 2002], the cohesive rock mass strength ($\Delta\sigma_{xx}$) exceeded at 220 and 900 m depth is

between 9.2 and 18.6 MPa.

Discussion

      All six scarp models are consistent with deformation from thrust faulting at

typical dip angles of 35-40° and maximum faulting depths from a few hundred meters to

around a kilometer. Binder and Gunga (1985) previously used Apollo image

photoclinometry, shadow measurements, and half-angles of scarp trace curvature for

inferred conical (arcuate) faults to estimate dip angles for observed lunar lobate scarps at

17-30° (with an average of 21.4°) and maximum depths of 400 m to 3.8 km.

Additionally, their scaled sandbox experiments suggested dip angles of 25° and

maximum depths of 1-8 km based on an arcuate thrust fault theory. Curvature of scarp

traces is common, but not ubiquitous on the Moon. For example, the traces of the Slipher

and Oppenheimer F scarps are not arcuate, yet their morphology suggests a fault

geometry similar to other scarps. My modeled thrust fault dips (35-40°) are steeper and

my modeled depths (less than 1 km) are shallower, but do not assume an arcuate fault

geometry unrepresentative of the many linear or irregular lobate scarps traces [Binder and

Gunga, 1985; Watters *et al*., 2010; Banks *et al*., 2012]. My model results also fit reliefs

and slopes of the scarp face, crest, and back-limb instead of only maximum height.

The sub-kilometer depths modeled for lunar lobate scarp faults, as opposed to

more deeply rooted faults that extend to greater depths, suggest that they may be

restricted to weaker near-surface materials. Wilcox *et al*. (2005) show that regolith occurs

above an uneven, undulating fractured bedrock surface that grades up toward the surface

with decreasingly cohesive material, perhaps on the order of hundreds of meters to

kilometers. The megaregolith layer is weak enough for faults to grow within the upper

few hundred meters to a kilometer at stresses of 3.5-18.6 MPa. Areas with the most

pervasive fracturing, such as near large craters, might facilitate faulting due to decreased

rock strength [Sharpton and Head, 1988]. Scarps analyzed in this study occur both in

association with craters and in the highlands and variations in location and geologic

setting do not appear to have a significant influence on the results [Binder and Gunga,

1985; Watters *et al*.; 2010]. At greater depths, material strength of the megaregolith or

bedrock may be great enough that the current stress state is insufficient to allow for deeper fault propagation into a more coherent upper portion of the elastic lithosphere.

Lobate scarps also occur on other planetary bodies and have previously been modeled with geometries similar to my lunar scarp models. The lobate scarp Hinks Dorsum on asteroid 433 Eros has approximately 60 m of maximum relief and its subsidiary scarps have maximum reliefs of 25 m [Watters *et al*., 2011]. Fault dislocation models suggest that the main Hinks Dorsum fault has a dip of ~40°, maximum depth of 240 m, and a fault slip of ~90 m. Scarps subsidiary to Hinks Dorsum have modeled dips of ~35°, maximum depth of ~200 m, and slip of ~40 m [Watters *et al*., 2011]. The subsurface geometries of Hinks Dorsum and its subsidiary scarps fall within the range of values estimated for the lunar lobate scarps modeled in this study. Using equation 1 and the relief and dip values from Watters *et al*. [2011] yields 30-71.5 m of horizontal shortening for scarps on 433 Eros, also within the range I estimate for lunar lobate scarps. Eros' scarps are interpreted to have formed by compressional stresses during or shortly after a large nearby impact that formed a ~7.6 km diameter crater [Watters *et al*., 2011]; however, lunar lobate scarps do not appear to be associated with recent large impacts. Although the sources of stress are almost certainly different for lunar scarps versus those on Eros, the similar model geometries suggest that stress magnitudes and some material properties of the regoliths (*i.e.*, coefficient of static friction) on both bodies may be similar.

Lobate scarps on Mars and Mercury have maximum reliefs of up to a kilometer or more, but show similar morphologies to lunar scarps. Watters and Schultz (2002) created fault dislocation models for Discovery Rupes on Mercury and Amenthes Rupes on Mars

using listric fault geometries with dips that shallow with increasing depth; however, only a slight or no curve (±5°) in the fault fits the observed topography, planar faults fit best, and décollemont models with dips that that shallow to nearly horizontal fit poorest. The best-fit geometry of the Mercurian Discovery Rupes is a 30-35° dip with a maximum depth of 35-40 km and a fault slip of 2.2 km [Watters and Schultz, 2002; Watters et al., 2002]. The best-fit geometry of the Martian Amenthes Rupes is a 30° dip with a maximum depth of 25 km and a fault slip of 1.6 km [Schultz and Watters, 2001]. Due to order of magnitude smaller fault slips predicted for lunar scarps compared to those on Mars and Mercury, maximum depths of faulting are expected to be much shallower on the Moon, consistent with the model results presented above. However, the modeled dips of the Mercurian and Martian lobate fault scarps are comparable to lunar fault scarp models within ±5°.

The amounts of global radial contraction inferred from larger scarp populations on Mercury and Mars are similarly an order of magnitude greater than contraction estimates for the Moon. Previous studies have estimated the change in radius for Mercury to be at least 0.8 km [e.g., Watters *et al*., 1998; Watters *et al*., 2009; Watters and Nimmo, 2010] and for Mars to be between 112 m and 3.77 km [e.g., Mangold *et al*., 2000; Golombek *et al*., 2001; Golombek and Phillips, 2010; Nahm and Schultz, 2011]. The smaller magnitudes of slip and relief for lobate scarps on the Moon are consistent with recent estimates of lunar radial contraction of ~100 m [Watters *et al*., 2010; Banks *et al*., 2012].

The small but significant compressional strain across the global population of lunar lobate scarps is thought to be due to heat loss and planetary thermal contraction

over the Moon's history [Binder, 1985; Pritchard and Stevenson, 2000; Watters *et al*., 2010]. The lack of a latitude or longitude dependence on lobate scarps suggests that the Moon is in a state of net (perhaps isotropic) contraction. Relaxation of an early tidal bulge or tidal stresses raised solely by Earth would be predominantly extensional near the poles and compressional around the sub- and anti-Earth regions [Melosh, 1980]. Such a pattern is not observed, but tidal stresses may still play a secondary role in scarp formation (*i.e.*, influencing preferred orientation) [Watters *et al*., 2010]. Tidal stress raised solely by Earth would also only be on the order of tens of kPa [Weber *et al*., 2009], too low to initiate faulting by itself in 3.5-18.6 MPa-strength material [this study; Watters et al., 2010; Banks et al., 2012; Turcotte and Schubert, 2002].

Crater counts of mare basins crosscut by large-scale graben indicate that basin-related extension occurred before ~3.6 Ga [Lucchitta and Watkins, 1978; Solomon and Head, 1979]. Turning off of large-scale extension may result from superposition of increasing global contractional stresses via cooling, leading to a predominantly compressional regime thereafter [Solomon and Head, 1979]. Over the last ~3.5 Ga, global stresses would build and may have only exceeded rock mass strengths of 3.5-18.6 MPa in the geologically recent past, potentially explaining why lunar lobate scarps have ubiquitously fresh, crisp morphologies consistent with recent (<1 Ga) activity [Binder and Gunga, 1985; Watters *et al*., 2010]. Recently discovered young (<50 Ma) small-scale shallow graben on the lunar surface are consistent with localized extensional stresses of about 12 MPa in the presence of a low ~10 MPa background compressional stress, which may be relaxed by the formation of associated scarps where near-surface flexure results in extension in the area of the scarp back-limb [Watters *et al*., 2012]. The presence of

young graben in the back limb terrain suggests that some scarp deformation may be concurrent with shallow graben formation as recently as 50 Ma, and could possibly even continue today.

If the Moon was initially completely molten, radial contraction from cooling could be expected to have been on the order of a kilometer or more with stresses up to 350 MPa [Binder and Lange, 1980; Binder, 1982; Binder, 1985; Binder, 1986; Pritchard and Stevenson, 2000]. Our estimated 3.5-18.6 MPa of compressional stress necessary to initiate thrust faulting at the modeled depths (220 and 900 m, resp.) is consistent with thermal history models that predict small but significant global net compressional stresses (<100 MPa) that could arise from an initially hot exterior magma ocean superposed on a cooler interior [Solomon and Chaiken, 1976; Solomon and Head, 1979; Solomon and Head, 1980; Kirk and Stevenson, 1989; Pritchard and Stevenson, 2000]. The shallow faulting, which does not penetrate deeper into more coherent rock, further implies a low stress state consistent with only a small amount (~100 m) of net radial contraction of the Moon estimated from the global scarp population [Binder and Gunga, 1985; Watters *et. al.*, 2010].

3. EVIDENCE FOR AN EXPLOSIVE ORIGIN OF CENTRAL PIT CRATERS ON MARS

Background

       Central pits occur in many impact structures on Mars and exhibit a crater-in-crater configuration [*e.g.*: Smith, 1976; Hodges, 1978; Barlow, 2006, 2010] (Fig. 21). Kilometer-scale central pits have been identified on the floors or on tops of the central peaks of over 1,000 Martian impact craters with diameters as large as 125 km in diameter and down to as small as 5 km in diameter [Smith, 1976; Barlow and Bradley, 1990; Barlow *et al.*, 2000; Barlow, 2011], although some smaller central pits have also been identified [Barlow, 2010]. In this study, I focus on "floor pits" that are deeper than the surrounding floor of their host craters, as opposed to "summit pits" that occur atop the central peaks and have floors at higher elevations than their host crater floors, to avoid potential bias in my thermal methods due to coherent rock or boulders on the sides of the central peaks. Based an ongoing survey by Barlow [2010, 2011] and this study, central floor pits have a median diameter of 0.16-0.175 host crater radii, such that a 50 km diameter crater might have a central pit ~8 km wide. Their depths range from very shallow to over 1.5 km below the surrounding impact crater floor, measured using Mars Orbiter Laser Altimeter data [Smith *et al.*, 2001] for a few of the largest central pits [this study].
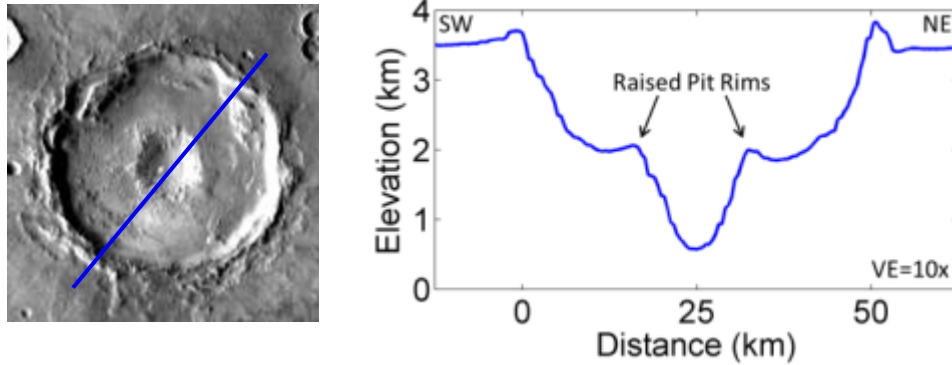
Fig. 21: THEMIS daytime IR mosaic of a 50 km diameter unnamed Martian impact crater containing a central pit at 296.4°E, 17.6°S. A MOLA topographic profile across the center shows typical pit morphology.

Central pit craters on Mars are confined to low and mid-latitudes, within ±70° of the Martian equator [Hodges *et al*., 1980; Barlow, 2011; Garner and Barlow, 2012]. They are also common for impact craters on icy satellites, including Ganymede and Callisto [Smith *et al*., 1979]. Central pits are seldom observed on rocky planets other than Mars, although a few dozen are present on Mercury [Schultz, 1988; Xiao and Komatsu, 2013] and the Moon [Croft, 1981; Schultz, 1976a, 1976b, 1988; Xiao *et al*., 2014]. As a result, several proposed models require water to play a leading role in forming central pits.

The presence of water-ice has been believed to be involved in typical pit formation for decades [Hodges *et al*., 1980; Croft, 1981]. Although water-ice is not stable at the surface of Mars within the low latitudes today [Clifford and Hillel, 1983; Mellon *et al*., 1997; Head *et al*., 2003], water was (and may still be) present within the upper few meters to kilometers of the surface even at low latitudes earlier in Mars' history. The possibility of significant subsurface water in pre-impact terrains is supported by the presence of layered ejecta surrounding many fresh Martian impact craters [Carr *et al*., 1977; Gault and Greeley, 1978; Wohletz and Sheridan, 1983; Barlow *et al*., 2000; Baloga

56

et al., 2005] and Mars Odyssey Gamma Ray Spectrometer spectra [Boynton *et al.*, 2007]. However, the process(es) responsible for forming central pits in impact craters and the role of water are still debated, and several mechanisms for pit formation have previously been proposed.

Wood *et al.* [1978] proposed that explosive decompression may volatilize a subsurface water-rich layer, causing steam explosions and removing the core of central peaks. However, this explosive model suffers from the difficulty of keeping water vapor from escaping early in the impact process before a central pit can be preserved [Croft, 1981; Pierazzo *et al.*, 2005; Senft and Stewart, 2011; Elder *et al.*, 2012].

Croft [1981], Bray [2009], Senft and Stewart [2011], Alzate and Barlow [2011] and Elder *et al.* [2012] proposed that central pits could form by the melting then gravitational drainage of target water-ice through fractures underlying central uplifts. This model provides a low-energy solution to forming central pits long enough after impact that they should be preserved.However, raised rims are also associated with many Martian central pits [Wood *et al.*, 1978; Garner and Barlow, 2012] and would not be expected with drainage structures. These models also require large volumes of water to be drained, nearly equal to the volumes of the central pits plus any initial central peaks, which is unrealistic for forming the central pits on the Moon and Mercury assuming pits there form by the same mechanism as on Mars. Numerical simulations of the melt-drainage model have also only been successful in predicting central pits when conducted for pure-ice targets.

Passey and Shoemaker [1982], Greeley *et al.* [1982], and Bray *et al.* [2012] proposed that central peaks of impacts in weak target materials may collapse to form

central pits. This model explains the destruction of central peaks in craters that might otherwise have them. However, the abundance of impact craters with central peaks and summit pits in the same regions as impact craters with floor pits suggests that the target material should be strong enough to prevent collapse [Barlow, 2011].

Greeley *et al*. [1982] proposed and demonstrated in laboratory experiments that small-scale central pits can be excavated from impacts into layered targets, causing central peaks to detach, rise directly upwards, and fall back into the crater bowl forming a central secondary pit. This model does not require a target to be water-bearing, consistent with the presence of a small number of central pits on Mercury and the Moon, although a water-bearing layer could provide an enhancing strength contrast. However, scaling up to planetary impact craters with diameters of tens of kilometers is problematic because of the scale-dependent magnitude of gravitational versus strength-limited late-stage impact modification, greatly reducing the influence of any layer strength differences on the final crater morphology [Croft, 1981].

Schultz [1988] proposed that central pits are excavated as a primary result of impacts with low-velocity bolides. This model also does not require a target to be water-bearing, and implies that the presence yet relative scarcity of central pits on Mercury and the Moon compared to icy satellites is due to higher average impact velocities in the inner solar system. However, Schultz [1988] assumes that post-impact modification is only weakly dependent on crater size, which becomes an issue for craters with diameters of tens of kilometers [Croft, 1981].

Each of the above models has both strengths and weaknesses. I provide another set of observations to test these models using new thermal observations and test for the

58

presence of absence of ejecta. For this study, I broadly group the previously proposed

mechanisms for pit formation into those that explosively eject pit material up and

outward [*e.g.*: Wood *et al*., 1978; Greeley *et al*., 1982; Schultz, 1988] versus those that

drain or collapse material downward [*e.g.*: Croft, 1981; Passey and Shoemaker, 1982].

During a crater-forming explosion, rocks and boulders are ejected out of the crater, layers

are proximally uplifted and overturned, and ejecta are draped over the surrounding

surface [*e.g.* Melosh, 1989]. Raised rims can be formed by both the addition of ejecta

[e.g. White and Ross, 2011] and structural uplift [Sharpton, 2014], although the latter

indicates that the uplift is the greatest contributor to raised impact rims for impacts. The

average grain size for ejecta decreases with radial distance from the crater, such that the

largest clasts or blocks are proximal to the crater rim [*e.g.*: Gault *et al*., 1963; O'Keefe

and Ahrens, 1985; Melosh, 1989; Buhl *et al*., 2014]. Conversely, drainage and collapse

features such as sinkholes, which are typical of karst landscapes, and lava tube skylights

form by gravitational collapse and do not create raised rims nor emplace material atop

their rims [*e.g.*, Okubo and Martel, 1998; Salvati and Sasowsky, 2002; Cushing *et al*.,

2007; Robinson *et al*., 2012]. The presence or absence of pit-derived ejecta around

central pits therefore provides one way to distinguish between explosive versus drainage

and collapse scenarios for the formation of central pits.

I use the presence or absence of decreasing average grain size with distance from

pits as the indicator of possible pit-derived ejecta. I hypothesize that central pits are

formed by explosive excavation or devolatilization during or after impact. The Wood *et*

al. [1978], Greeley *et al*. [1982] and Schultz [1988] models would be supported by the

presence of pit-derived ejecta, and the Croft [1981] and Passey and Shoemaker [1982]

models would not be supported. After analyzing the results, I also address the weakness of previous explosive formation models to produce central pits late enough in the impact process to be preserved, by presenting an alternative "melt contact model" for central pit formation late in the impact process. Finally, I apply my integrated observations to interpret the morphology and thermal properties of central pits in the context of central uplifts and propose testable predictions for the model.

Data and Methods

For this study, I surveyed impact craters > ~10 km in and identified containing central floor pits within ±60° latitude of the Martian equator using the Java-based planetary geographic information system program JMARS [Christensen *et al*., 2009]. Central pits were identified as distinctive circular depressions in the center of an impact crater that appeared to be deeper than the host crater floor based on the available imaging and topography. Many small impact craters with diameters <10 km containing central depressions were excluded from this survey due to poor spatial resolution, as well as craters I could not confidently determine had depressions deeper than the host floor. I excluded summit pits that occur atop central peaks and are not deeper than the host crater floor to avoid potential bias from coherent rock or boulders exposed on or eroding out of the sides of the central peaks. I also excluded structures considered to be peak rings for large host craters with diameter of several tens of kilometers, and concentric terraces, especially in craters near the Martian simple to complex crater transition of ~6-7 km diameter [Garvin *et al*., 2000, 2003].

Diameters were measured for both the central pits and their host craters. Only the largest central pits are resolved in the 128 pixel/deg (460 m/px) Mars Orbiter Laser Altimeter (MOLA) global mosaic [Smith *et al*., 2001], so the ~100 m/pixel Mars Odyssey mission Thermal Emission Imaging Spectrometer (THEMIS) [Christensen *et al*., 2004] calibrated daytime infrared (IR) global mosaic [Edwards *et al*., 2011] was used for most craters, which provides nearly complete (~90%) coverage to ±60° latitude. THEMIS daytime IR images show topography as shading, since sun-facing slopes are warmer and have the highest pixel values, while slopes facing away from the sun or those in shade are coolest and have the lowest pixel values. Higher resolution visible images were also used to observe finer-scale morphology and distinguish central morphologies that appeared ambiguous in THEMIS daytime IR. Primarily, I used Mars Reconnaissance Orbiter mission Context Camera (CTX) [Malin *et al*., 2007; Bell *et al*., 2013] images at ~6 m/pixel that were map-projected and photometrically stretched from Planetary Data System (PDS) raw electronic data records, and where available I used High Resolution Imaging Science Experiment (HiRISE) [McEwen *et al*., 2007] images at ~ 0.25 to 1.3 m/pixel that were map-projected and photometrically stretched from PDS calibrated reduced data records. The global dust environment for central pit crater context is shown using Thermal Emission Spectrometer (TES) solar energy reflectivity (albedo) integrated from 0.3 to 2.9 μm [Christensen *et al*., 2001].

During the formation of impact and other explosive craters, coarse debris are typically ejected and scattered outside the crater. Large blocks and coarse grains have a higher thermal inertia than finer-grained materials and hold on to their heat longer through the night. Thermal conductivity, a function of grain size, varies by 3-4 orders of

magnitude more than density and specific heat for geologic materials under Martian atmospheric conditions. As a result, thermal inertia calculated from nighttime thermal images can be used to estimate changes in average grain size [Christensen, 1986]. I therefore used the THEMIS thermal inertia global mosaic as a quantitative proxy for average grain size, such that coarse-grained or blocky materials have relatively higher thermal inertias (warmer at night) while dust, sand, and other fine-grained materials have lower thermal inertias (cooler at night) [Christensen, 1986; Fergason *et al*., 2006; Edwards *et al*., 2009, 2011]. THEMIS nighttime images and thermal inertias have previously been used to identify blocky ejecta rays from impact craters on Mars that otherwise show little or no albedo variation in visible images but where grain size trends are seen with respect to distance from the crater [McEwen *et al*., 2005; Tornabene *et al*., 2006]. Central pits with an annulus or a geographically skewed patch of higher thermal inertia material nearer the pit rim than more distally across the surrounding host crater floor may be classified as having a fining average grain size with radial distance, consistent with ejecta.

To measure the trend of thermal inertias, I circumferentially averaged the THEMIS thermal inertia mosaic over central pit craters in intervals of 0.1 host crater radii. Because most central pits are <0.2 crater radii, I compared pit-proximal averaged thermal inertia values within the interval from 0.2-0.3 crater radii versus more distal averaged thermal inertia values at 0.5-0.6 crater radii. A Student's t-test was then performed on the differences between proximal and distal averaged thermal inertias for the population of central pits. A significance level of $P \geq 0.05$ would be deemed not statistically significant and served as my null hypothesis: thermal inertia and average

62

grain size do not decrease radially away from pit rims. For P<0.05, a radial decrease in thermal inertia with distance from the pit rim would be deemed statistically significant and would reject the null hypothesis and support an alternative hypothesis that ejecta surrounds central pits.

Results

I identified central floor pits within 654 host craters ~10 km diameter or larger between ±60° latitude of the Martian equator (Fig. 22). Additional smaller craters with central pits exist [Barlow, 2010, 2011], but are not well-resolved in the THEMIS thermal images used for this study. MOLA topographic profiles have very coarse resolution and may only provide topographic insight to the largest central pit craters (Fig. 21), and sometimes show complete and partially rimmed pits that frequently occur in the highlands terrains [Garner and Barlow, 2012]. I identified central pits in host impact craters with diameters ranging from ~8 to 114 km, with 95% of those host craters being <50 km in diameter and excluding smaller potential central pit craters. The surveyed central pits have a median diameter ratio to their host craters of 0.175 with a standard deviation of 0.037 (Fig. 23). These results are comparable to the median ratio of 0.16 found by Barlow [2011].
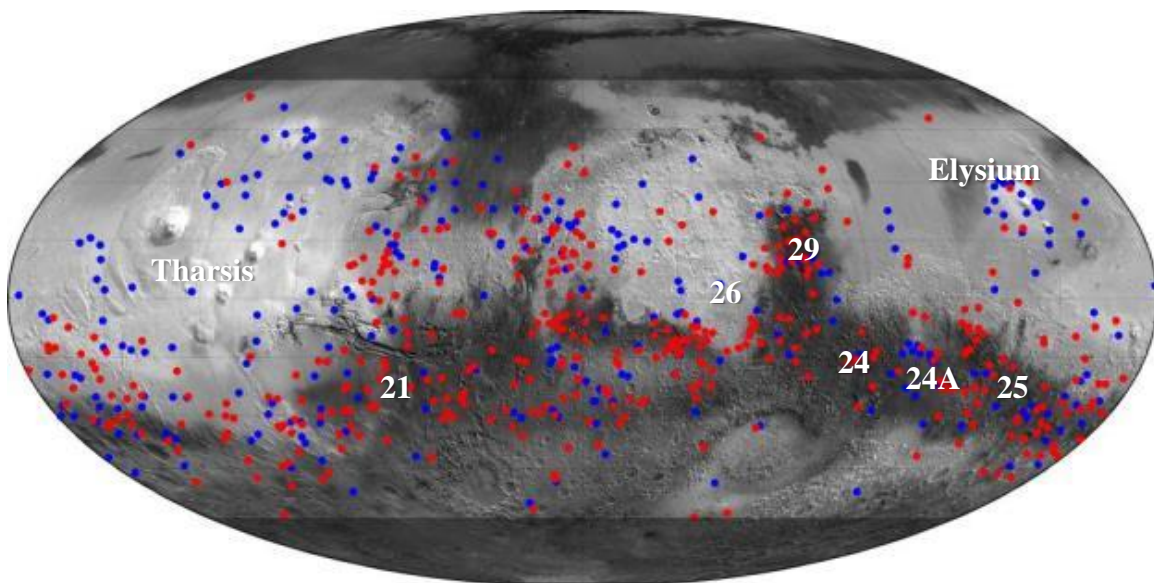
● Pits w/ Decreasing Thermal Inertia Trend (n=395, 62%)
● Pits w/o Decreasing Thermal Inertia Trend (n=240, 38%)

Fig. 22: Distribution of 654 central pit craters identified in this survey of the THEMIS daytime global mosaic, within ±60° degrees of the Martian equator, overlain on the TES albedo basemap [Christensen *et al*., 2001] and presented in a Mollweide equal area projection. Locations of Figs. 1, 4A, 4B, 5, 6, and 9 are highlighted. The Tharsis and Elysium regions are also labeled, where coatings of dust mask most central pit thermal signatures.
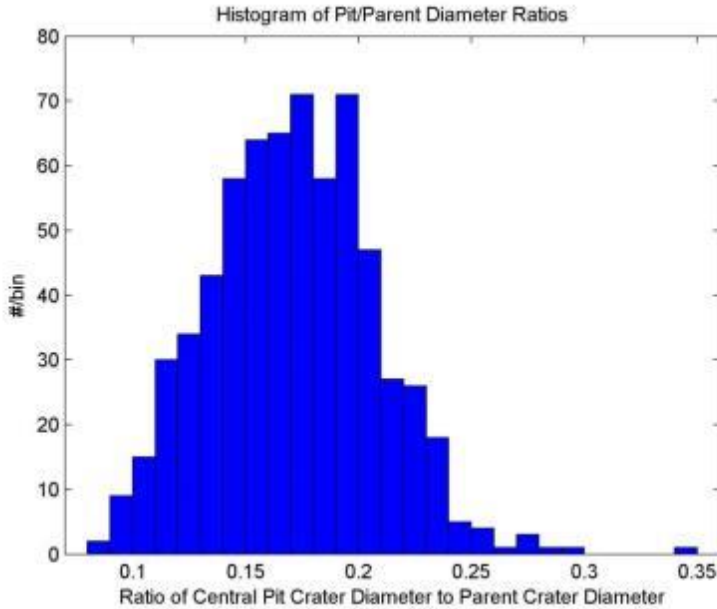
Fig. 23: Histogram showing the range of diameter ratios between central pits and their host craters. The median value is 0.175 with a standard deviation of 0.037.

Based on THEMIS-derived thermal inertias, most central pits showed higher thermal inertia (coarser) material near their rim than more distally on the host crater floor (*e.g.* Fig. 24). 635 of the 654 central pits had thermal images over their host crater floors. A number of observations can be seen in my data. A majority of CPCs (62%, n=395) show radially decreasing thermal inertia trends outside the pits. That percentage increases to 76% (254 of 333) with increasing host crater diameter (>20 km). Restricting the selection of central pits craters to those with absolute thermal inertia values >300 TIU (coarser than medium-grained sand and dust), independent of crater diameter, increases the percentage to 80% (175 of 216). Central pit craters with both host crater diameters >20 km and absolute thermal inertia values >300 TIU increases the percentage to 89% (74 of 83). Pits with proximal high and radially decreasing thermal inertias in THEMIS images show large blocky debris (up to tens of meters wide) in visible CTX and HiRISE

65

images (Fig. 25), while pits that did not show proximally high nor decreasing thermal

inertias appear blanketed or mantled (Fig. 26).
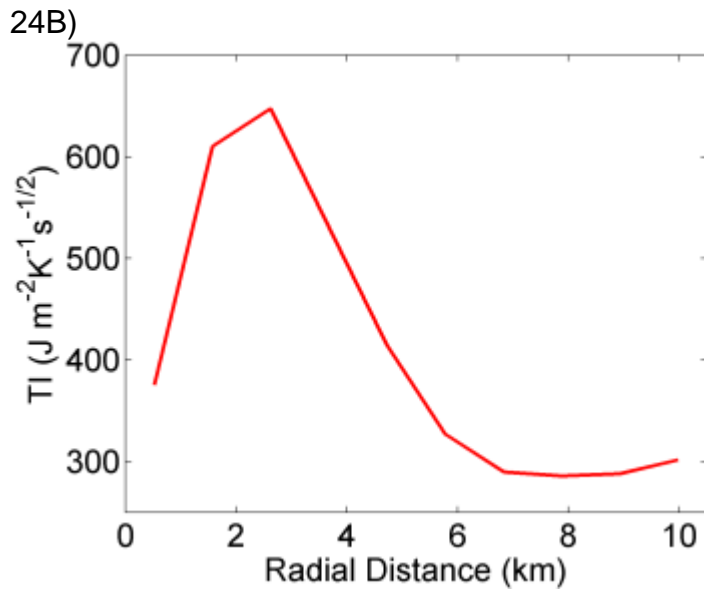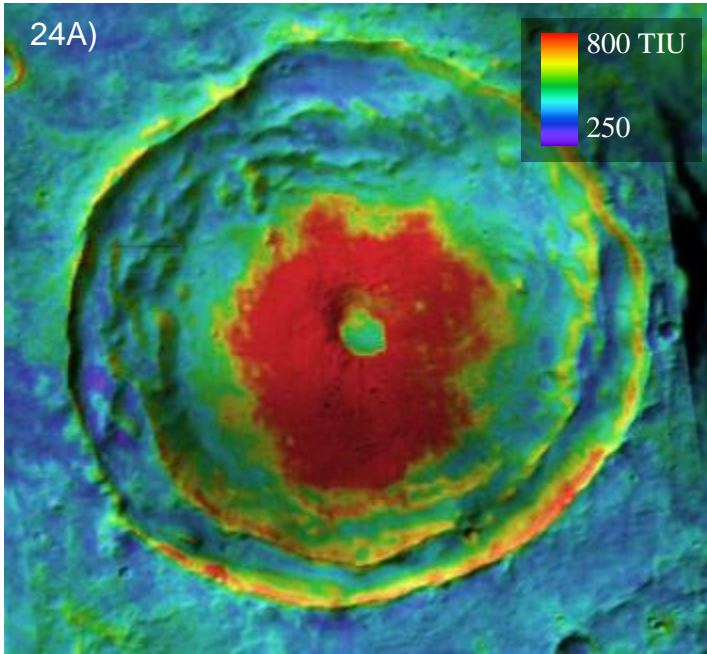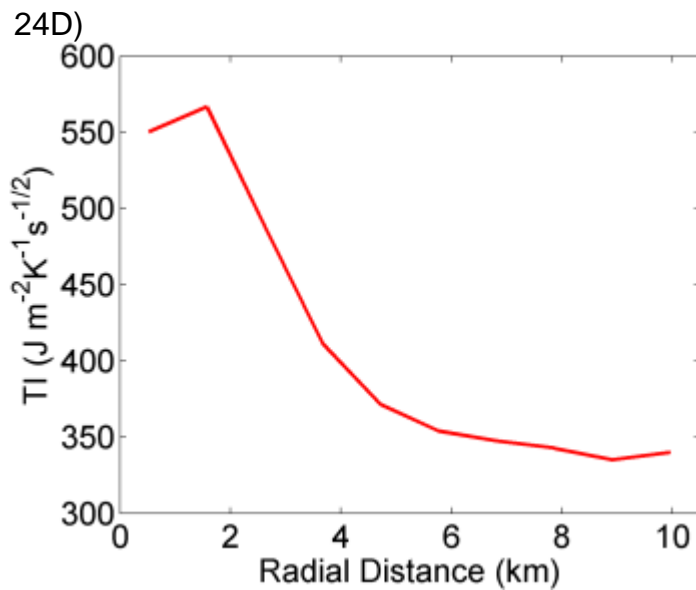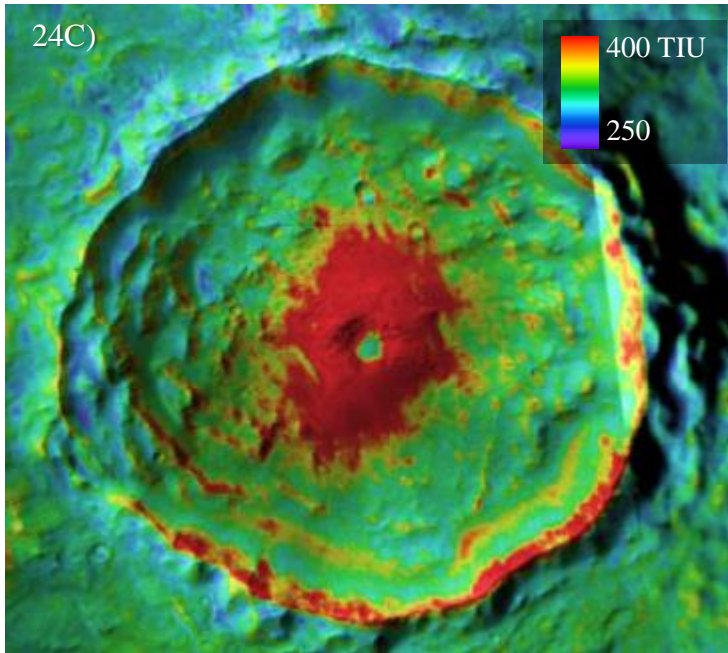
Fig. 24: THEMIS nighttime (color) and CTX visible (shading) images showing radially decreasing high thermal inertia material interpreted as ejecta surrounding two central pit craters at 24A) 18.4°S, 102.7°E, and 24C) 14.9°S, 93.2°E. Color scales indicate thermal inertia values. Panels 24B) and 24D) show the radially decreasing thermal inertia trends for the central pit craters in 24A) and 24C), resp.
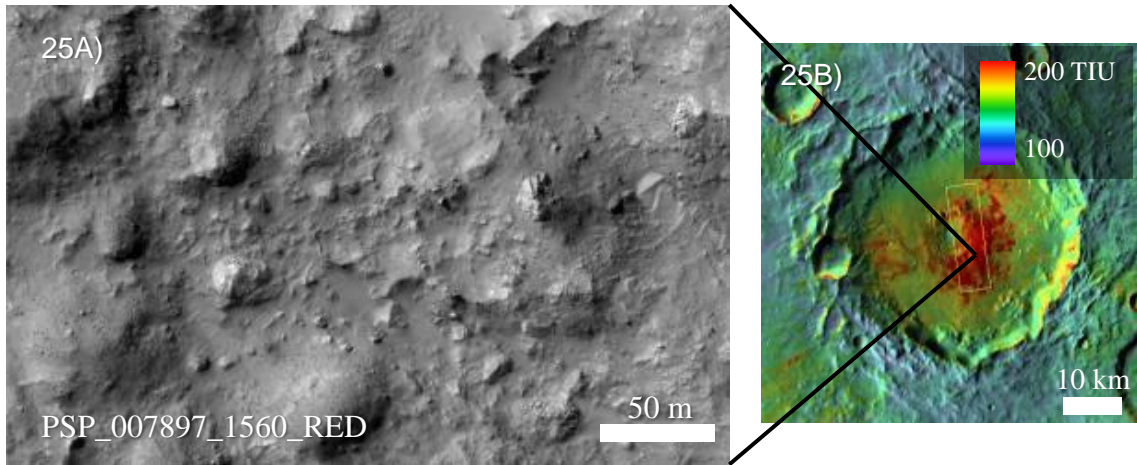
Fig. 25: 5A) HiRISE image showing large blocks near a central pit crater at 23.8°S, 126.8°E. 5B) THEMIS nighttime IR (color) over daytime IR (shading) context image showing high-thermal inertia material inferred as being blocky and confirmed by the HiRISE image. Black lines indicate location of A. Yellow box in B indicates footprint of HiRISE image.
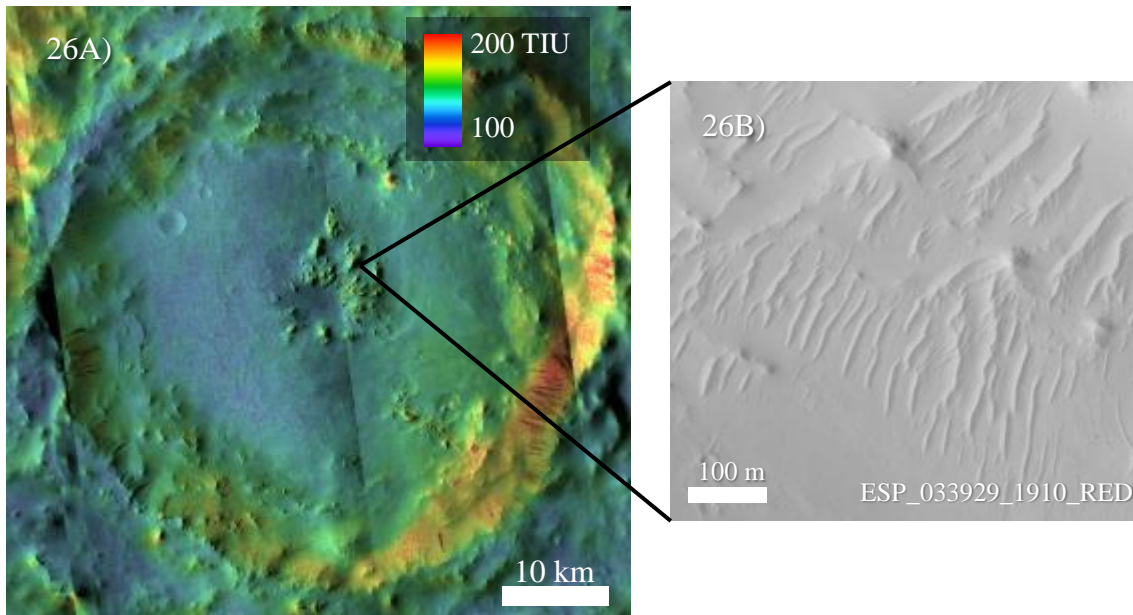
Fig. 26: A) THEMIS nighttime IR (color) over CTX visible (shading) image showing a central pit crater at 10.9°N, 50.8°E without a radially decreasing thermal inertia. Average thermal inertia values are uniformly low across the crater floor and associated with a coating of fine-grained dust. B) HiRISE visible image enlargement of an area near the central pit showing low-contrast dust mantling the terrain.

I conducted a paired Student's t-test to determine the confidence interval of the measured thermal inertia decreases from 0.2-0.3 crater radii to 0.5-0.6 crater radii. For the 635 central pit craters with thermal images, the t-test returns a $P<0.01$ indicating extreme statistical significance. I therefore reject the null hypothesis that thermal inertia and average grain size do not decrease radially away from pit rims, and adopt an alternative hypothesis that pits are surrounded by ejecta with grain size decreasing with distance away from the pit.

The median proximal thermal inertia for central pits with radially decreasing thermal inertias is 283 thermal inertia units (1 TIU = 1 $J\ m^{-2}K^{-1}s^{-1/2}$) with a standard deviation of 121 TIU, while the median proximal thermal inertia for central pits with

other, radially non-decreasing thermal inertia trends is 205 TIU with a standard deviation of 145 TIU (Fig. 27). Central pits lacking the radially decreasing trends are more common in Tharsis, Elysium, and other dusty regions characterized by high TES albedos and low thermal inertia values (blue dots around "Tharsis" and "Elysium" in Fig. 22).

Fig. 27: Histogram and box-and-whisker plot of central pit craters exhibiting radially decreasing thermal inertia trends (red) and radially non-decreasing thermal inertia trends (blue) plotted against THEMIS thermal inertia values. Lower thermal inertias are indicative of finer average grain size and dustiness.

Smaller central pits also tend not to show radially decreasing thermal inertias (Fig. 28). Based on the population of impact craters observed with THEMIS data, the median diameter for host craters containing pits with warm material is ~23.3 km and the median diameter for craters with pits lacking it is ~16.7 km, both cases being above the simple/complex transition of 6-7 km for Martian craters [Garvin *et al*., 2000, 2003].

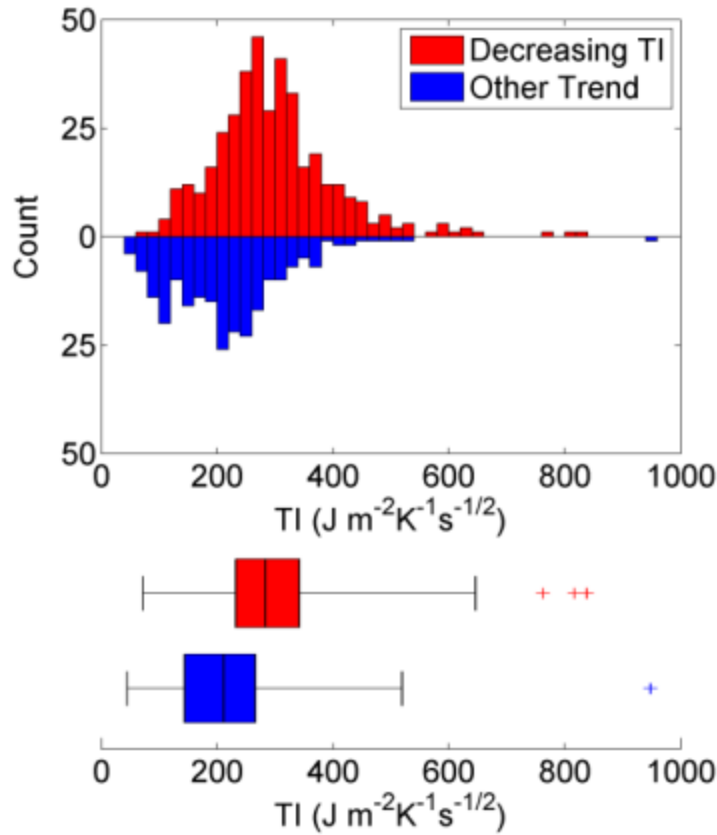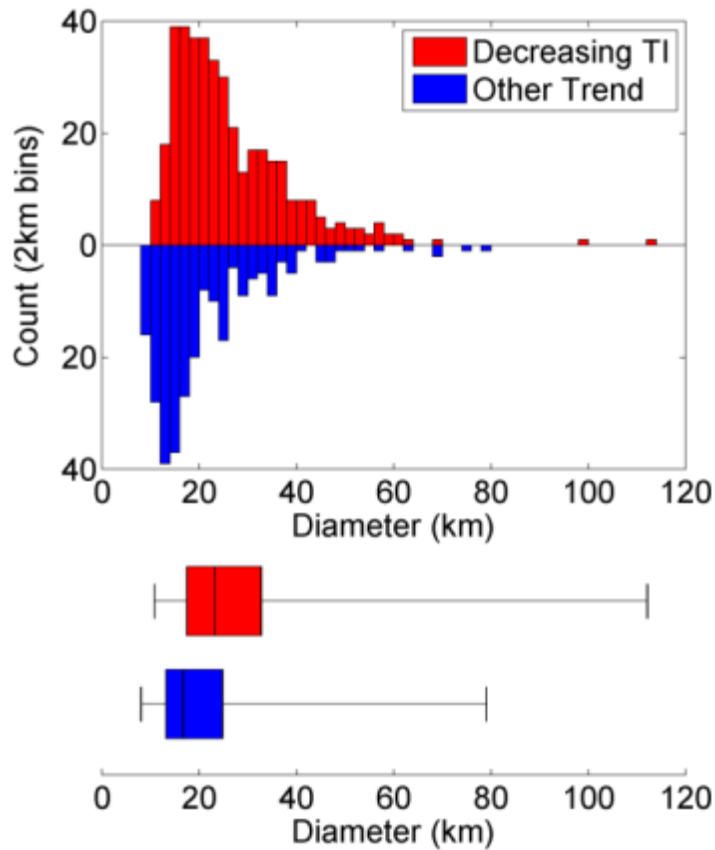Fig. 28: Histogram and box-and-whisker plot of craters containing central pits exhibiting radially decreasing thermal inertia trends (red) and radially non-decreasing thermal inertia trends (blue) plotted against host crater diameter.

Discussion

The raised rims around some pits [Wood, 1978; Garner and Barlow, 2012] are suggestive of explosive excavation, similar to their host craters, which also have raised rims. As discussed by Garner and Barlow [2012], raised rims are more frequently observed in larger central pits than smaller ones. They also argue that the preferred distribution of rimmed pits in highlands regions and non-rimmed pits in volcanic plains suggests that target material strength and/or volatile content may also limit the expression of raised rims. Some very small scale pits on Mars believed to have formed from volatile release in impact melt have been identified and also exhibit slightly raised rims, although they are not exclusive to crater centers and do not exhibit well-defined ejecta [Tornabene *et al*., 2012; Boyce *et al*., 2012]. Surfaces visible in some CTX and HiRISE images show large (meter-scale) blocks in warm patches adjacent to central pits (*e.g.,* Fig. 25), consistent with the expected correlation between warm material and coarse surfaces. Such blocks and megablocks are commonly observed near impact craters, including at the Ries crater in Germany [*e.g*. Gault *et al*., 1963] and at some Martian craters [*e.g.,* Caudill *et al*., 2012]. Combined with the spatial correlation of warm material and central pits, I interpret the blocks scattered around central pits to be explosively-emplaced pit ejecta.

The observability of high thermal inertia, coarse-grained material appears linked to the size of the pit. Small craters excavate smaller volumes of material that is finer-grained on average than larger craters [*e.g*.: Gault *et al*., 1963; O'Keefe and Ahrens, 1985; Melosh, 1989; Buhl *et al*., 2014]. Fine-grained rocks are more easily eroded or buried than coarser-grained rocks, so the coarser ejecta at larger pits should be

preferentially preserved and less buried. Surface diurnal thermal inertias are sensitive to materials within a few thermal skin depths (several centimeters) of the surface, so any ejecta would have to be buried by no more than a few centimeters of dust in order to be observable. Accumulated dust and sand is frequently observed on Mars and is indicated in my analysis as low thermal inertia values due to dust's fine grain size (Fig. 26). The smaller grain size distribution of ejecta for smaller craters is therefore expected to decrease the positive detection of ejecta using diurnal thermal inertias.

The presence of high thermal inertia material on host crater floors near pits would not necessarily need to be due to pit-derived ejecta. To avoid many false-positives, I have calculated the trend in thermal inertia (grain size) with radial distance from the pit. For example, post-impact lava or perhaps impact melt flows occur on the floors of some craters containing central and have high thermal inertias, although small flow lobes are easily distinguishable (Fig. 29), and much more extensive lava or impact melt flows could potentially fill central pits. I expect impact melt ponds to be distributed throughout the crater floor, so measuring a radially decreasing trend in thermal inertia as opposed to only using high thermal inertia values avoids this problem in most cases.

Mass wasting of material off the host crater wall is also unlikely to cause a radially decreasing thermal inertia trend, as the coarsest materials slumping off the wall should be distributed closer to the source walls and far from central pits, instead making a radially increasing trend. Similarly, I expect that blocky material transported fluvially or glacially from outside the crater and down the crater walls should be preferentially deposited with the coarsest grains near the break in slope at the base of the crater wall, far from central pits. If a central peak did form and shed material before the peak's

destruction, that material might be manifested on the floor of the host crater at the base of the now-destroyed central peak. However, I expect any gravitational or fluid-driven transport of such peak material would be very limited before collapse of any central peaks to possibly form pits. Patchy or partial erosional uncovering of consolidated host crater fill rocks could also explain higher thermal inertias relative to the surrounding crater floor; however, I consider the selective removal of significant amounts of dust from the centers of host craters, but not in the dusty plains surrounding many host craters, to be unlikely. Additionally, significant erosion on the host crater floor is inconsistent with the presence and preservation of raised rims around many central pits. Thermal inertias are also low for relatively fine-grained aeolian dunes or other bedforms that often form in the centers of craters, and confirmed in CTX and HiRISE images (Fig. 26).
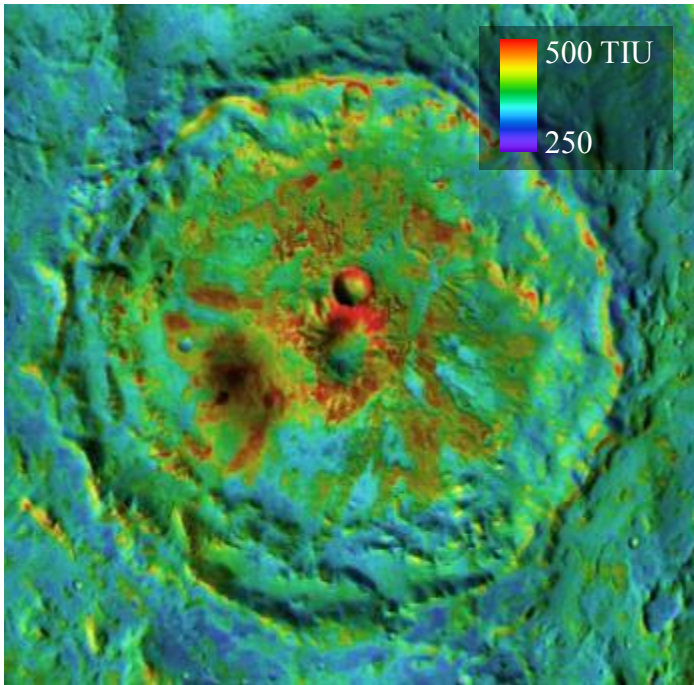
Fig. 29: THEMIS nighttime IR (color) over CTX visible (shading) image showing high thermal inertia lava or impact melt flow lobes (red, oranges, and yellow irregular bands on crater floor) on the floor of an impact crater containing a central pit at 28.5°N, 83.4°E.

For central pit craters on Mars, the radial decrease of thermal inertia is consistent with and supports the Wood *et al*. [1978], Greeley *et al.* [1982], and Schultz [1988] explosive models that would each emplace pit-derived ejecta around them, and the thermal inertia trend does not support the drainage and collapse models of Croft [1981] and Passey and Shoemaker [1982] that do not predict a distribution of pit-derived ejecta. However, each explosive model also suffers from a critical weakness. The Wood *et al*. [1978] model for an explosive pit origin suffers from the difficulty of keeping vapor from escaping early in the impact process before a pit can be preserved. The Greeley *et al*. [1982] central peak detachment model also suffers from issues scaling up from the laboratory to planetary impact craters. The Schultz [1988] low velocity impact model also suffers from scaling issues with respect to crater modification and material strength.

75

Alternatively, an explosive reaction could potentially result from mixing of water-ice and molten rock through several mechanisms. For example, a post-impact magmatic intrusion could intrude into a crater and react with the ground water as a maar volcano [Wohletz, 1986; Begét *et al*., 1996]; however, I would not expect such a scenario to consistently form pits in crater centers. Heavy fracturing and brecciation during the impact process may allow fluids (either impact melt, or liquid water) to mobilize and permeate the substrate and come into contact with each other, similar to the fluid flow described by Elder *et al*. [2012]. Although liquid water may move freely through fractures, Elder *et al*. finds that impact melt would cool too quickly due to its high melting temperature and larger temperature difference with the country rock. Rain or ice-bearing fallback ejecta could also be deposited on top of impact melt pools or suevite deposits [Segura *et al*., 2002], but that would not necessarily require that pits always form in the centers of their host craters, nor that they be consistently sized. Below, I describe an alternate model for bringing water into contact with impact melt.

Melt-Contact Model

I present an alternate hypothesis that -- unique among other explosive pit origin hypotheses -- predicts an explosion late enough in the impact process for central pits to be preserved and has a properly scaled analog. In my melt contact model, impact central uplifts bring water (as liquid, ice, or both) vertically up and into contact with near-surface impact melt to initiate late-stage steam explosions and form central pits (Fig. 30). Central uplift occurs late in the impact process from the end of the excavation stage through the modification stage, after most crater fill has settled [*e.g.,* Melosh, 1989]; thus, pit

76

formation concurrent with central uplift is consistent with the apparent lack of infilling of deep pits. As I describe in the next paragraph, my explosive central pit model is akin to an inverted maar volcano [*e.g.* White and Ross, 2011], except instead of magma rising up into contact with groundwater or permafrost, a water-bearing substrate is uplifted into contact with impact melt. Similarly-scaled events have been observed at monogenetic maar volcanoes with diameters of up to 8 km on the Seward Peninsula in Alaska [Begét *et al*., 1996], where the permafrost buffers the water-magma interaction to achieve high heat transfer efficiencies [Wohletz, 1986].

A)   B)
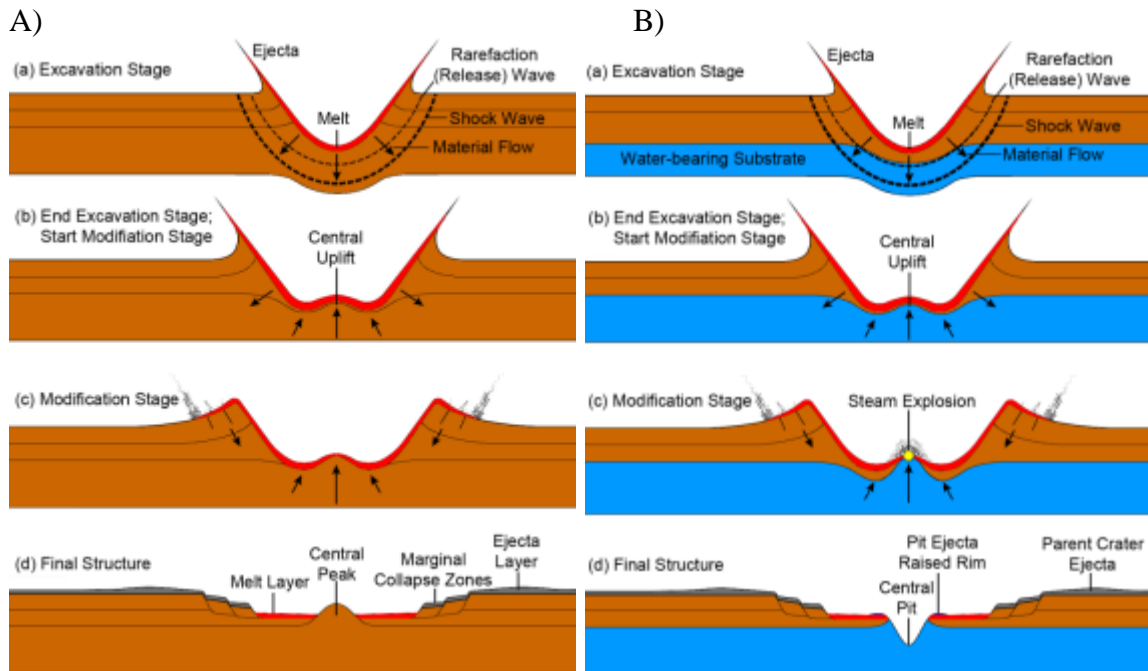
Fig. 30: Schematic cartoons illustrating steps in complex crater formation resulting in: A) a classical central peak [modified from French, 1998], and B) my proposed new "melt contact model" for Martian central pit crater formation.

As the central uplift rises, it brings deeply-sourced water-bearing rock from below the transient cavity up into contact with shallow crater fill deposits and impact melts. I would not expect significant vertical mixing of sub-transient cavity material outside the central uplift, so these large pits should always be in the centers of their host impact craters. As the water-bearing central uplift rises into contact with impact melt and other hot debris, the thermal energy from the melt may be transferred to the water, resulting in a steam explosion to eject material outward, raise rims, and deposit ejecta surrounding the pits (with average grain sizes decreasing with radial distance, as I found in this study). As material is ejected outwards, the walls may become unstable and slump hot debris and impact melt into the pit cavity. There, the new rush of melt and hot rocks may again react with uplifting water to recharge the system and iteratively trigger a series of explosions to

further deepen and widen the central pit. When central uplift slows, the vertical mixing of water decreases and the explosions will cease.

I explored the theoretical plausibility of whether enough thermal energy could have been available in a post-impact environment to initiate steam explosions capable of creating kilometer-scale central pits. I started with the empirical model shown below which predicts the mass ratio of melted (m_m) to displaced (m_d) impact target materials in a silicate target (Eq. 8) [O'Keefe and Ahrens, 1982; Melosh, 1989]:

$$m_m/m_d = 1.6 \times 10^{-7} \times (g \times D_i)^{0.83} \times v_i^{0.33} \quad , \quad (8)$$

where g is planetary gravity, D_i is host crater diameter and v_i is bolide velocity. I assigned the following values for my calculations: gravity $g = 3.711$ m/s^2 and mean Mars asteroidal bolide velocity $v_i = 10$ km/s [Ivanov et al., 2002]. I also assumed that any melt generated remained within the host crater. Finally, I modeled the host crater as a half-ellipsoid and applied the mass fraction to determine the volume and mass of melt produced (Eqs. 9,10):

$$V_m = (m_m/m_d) \times (2/3) \times \pi \times d_i \times (D_i/2)^2 \quad , \quad (9)$$

$$m_m = \rho_m/V_m \quad , \quad (10)$$

where V_m is the volume of melt, d_i is the depth of the host crater, and ρ_m is the density of the melt. I assumed a depth of complex craters (in km) of $d_i = 0.357D_i^{0.52}$ [Tornabene et

al., 2013]. Sato and Taniguchi [1997] found the following empirical equation to predict the energy required to form a crater via volcanic, nuclear, and chemical explosions, independent of origin. The equation can similarly be applied to central pits (Eq. 11):

$$E_c = 4.45 \times 10^6 \times D_p^{3.05} \ , \qquad (11)$$

where E_c is the energy of pit formation and D_p is the diameter of the pit, for which I assume a median pit-to-host crater diameter ratio of 0.16 [Barlow, 2010, 2011]. The total thermal energy transfer required to melt ice and boil water to steam can be calculated using specific and latent heats [*e.g.* Wohletz, 1986] (Eq. 12):

$$H_w = m_w \times L_f + m_w \times c_{lq} \times \Delta T_w + m_w \times L_v \ , \qquad (12)$$

where H_w is the energy transferred to the water, m_w is the mass of water, L_f is the latent heat of fusion, c_{lq} is the specific heat of liquid water, ΔT_w is the temperature change of liquid water, and L_v is the latent heat of vaporization. I assigned values for $L_f = 3.34 \times 10^5$ J/kg, $c_{lq} = 4.187 \times 10^3$ J/kg·K, and $L_v = 2.257 \times 10^6$ J/kg [Moran and Shapiro, 2008]. I assumed thermal equilibrium between water and chilled impact melt, a saturated water (liquid-vapor) system, and a 100 K temperature change. Evaluating Eq. 12, I found that an investment of 3.023×10^6 J is required to turn 1 kg of water from ice (273 K) to steam (373 K). Steam could potentially be heated to higher temperatures and/or further pressurized, which would result a smaller amount of (superheated) steam to satisfy the energy requirements for explosivity. The thermal energy of vaporization, specifically the

step of converting water to steam, can be transformed to kinetic energy that can form a

pit. The mass of steam required is calculated by dividing the pit formation energy from

Eq. 11 by the latent heat of vaporization. Dividing this result by the density of ice

provides the volume of ice required to form a central pit. As shown in Fig. 31, assuming a

half-ellipsoidal pit geometry with the pit depth (in km) $d_p = 0.276 D_p^{0.68}$ [Tornabene *et al*.,

2013], only a small amount of water (comprising 2-6% of a central pit's volume) would

need to be vaporized to form a central pit for the host crater diameters observed (5-125

km [Barlow, 2011]).
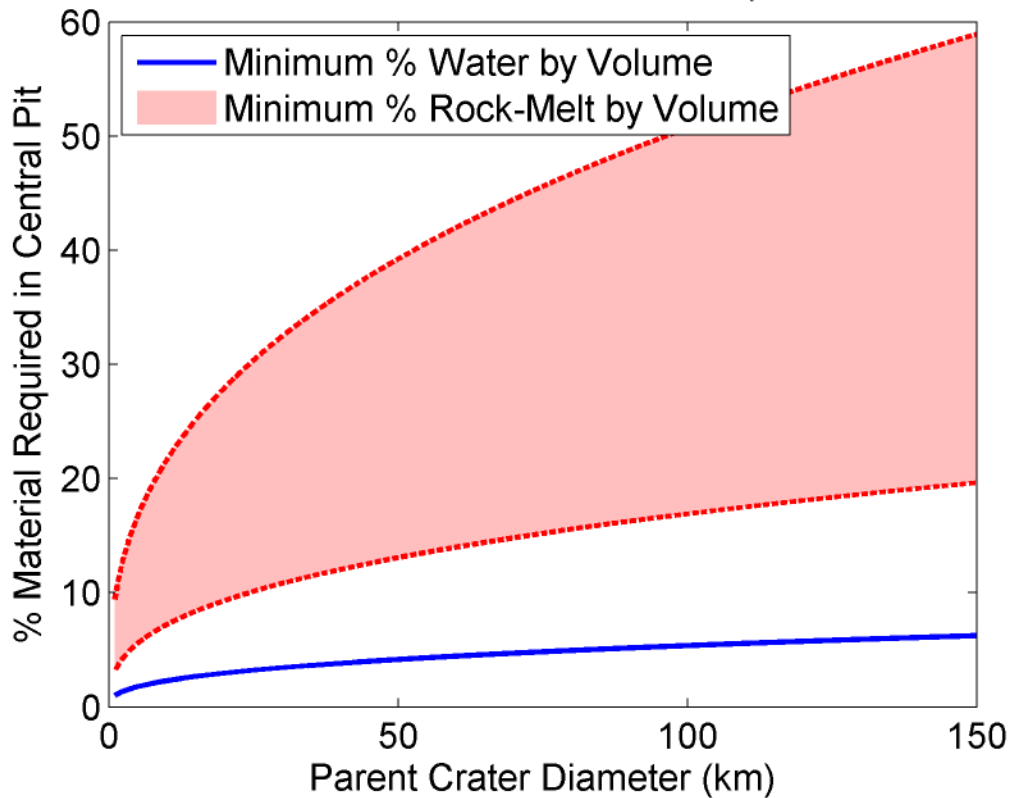
Fig. 31: Required amounts of water and impact melt for heat energy transfer to form a kilometer-scale (pit) crater shown as percent by volume with respect to the volume of a central pit crater. The range in impact melt volume represents uncertainty due to varying heat transfer efficiency between 0.1-0.3.

The amount of thermal energy available in impact melt may also be calculated using specific heats (Eq. 13):

$$E_m = m_m \times c_{pm} \times \Delta T_m = \rho_m \times V_m \times c_{pm} \times \Delta T_m \quad , \qquad (13)$$

where E_m is the energy required for cooling rock, c_{pm} is the specific heat of rock, ΔT_m is the temperature change of the rock. I assumed a basaltic melt composition and assign values of $\rho_m = 2900$ kg/m^3 [Judd and Shakoor, 1989]; $c_{pm} = 1000$ J/kg·K [Wohletz, 1986]; and change of temperature (from the basalt solidus to the STP boiling point of water) $\Delta T_m = 1473$ K $-$ 373 K $= 1100$ K [Wohletz, 1986]. It should be noted that impact melts can also be superheated, perhaps up to 1700°C (1973 K) [Zieg and Marsh, 2005], so these calculations may underestimate the thermal energy available by ~50%. Adiabatic heat transfer efficiency is typically ~0.1 or less due to poor mixing; however, it can reach an optimal efficiency of ~0.3 for water/melt ratios of 0.3-0.5 [Wohletz, 1986]. Such optimal efficiencies are believed to be present for maars in permafrost, as suggested by the largest, kilometer-scale terrestrial maars found in the Seward Peninsula, Alaska [Begét *et al*., 1996]. These calculations consider cases with both 0.1 (suboptimal) and 0.3 (optimal) efficiencies.

The mass of impact melt required to vaporize ice to steam can be calculated by setting the total heat transfer H_w from Eq. 12 equal to the product of the heat transfer efficiency and the impact melt thermal energy from Eq. 13. As shown in Fig. 31, the impact melt must comprise a volume greater than or equal to 6-18% of the central pit's volume for an optimal thermal efficiency of 0.3, or 17-55% of the central pit's volume

for a suboptimal thermal efficiency of 0.1. The total energy transfer required for

vaporizing ice (H_w) from Eq. 12 can also be compared to the total energy available from

impact melt by multiplying Eq. 13 with the value(s) for heat transfer efficiency (Figs.

32,33). Based on these calculations, sufficient thermal energy should be available via

impact melt to vaporize small amounts of ice that act explosively to form central pits

within kilometer-scale impact structures. However, not all Martian craters exhibit central

pits. Below, I discuss the material requirements that may inhibit the explosive formation

of some central pits on Mars.
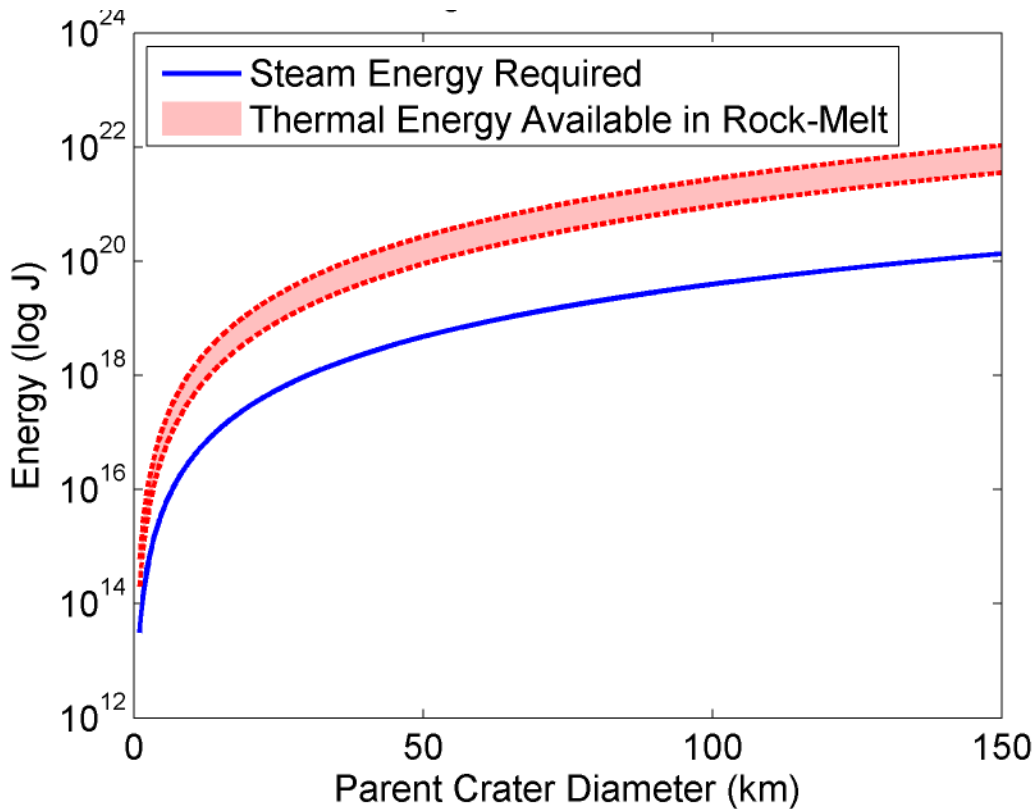
Fig. 32: Thermal energies of water required to convert ice to steam to provide the energy
for creating central pit craters (blue line) of differing diameter. Also shown is the
available thermal energy from impact melt, after applying thermal efficiency values of
0.1 (lower red curve) to 0.3 (upper red curve).
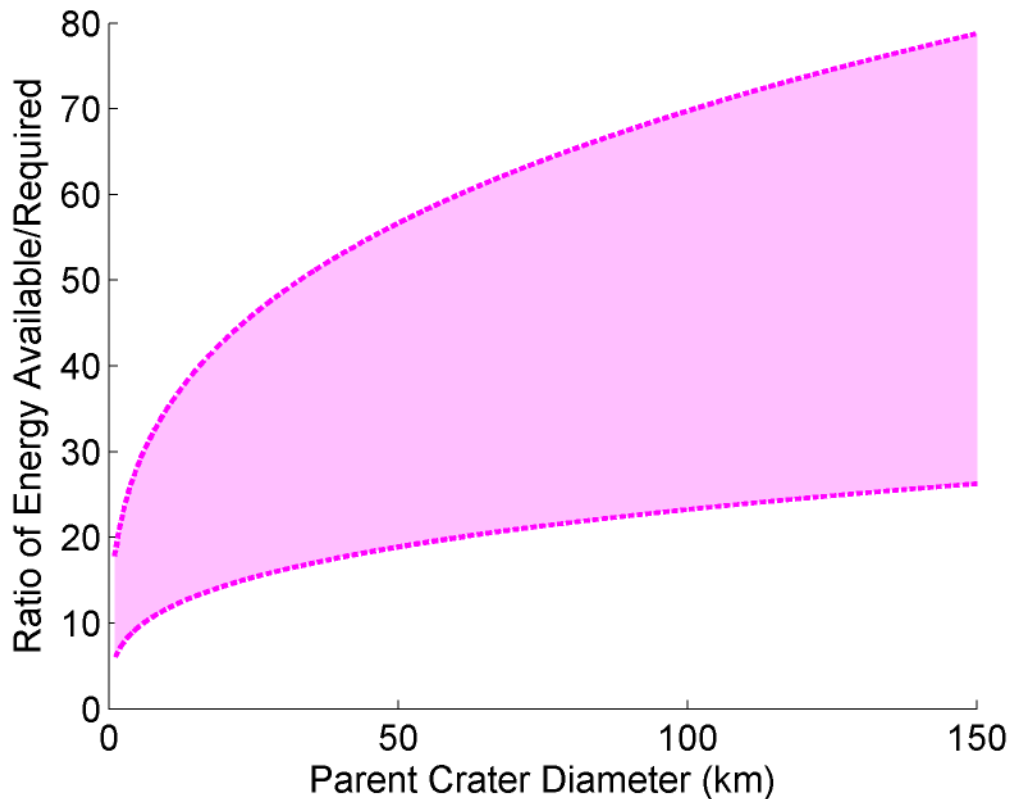
Fig. 33: Ratios of available / required thermal energy for vaporizing enough steam to explode and form a central pit, with respect to crater diameter. The range of in energy ratios reflects variations in heat transfer efficiency over a range of 0.1 (lower curve) to 0.3 (upper curve).

First, an appropriate volume of water must be available in the central uplift. If too little water (or too low a concentration) is present, there may not be sufficient steam to form a large pit. Even if water was initially present in the target rocks, large impacts (with crater diameters of several tens to hundreds of km) likely remove most subsurface volatiles early in the impact process such that not enough water is available to react with the impact melt to form a pit. Conversely, if the system has excess water, there may not be enough thermal energy in the impact melt to heat the excess water and still vaporize enough to sustain an explosion and make a pit.

Second, an appropriate volume of impact melt must be retained within the host impact crater. Smaller impact craters produce less melt proportionally and distribute that impact melt more sparsely, so small craters may not have enough consolidated impact melt even if enough water is present. Larger impact craters might also produce excess impact melt that could fill in any central pits that might form. Another interesting aspect of the melt contact model is that since these calculations show it only requires small amounts of water (perhaps as little as 2-6% by volume), it provides a possible explanation for the formation of the small number of central pits observed on Mercury [Schultz, 1988; Xiao and Komatsu, 2013] and the Moon [Croft, 1981; Schultz, 1976a, 1976b, 1988; Xiao *et al*., 2014], which should have insufficient water or other volatiles to form by drainage and collapse models [*e.g.* Croft, 1981]. Although I did not measure summit pit-related thermal inertias in this survey, summit pits would be expected to form as in my melt contact model when steam explosions start but become water- or impact melt-limited. In such a case, the explosive reaction fails before uplift has ceased and an incomplete pit is left superposed on a remnant central peak.

Based on my melt contact model, I propose the following testable predictions. First, a the ejecta deposit is expected to contain abundant fractured and fragmented glassy impact melt, similar to the Onaping Formation at Sudbury [Grieve *et al*., 2010]. This layer of glassy deposits should overlay more coherent impact melt deposits. Second, lithic clasts and mineral assemblages found stratigraphically below the transient crater should be found on the floor of the host crater, with the greatest abundance proximal to the rim. Third, the stratigraphic sequence of rocks around central pits should be

overturned. Finally, *in situ* measurements of material around the pit should show

decreasing average grain sizes with radial distance from central pits.

CONCLUSIONS

This dissertation has utilized multiple datasets from visible and thermal images to topographic rasters and crosscut planetary bodies. Through careful observation, mapping, interpretation, and finally modeling, I have characterized morphology, determined distributions, constrained ages and geometries, and proposed mechanisms for landscape evolution. The products are reconstructions the evolution of both lunar tectonic landforms and Martian central pit craters to provide new insights to their respective fundamental processes.

On Mars, the presence of raised rims and blocky material surrounding Martian central pits are suggestive of ejecta from an explosive pit origin. A strong majority of central pits in my global survey have material with radially decreasing thermal inertias around them, particularly for central pits craters with larger diameters and regions relatively free of sand and dust. The population of central pit craters as a whole has a statistically significant ($P<0.01$) decrease in thermal inertia radially outwards from pit rims. I interpret these findings as a typical decrease in average grain size with increasing distance away from central pits. As expected, dust masks the diurnal thermal signature around many central pits. This effect is amplified in smaller pits due to their less voluminous and finer-grained ejecta that are more easily buried or eroded.

Previously proposed models do not satisfactorily explain all observed characteristics of central pits. I have therefore proposed a new "melt contact model" to explain the observed morphologies (i.e., geometries, raised rims) and thermal properties (radially decreasing thermal inertias/average grain size) of Martian central pit craters. Thermal calculations show that only 2-6% water by volume is required to create a

87

phreatomagmatic explosion and form central pits. The absence of central pits in many impact craters may be due to excess or insufficient volumes of impact melt and water to propagate a steam reaction, as well as variable degrees of mixing. An explosive origin model is advantageous over drainage and collapse models in explaining the small number of central pits on Mercury and the Moon using only minor amounts of volatiles in localized pre-impact subsurfaces. My melt contact model is also advantageous over other explosive models in forming the pit late enough in the impact process to be preserved. Drainage and collapse may still be a viable method for pit formation on icy satellites, but an explosive origin appears to be the more viable mechanism on Mars (and other rocky planets) for forming central pit craters.

On the Moon, Mare Frigoris is host to a complex assortment of tectonic landforms that imply a complex history of deformation spanning the last ~3.8 billion years. Mare basalts filled most of the eastern part of the basin from ~3.8 to 3.6 billion years ago [Hiesinger *et al.*, 2010], leading to isostatic flexure and subsidence. The center of the eastern basin underwent compression forming the observed polygonal pattern of wrinkle ridges, while the edges of the eastern basin underwent extension forming large linear to arcuate graben. Mare basalts were mostly emplaced in the western basin from ~3.6 to 3.4 billion years ago with some as late as ~2.6 billion years ago [Hiesinger *et al.*, 2010] and were shortly followed by the formation of a parallel set of wrinkle ridges. These ridges do not support mascon induced flexure nor a tectonic control associated with Mare Imbrium. Instead, they suggest a regional, non-isostatic stress field of similar large scale to the previously proposed Procellarum basin, but not necessarily due to impact [Whitaker, 1981] or rifting [Andrews-Hanna *et al.*, 2014]. Flexural induced subsidence and resulting

88

tectonic activity decayed and ceased after ~3.4 billion years ago in most places and everywhere in Mare Frigoris after ~2.6 billion years ago, while bombardment of meteoroids progressively degraded these older landforms. Small graben associated with these older landforms may have formed while they were active, but any that might have existed would have been infilled by impact gardening over millions to billions of years.

I also performed fault dislocation modeling using LROC NAC DTMs for six lunar lobate scarps to determine their fault geometries. The six scarp models are consistent with deformation from thrust faulting at typical dip angles of 35-40° and maximum faulting depths from a few hundred meters to around a kilometer. Although a subset of the global population of lobate scarps was used in this study, their morphology is characteristic of other scarps [Banks *et al*., 2012]. Since fault geometry is the principal variable in controlling lobate scarp topography, I expect other scarps to have similar fault geometries. My model fault dips are steeper and have shallower maximum depths than Apollo-era estimates, but are comparable to other fault dislocation models created for lobate scarps on asteroid 433 Eros [Watters *et al*., 2011] and larger scarps on Mercury [Watters and Schultz, 2002; Watters et al., 2002] and Mars [Schultz and Watters, 2001]. Based on modeled depths of faulting, I estimate between 3.5-18.6 MPa of differential stress within a kilometer of the lunar surface at the time of faulting. This low level of compressional stress needed to initiate shallow-rooted thrust faults on the Moon is consistent with thermal history models that predict a relatively small amount of late-stage stress from global radial contraction.

The most exciting finding of this dissertation is probably the abundance of recent and ongoing tectonic activity. In the late Eratosthenian to Copernican (~1 billion years

ago), late-stage stresses from global radial contraction formed new faults and perhaps reactivated some old ones. These faults formed the lobate scarps in the highlands, including the long cluster just east of Mare Frigoris. New wrinkle ridges formed in the mare and appear in LROC images as a morphologically crisp population contrasting with the older, more degraded ridges. In some cases, new faults crossed the mare-highland boundary forming wrinkle ridge – lobate scarp transitions. Small graben also formed recently as a secondary effect of wrinkle ridge and lobate scarp growth, and at least some have survived to today. Although direct changes from surface tectonic deformation have not yet been observed in the modern day, the young ages of many tectonic landforms identified globally as well as in Mare Frigoris, along with the shallow moonquakes recorded by Apollo with seismic moments consistent with those predicted for the population of lobate scarps, suggest that tectonic activity is likely still occurring on the lunar surface today.

Geologic activity at the surface of the Moon and Mars are not only intriguing in their own right, but they also provide greater insight to the geophysics and other processes that occur here on Earth but are not always well expressed on our planet's surface. Through continued work beyond this dissertation, I endeavor to continue investigating near-surface structural evolution on planetary surfaces in endmember environments to better understand how landforms evolve both here and elsewhere in the universe.

REFERENCES

Alzate, N., Barlow, N.G., 2011. Central pit craters on Ganymede. Icarus 211, 1274-1283.

Anderson, J.A., Sides, S.C., Soltesz, D.L., Sucharski, T.L, Becker, K.J., 2004. Modernization of the Integrated Software for Imagers and Spectrometers. Lunar Planet. Sci. Conf. 35, #2039.

Andrews-Hanna, J.C., Besserer, J., Head, J.W., Howett, C.J.A., Kiefer, W.S., Lucey, P.J., McGovern, P.J., Melosh, H.J., Neumann, G.A., Phillips, R.J., Schenk, P.M., Smith, D.E., Solomon, S.C., Zuber, M.T., 2014. Structure and evolution of the lunar Procellarum region as revealed by GRAIL gravity data. Nature 514, 68-71.

Arvidson, R., Drozd, R.J., Hohenberg, C.M., Morgan, C.J., Poupeau, G., 1975. Horizontal transport of the regolith, modification of features, and erosion rates on the lunar surface. Moon 13, 67-79.

Baloga, S.M., Fagents, S.A., Mouginis-Mark, P.J., 2005. Emplacement of Martian Rampart Crater Deposits. J. Geophys. Res. 110, E10001. doi:10.1029/2004JE002338.

Banks, M.E., Watters, T.R., Robinson, M.S., Tornabene, L.L., Tran, T., Ojha, L., Williams, N.R., 2012. Morphometric analysis of small-scale lobate scarps on the Moon using data from the Lunar Reconnaissance Orbiter. J. Geophys. Res. 117, doi:10.1029/2011JE003907.

Barlow, N. G., Bradley, T. L., 1990. Martian impact craters: Correlations of ejecta and interior morphologies with diameter, latitude, and terrain. Icarus, 87(1), 156-179.

Barlow, N.G., 2006. Impact Craters in the Northern Hemisphere of Mars: Layered Ejecta and Central Pit Characteristics. Met. & Planet. Sci. 41, 1425-1436.

Barlow, N.G., 2010. Central pit craters: Observations from Mars and Ganymede and implications for formation models. GSA Special Papers 465, 15-27.

Barlow, N.G., 2011. Constraints on the Proposed Formation Models for Martian Central Pit Craters. Lunar Planet. Sci. 42. Abstract #1149.

Barlow, N.G., Boyce, J.M., Costard, F.M., Craddock, R.A., Garvin, J.B., Sakimoto, S.E.H., Kuzmin, R.O., Roddy, D.J., 2000. Standardizing the Nomenclature of Martian Impact Crater Ejecta Morphologies. J. Geophys. Res. 105, E11, 26733-26738.

Begét, J.E., Hopkins, D.M., Charron, S.D., 1996. The Largest Known Maars on Earth, Seward Peninsula, Northwest Alaska. Arctic 49, 1, 62-69.

Bell, J.F., III, Malin, M.C., Caplinger, M.A., Fahle, J., Wolff, M.J., Cantor, B.A., James, P.B., Ghaemi, T., Posiolova, L.V., Ravine, M.A., Supulver, K.D., Calvin, W.M., Clancy, R.T., Edgett, K.S., Edwards, L.J., Haberle, R.M., Hale, A., Lee, S.W., Rice, M.S.,

Thomas, P.C., Williams, R.M.E., 2013. Calibration and Performance of the Mars Reconnaissance Orbiter Context Camera (CTX). Mars 8, 1-14. doi:10.1555/mars.2013.0001.

Berens, P., 2009. CircStat: A Matlab Toolbox for Circular Statistics. Journal of Statistical Software 31, 10.

Bieniawski, Z.T., 1984. Rock Mechanics Design in Mining and Tunneling, A.A. Balkema, Rotterdam, 272.

Binder, A.B., 1982. Post-Imbrian Global Lunar Tectonism: Evidence for an Initially Totally Molten Moon, Moon and Planets 26, 117-133.

Binder, A.B., 1986. The Initial Thermal State of the Moon, Origin of the Moon, Lunar and Planetary Institute, 425-433.

Binder, A.B. and H.-C. Gunga, 1985. Young Thrust-Fault Scarps in the Highlands: Evidence for an Initially Totally Molten Moon, Icarus 63, 421-441.

Binder, A.B. and M.A. Lange, 1980. On the Thermal History of the Moon of Fission Origin, Moon 17, 29-45.

Boyce, J.M., Wilson, L., Mouginis-Mark, P.J., Hamilton, C.W., Tornabene, L.L., 2012. Origin of small pits in martian impact craters. Icarus, 221(1), 262-275.

Boynton, W.V., Taylor, G.J., Evans, L.G., Reedy, R.C., Starr, R., Janes, D.M., Kerry, K.E., Drake, D.M., Kim, K.J., Williams, R.M.S., Crombie, M.K., Dohm, J.M., Baker, V., Metzger, A.E., Karunatillake, S., Keller, J.M., Newsom, H.E., Arnold, J.R., Bruckner, J., Englert, P.A.J., Gasnault, O., Sprague, A.L., Mitrofanov, I., Squyres, S.W., Trombka, J.I., d'Uston, L., Wanke, H., Hamara, D.K., 2007. Concentration of H, Si, Cl, K, Fe, and Th in the low- and mid-latitude regions of Mars. J. Geophys. Res. 112, E12S99. doi:10.1029/2007JE002887.

Bray, V.J., 2009. Impact crater formation on the icy Galilean satellites. Doctoral dissertation, Imperial College London.

Bray, V.J., Schenk, P.M., Melosh, H.J., Morgan, J.V., Collins, G.S., 2012. Ganymede crater dimensions – Implications for central peak and central pit formation and development. Icarus 217, 115-129.

Buhl, E., Sommer, F., Poelchau, M.H., Dresen, G., Kenkmann, T., 2014. Ejecta from experimental impact craters: Particle size distribution and fragmentation energy. Icarus 237, 131-142.

Bürgmann R., D. D. Pollard, and S. J. Martel, 1992. Slip Distributions on Faults: Effects of Stress Gradients, Inelastic Deformation, Heterogeneous Hostrock Stiffness, and Fault Interaction, J. Struct. Geol., 16, 1675–1690.

Byerlee, J. D., 1968. Brittle-Ductile Transition in Rocks, JGR 73, 4741-4750.

Byerlee, J. D., 1978. Friction of Rocks, Pure and Applied Geophys. 116, 615-626.

Cadogan, P.H., 1974. Oldest and largest lunar basin? Nature 250, 315-316.

Cadogan, P.H., 1975. The gargantuan basin – some implications. Lunar Planet. Sci. Conf. 6, 123-124.

Carr, M.H., Crumpler, L.S., Cutts, J.A., Greeley, R., Guest, J.E., Masursky, H., 1977. Martian Impact Craters and Emplacement of Ejecta by Surface Flow. J. Geophys. Res. 82, 28, 4055-4065.

Caudill, C. M., Tornabene, L. L., McEwen, A. S., Byrne, S., Ojha, L., & Mattson, S., 2012. Layered MegaBlocks in the central uplifts of impact craters. Icarus, 221(2), 710-720.

Christensen, P.R., 1986. The Spatial Distribution of Rocks on Mars. Icarus 68, 217-238.

Christensen, P.R., Bandfield, J.L., Hamilton, V.E., Ruff, S.W., Kieffer, H.H., Titus, T.N., Malin, M.C., Morris, R.V., Lane, M.D., Clark, R.L., Jakosky, B.M., Mellon, M.T., Pearl, J.C., Conrath, B.J., Smith, M.D., Clancy, R.T., Kuzmin, R.O., Roush, T., Mehall, G.L., Gorelick, N., Bender, K., Murray, K., Dason, S., Greene, E., Silverman, S., Greenfield, M., 2001. Mars Global Surveyor Thermal Emission Spectrometer experiment: Investigation description and surface science results. J. Geophys. Res. 106, E10, 23823–23871.

Christensen, P.R., Engle, E., Anwar, S., Dickenshied, S., Noss, D., Gorelick, N., Weiss-Malik, M., 2009. JMARS – A Planetary GIS. AGU Fall Meeting, Abs. # #IN22A-06.

Christensen, P.R., Jakosky, B.M., Kieffer, H.H., Malin, M.C., McSween, H.Y., Jr., Nealson, K., Mehall, G.L., Silverman, S.H., Ferry, S., Caplinger, M., Ravine, M., 2004. The Thermal Emission Imaging System (THEMIS) for the Mars 2001 Odyssey Mission. Space Sci. Rev. 110, 85-130.

Clifford, S.M., Hillel, D., 1983. The Stability of Ground ice in the Equatorial Region of Mars. J. Geophys. Res. 88, B3, 2456-2474.

Croft, S.K., 1981. On the Origin of Pit Craters. Proc. Lunar Planet. Sci. Conf. 12, 196-198.

Cushing, G.E., Titus, T.N., Wynne, J.J., Christensen, P.R., 2007. THEMIS observes possible cave skylights on Mars. Geophys. Res. Let. 34, L17201. doi:10.1029/2007GL030709.

DeVenecia, K., A. S. Walker, B. Zhang, 2007. New approaches to generating and processing high resolution elevation data with imagery, Photogrammetric Week 2007, edited by D. Fritsch, pp. 297–308, Wichmann, Heidelberg.

Edwards, C.S., Bandfield, J.L., Christensen, P.R., Fergason, R.L., 2009. Global Distribution of Bedrock Exposures on Mars using THEMIS High-resolution Thermal Inertia. J. Geophys. Res. 114, E11001. doi:10.1029/2009JE003363.

Edwards, C.S., Nowicki, K.J., Christensen, P.R., Hill, J., Gorelick, N., Murray, K., 2011. Mosaicking of global planetary image datasets: 1. Techniques and data processing for Thermal Emission Imaging System (THEMIS) multi-spectral data. J. Geophys. Res. 116, E10008. doi:10.1029/2010JE003755.

Elder, C.M., Bray, V.J., Melosh, H.J., 2012. Theoretical Plausibility of Central Pit Crater Formation Via Melt Drainage. Icarus 221, 831-843.

Fergason, R.L., Christensen, P.R., Kieffer, H.H., 2006. High Resolution Thermal Inertia Derived from THEMIS: Thermal Model and Applications. J. Geophys. Res. 111, E12004. doi:10.1029/2006JE002735.

Freed, A.M., Melosh, H.J., Solomon, S.C., 2001. Tectonics of mascon loading: Resolution of the strike-slip faulting paradox. J. Geophys. Res. Planets 106, 20603-20620.

French R.A., Bina, C.R., Robinson, M.S., Watters, T.R., 2015. Small-scale lunar graben: Distribution, dimensions, and formation processes. Icarus 252, 95-106.

French, B.M., 1998. Traces of Catastrophe. LPI Contribution No. 954, Lunar and Planet. Inst., Houston, Texas.

Garner, K. M. L., Barlow, N. G., 2012. Distribution of rimmed, partially rimmed, and non-rimmed central floor pits on Mars. LPSC 43, Abstract #1256.

Garvin, J. B., Sakimoto, S. E., Frawley, J. J., 2000. Craters on Mars: Global Geometric Properties from Gridded MOLA topography. Mars 5, Abstract #3277.

Garvin, J. B., Sakimoto, S. E., Frawley, J. J., Schnetzler, C. 2000. North polar region craterforms on Mars: Geometric characteristics from the Mars Orbiter Laser Altimeter. Icarus, 144(2), 329-352.

Gault, D.E., Greeley, R., 1978. Exploratory Experiments of Impact Craters Formed in Viscous-Liquid Targets: Analogs for Martian Rampart Craters?. Icarus 34, 486-495.

Gault, D.E., Shoemaker, E.M., Moore, H.J., 1963. Spray Ejected from the Lunar Surface by Meteoroid Impact. NASA Technical Note D-1767.

Gilbert, G.K., 1893. The Moon's face, a study of the origin of its features. Philos. Soc. Washington Bull. 12, 241–292.

Golombek, M. P. and R. J. Phillips, 2010. Mars Tectonics, Planetary Tectonics, Cambridge University Press, edited by T. R. Watters and R. A. Schutlz, pp. 183-232.

Golombek, M.P., 1979. Structural analysis of lunar grabens and the shallow crustal structure of the Moon. J. Geophys. Res. 84, 4657–4666.

Golombek, M.P., Anderson, F.S., Zuber, M.T. 2001. Martian wrinkle ridge topography: Evidence for subsurface faults from MOLA. J. Geophys. Res., 106, 23811–23821.

Golombek, M.P., Plescia, J.B., Franklin, B.J., 1991. Faulting and folding in the formation of planetary wrinkle ridges. Proc. Lunar Planet Sci. Conf. 21, 679−693.

Greeley, R., Fink, J.H., Gault, D.E., Guest, J.E., 1982. Experimental simulation of impact cratering on icy satellites. In D. Morrison (Ed.), Satellites of Jupiter. University of Arizona Press, Tucson, Arizona. pp. 340-378.

Grieve, R.A.F., Ames, D.E., Morgan, J.V., Artemieva, N., 2010. The evolution of the Onaping Formation at the Sudbury impact structure. Met. Planet. Sci. 45, 5, 759-782.

Head, J. W., Mustard, J.F., Kreslavsky, M.A., Milliken, R.E., Marchant, D.R., 2003. Recent Ice Ages on Mars. Nature 426, 797-802.

Hiesinger, H., Head, J.W., Wolf, U., Jaumann, R., Neukum, G., 2003. Ages and stratigraphy of mare basalts in Oceanus Procellarum, Mare Nubium, Mare Cognitum, and Mare Insularum. J. Geophys. Res. 108, E75065.

Hiesinger, H., Head, J.W., Wolf, U., Jaumann, R.,Neukum, G., 2010. Ages and stratigraphy of the lunar mare basalts in Mare Frigoris and other nearside maria based on crater size-frequency distribution measurements. J. Geophys. Res. 115, doi:10.1029/2009JE003380.

Hodges, C.A., 1978. Central Pit Craters on Mars. Proc. Lunar Planet. Sci. Conf. 9, 521-522.

Hodges, C.A., Shew, N.B., Clow, G., 1980. Distribution of Central Pit Craters on Mars. Proc. Lunar Planet. Sci. Conf. 11, 450-452.

Hoek, E., and M. S. Diederichs, 2006. Empirical Estimation of Rock Mass Modulus, Int. J. Rock Mech. Min. Sci., 43, 203–215, doi:10.1016/j.ijrmms.2005.06.005.

Hoek, E., C. Carranza-Torres, B. Corkum, 2002. Hoek-Brown Failure Criterion, in Proceedings 5th North American Rock Mechanics Symposium, edited by R. P. Young, pp. 267–273, Toronto, Ont., Canada.

Hoek, E., D. Wood, S. Shah, 1992. A Modified Hoek-Brown Failure Criterion for Jointed Rock Masses, Proc. rock characterization, symp. Int. Soc. Rock Mech., 209-214

Howard, K.A., Muehlberger, W.R., 1973. Lunar thrust faults in the Taurus−Littrow region. Apollo 17 Prel. Sci. Rep., NASA Spec. Publ. SP-330, 31-32 – 31-25.

Hustrulid, W. A. and R. L. Bullock, 2001) Underground Mining Methods - Engineering Fundamentals and International Case Studies, Society for Mining, Metallurgy, and Exploration, p. 305.

Ivanov, B. A., Neukum, G., Bottke, W. F., & Hartmann, W. K., 2002. The comparison of size-frequency distributions of impact craters and asteroids and the planetary cratering rate. Asteroids III, 1, 89-101.

Judd, W. R., Shakoor, A., 1989. Density in Physical Properties of Rocks and Minerals (ed. C. Y. Ho et al.), Philadelphia, PA: Taylor and Francis, pp. 409–502.

Kirk, R.L., Stevenson, D.J., 1989. The competition between thermal contraction and differentiation in the stress history of the Moon. J. Geophys. Res. B9, 12133-12144.

Lemoine, F.G., Goossens, S., Sabaka, T.J., Nicholas, J.B., Mazarico, E., Rowlands, D.D., Loomis, B.D., Chinn, D.S., Neumann, G.A., Smith, D.E., Zuber, M.T., 2014. GRGM900C: A degree 900 lunar gravity model from GRAIL primary and extended mission data. Geophys. Res. Let. 41, 10, 3382-3389.

Lin, J. and R.S. Stein, 2004. Stress triggering in thrust and subduction earthquakes, and stress interaction between the southern San Andreas and nearby thrust and strike-slip faults, JGR 109, B02303, doi:10.1029/2003JB002607.

Lucchitta, B. K. and J. A. Watkins, 1978. Large Grabens and Lunar Tectonism, Proc. LPSC 9, 666-668.

Lucchitta, B.K., 1976. Mare ridges and related highland scarps – Result of vertical tectonism? Proc. Lunar Planet. Sci. Conf. 7, 2761-2782.

Malin, M.C., Bell, J.F., III, Cantor, B.A., Caplinger, M.A., Calvin, W.M., Clancy, R.T., Edgett, K.S., Edwards, L., Haberle, R.M., James, P.B., Lee, S.W., Ravine, M.A., Thomas, P.C., Wolff, M.J., 2007. Context Camera Investigation on board the Mars Reconnaissance Orbiter. J. Geophys. Res. 112, E05S04. doi:10.1029/2006JE002808.

Mangold, N., P. Allemand, P. G. Thomas, G. Vidal, 2000. Chronology of Compressional Deformation on Mars: Evidence for a Single and Global Origin, Planetary And Space Science 48, 1201-1211.

McEwen, A.S., Eliason, E.M., Bergstrom, J.W., Bridges, N.T., Hansen, C.J., Delamere, W.A., Grant, J.A., Gulick, V.C., Herkenhoff, K.E., Keszthelyi, L., Kirk, R.L., Mellon, M.T., Squyres, S.W., Thomas, N., Weitz, C.M., 2007. Mars Reconnaissance Orbiter's

High Resolution Imaging Science Experiment (HiRISE). J. Geophys. Res. 112, E05S02. doi:10.1029/2005JE002605.

McEwen, A.S., Preblich, B.S., Turtle, E.P., Artemieva, N.A., Golombek, M.P., Hurst, M., Kirk, R.L., Burr, D.M., Christensen, P.R., 2005. The rayed crater Zunil and interpretations of small impact craters on Mars. Icarus 176, 351-381.

McGill, G.E., 1971. Attitude of fractures bounding straight and arcuate lunar rilles. Icarus 14, 53–58.

Mellon, M.T., Jakosky, B.M., Postawko, S.E., 1997. The Persistence of Equatorial Ground Ice on Mars. J. Geophys. Res. 102, E8, 19357-19369.

Melosh, H. J., 1980) Tectonic patterns on a tidally distorted planet, Icarus 43, 334-337.

Melosh, H.J., 1978. The tectonics of mascon loading. Proc. Lunar Planet. Sci. Conf. 9, 3513-3525.

Melosh, H.J., 1989. Impact Cratering: A Geologic Process. Oxford Monographs on Geology and Geophysics #11, Oxford University Press, New York.

Moore, H.J., Boyce, J.M., Hahn, D.A., 1980. Small impact craters in the lunar regolith – their morphologies, relative ages, and rates of formation. Moon & Planets 23, 231-252.

Moran, M. J., Shapiro, H. N., Boettner, D. D., & Bailey, M., 2010. Fundamentals of Engineering Thermodynamics. John Wiley & Sons.

Mueller, K., Golombek, M.P., 2004. Compressional structures on Mars. Annu. Rev. Earth Planet. Sci., doi:10.1146/annurev.earth.1132.101802.120553.

Nahm, A. L. and R. A. Schultz, 2011. Magnitude of Global Contraction on Mars from Analysis of Surface Faults: Implications for Martian Thermal History, Icarus 211, 389-400.

Nakamura, Y., Latham, G.V., Dorman, H.J., 1982. Apollo Lunar Seismic Experiment – Final Summary. J. Geophys. Res. 87, Supp., A117-A123.

Nakamura, Y., Latham, G.V., Dorman, H.J., Ibrahim, A.-B.K., Koyama, J., Horvath, P., 1979. Shallow moonquakes: Depth, distribution and implications as to the present state of the lunar interior. Proc. Lunar Sci. Conf. 10, 2299–2309.

Nelson, D.M., Koeber, S.D., Daud, K., Robinson, M.S., Watters, T.R., Banks, M.E., Williams, N.R., 2014. Mapping lunar maria extents and lobate scarps using LROC image products. Lunar Planet. Sci. Conf. 45, 2861.

O'Keefe, J.D., Ahrens, T.J., 1985. Impact and Explosion Crater Ejecta, Fragment Size, and Velocity. Icarus 62, 328-338.

Oberst, J., 1987. Unusually high stress drops associated with shallow moonquakes. J. Geophys. Res. 92, B2, 1397-1405.

Okada, Y., 1992. Internal Deformation Due to Shear and Tensile Faults in a Half-Space, Bulletin of the Seismological Society Of America 82, 1018-1040.

O'Keefe, J. D., & Ahrens, T. J., 1982. Cometary and meteorite swarm impact on planetary surfaces. J. Geophys. Res. 87(B8), 6668-6680.

Okubo, C.H., Martel, S.J., 1998. Pit crater formation on Kilauea volcano, Hawaii. J. Volc. Geothermal Res. 86, 1-18.

Passey, Q.R., Shoemaker, E.M., 1982. Craters and basins on Ganymede and Callisto: Morphological indicators of crustal evolution. In: Morrison, D. (Ed.), Satellites of Jupiter. Univ. of Arizona Press, Tucson, Arizona. pp. 379-434.

Pierazzo E., Artemieva, N.A., Ivanov, B.A., 2005. Starting conditions for hydrothermal systems underneath Martian craters: Hydrocode modeling. In Large meteorite impacts III, eds: Kenkmann T., Hörz F., Deutsch A.. Boulder, CO: Geo. Soc. of America. pp. 443–457.

Plescia, J.B., Golombek, M.P., 1986. Origin of planetary wrinkle ridges based on the study of terrestrial analogs. Geol. Soc. Am. Bull. 97, 1289–1299.

Pritchard, M.E., Stevenson, D.J., 2000. Thermal aspects of a lunar origin by giant impact. In Canup, R., Righter, K. (Eds.), Origin of the Earth and Moon. Tucson, AZ: University of Arizona Press, 179–196.

Robinson, M.S., Ashley, J.W., Boyd, A.K., Wagner, R.V., Speyerer, E.J., Hawke, B.R., Hiesinger, H., van der Bogert, C.H., 2012. Confirmation of sublunarean voids and thin layering in mare deposits. Planet. Space Sci. 69, 18-27.

Robinson, M.S., Brylow, S.M., Tschimmel, M., Humm, D., Lawrence, S.J., Thomas, P.C., Denevi, B.W., Bowman-Cisneros, E., Zerr, J., Ravine, M.A., Caplinger, M.A., Ghaemi, F.T., Schaffner, J.A., Malin, M.C., Mahanti, P., Bartels, A., Anderson, J., Tran, T.N., Eliason, E.M., McEwen, A.S., Turtle, E., Jolliff, B.L., Hiesinger, H., 2010. Lunar Reconnaissance Orbiter Camera (LROC) instrument overview. Space Sci. Rev. 150, 81–124.

Salvati, R., Sasowsky, I.D., 2002. Development of collapse sinkholes in areas of groundwater discharge. J. Hydrology 264, 1-11.

Sato, H., Taniguchi, H., 1997. Relationship Between Crater Size and Eject Volume of Recent Magmatic and Phreato-magmatic Eruptions: Implications for Energy Partitioning. Geophys. Res. Let. 24, 3, 205-208.

Savage, J.C., Simpson, R.W., 1997. Surface strain accumulation and the seismic moment tensor. Bull. of the Seis. Soc. of America 87, 5, 1345-1353.

Schmitt, H.H., Cernan, E.A., 1973. Geological investigation of the Apollo 17 landing site, Apollo 17 Preliminary Sci. Report. NASA Spec. Publ. SP-330, 5-1—5-21.

Scholten, F., J. Oberst, K.-D. Matz, T. Roatsch, M. Wählisch, M. S. Robinson, and the LROC Team, 2011. GLD100 – The Global Lunar 100 Meter Raster DTM from LROC WAC Stereo Models, LPSC 42, 2046.

Scholten, F., Oberst, J., Matz, K.-D., Roatsch, T., Wahlish, M., Speyerer, E.J., Robinson, M.S., 2012. GLD100: The near-global lunar 100 m raster DTM from LROC WAC stereo image data. J. Geophys. Res. Planets 117, doi:10.1029/2011JE003926.

Schultz, P.H., 1976a. Floor-fractured lunar craters. Moon 15, 241-273.

Schultz, P.H., 1976b. Moon Morphology. University of Texas Press, Austin, Texas.

Schultz, P.H., 1988. Cratering on Mercury: A Relook. In: Villas, F., Chapman, C.R., Matthews, M.S. (Eds.), Mercury, University of Arizona Press, Tucson, Arizona, pp. 274-335.

Schultz, R. A. and T. R. Watters, 2001. Forward Mechanical Modeling of the Amenthes Rupes Thrust Fault on Mars, Geophys. Res. Let. 28, 4659-4662.

Schultz, R.A., 2000. Localizaton of bedding-plane slip and backthrust faults above blind thrust faults: Keys to wrinkle ridge structure. J. Geophys. Res. 105, 12 035–12 052.

Scott, D.H., 1973. Small structures of the Taurus-Littrow region, Apollo 17 Preliminary Sci. Report. NASA Spec. Publ. SP-330, 31-25—31-29.

Segura, T.L., Toon, O.B., Colaprete, A., & Zahnle, K., 2002. Environmental effects of large impacts on Mars. Science, 298(5600), 1977-1980.

Senft, L.E., Stewart, S.T., 2011. Modeling the morphological diversity of impact craters on icy satellites. Icarus 214, 67-81.

Sharpton, V. L., and J. W. Head, 1988. Lunar Mare Ridges: Analysis of Ridge-Crater Intersections and Implications for the Tectonic Origin of Mare Ridges, LPSC 18, 307-317.

Sharpton, V.L., 2014. Outcrops on lunar crater rims: Implications for rim construction mechanisms, ejecta volumes and excavation depths. J. Geophys. Res. Planets 119, 154-168.

Smith, B.A., Soderblom, L.A., Beebe, R., Boyce, J., Briggs, G., Carr, M., Collins, S.A., Cook, A.F., II, Danielson, G.E., Davies, M.E., Hunt, G.E., Ingersoll, A., Johnson, T.V.,

Masursky, H., McCauley, J., Morison, D., Owen, T., Sagan, C., Shoemaker, E.M., Strom, R., Suomi, V., Veverka, J., 1979. The Galilean Satellites and Jupiter: Voyager 2 Imaging Science Results. Science 206, 927-950.

Smith, D.E., Zuber, M.T., Frey, H.V., Garvin, J.B., Head, J.W., Muhleman, D.O., Pettengill, G.H., Phillips, R.J., Solomon, S.C., Zwally, H.J., Banerdt, W.B., Duxbury, T.C., Golombek, M.P., Lemoine, F.G., Newmann, G.A., Rowlands, D.D., Aharonson, O., Ford, P.G., Ivanov, A.B., Johnson, C.L., McGovern, P.J., Abshire, J.B., Afzal, R.S., Sun, X. 2001. Mars Orbiter Laser Altimeter: Experiment Summary After the First Year of Global Mapping of Mars. J. Geophys. Res. 106, E10, 23689-23722.

Smith, D.E., Zuber, M.T., Jackson, G.B., Cavanaugh, J.F., Neumann, G.A., Riris, H., Sun, X., Zellar, R.S., Coltharp, C., Connelly, J., Katz, R.B., Kleyner, I., Liiva, P., Matuszeski, A., Mazarico, E.M., McGarr, J.F., Novo-Gradac, A.-M., Ott, M.N., Peters, C., Ramos-Izquierdo, L.A., Ramsey, L., Rowlands, D.D., Schmidt., S., Scott, V.S., Shaw, G.B., Smith, J.C., Swinski, J.-P., Torrence, M.H., Unger, G., Yu, A.W., Zagwodzki, T.W., 2010. Lunar Orbiter Laser Altimeter on the Lunar Reconnaissance Orbiter Mission. Space Science Reviews 150, 209-241.

Smith, E.I., 1976. Comparison of the Crater Morphology-Size Relationship for Mars, Moon, and Mercury. Icarus 28, 543-550.

Solomon, S. C. and J. Chaiken, 1976. Thermal Expansion and Thermal Stress in the Moon and Terrestrial Planets: Clues of Early Thermal History, Proc. LPSC 7, 3229-3243.

Solomon, S. C., R. L. McNutt Jr., T. R. Watters, D. J. Lawrence, W. C. Feldman, J. W. Head, S. M. Krimigis, S. L. Murchie, R. J. Pillips, J. A. Slavin, M. T. Zuber, 2008. Return to Mercury: A global perspective on MESSENGER's first Mercury flyby, Science, 321, 59, DOI:10.1126/science.1159706.

Solomon, S.C., Head, J.W., 1979. Vertical movement in mare basins: Relation to mare emplacement, basin tectonics and lunar thermal history. J. Geophys. Res. 84, 1667–1682.

Solomon, S.C., Head, J.W., 1980. Lunar mascon basins: Lava filling, tectonics, and evolution of the lithosphere. Rev. Geophys. Space Phys. 18, 107–141.

Stein, R.S., 1999. The role of stress transfer in earthquake occurrence. Nature 402, 605-609.

Strom, R. G., N. J. Trask, J. E. Guest, 1975. Tectonism and Volcanism on Mercury, JGR 80, 2478-2507.

Toda, S., R. S. Stein, K. Richards-Dinger, S. Bozkurt, 2005. Forecasting the evolution of seismicity in southern California: Animations built on earthquake stress transfer, JGR B05S16, doi:10.1029/2004JB003415.

Tornabene, L.L., Ling, V., Osinski, G.R., Boyce, J.M., Harrison, T.N., McEwen, A.S., 2013. A Revised Global Depth-Diameter Scaling Relationship for Mars Based on Pitted Impact Melt-Bearing Craters. LPSC 44, Abstract #2592.

Tornabene, L.L., Moersch, J.E., McSween, H.Y., Jr., McEwen, A.S., Piatek, J.L., Milam, K.A., Christensen, P.R., 2006. Identification of large (2-10) km rayed craters on Mars in THEMIS thermal infrared images: Implications for possible Martian meteorite source regions. J. Geophys. Res. 111, E10006. doi:10.1029/2005JE002600.

Tornabene, L.L., Osinski, G.R., McEwen, A.S., Boyce, J.M., Bray, V.J., Caudill, C.M., Grant, J.A., Hamilton, C.W., Mattson, S., Mouginis-Mark, P.J., 2012. Widespread crater-related pitted materials on Mars: Further evidence for the role of target volatiles during the impact process. Icarus, 220(2), 348-368.

Tran T., M. R. Rosiek, R. A. Beyer, S. Mattson, E. Howington-Kraus, M. S. Robinson, B. A. Archinal, K. Edmundson, D. Harbour, E. Anderson, and the LROC Science Team, 2010. Generating Digital Terrain Models Using LROC NAC Images, ASPRS/CaGIS specialty Conference.

Trask, N.J., 1971. In Geologic Comparison of Mare Materials in the Lunar Equatorial Belt, Including Apollo 11 and Apollo 12 Landing Sites. Vol. 750-D D138-D144 (US Geol. Survey Prof. Paper).

Turcotte, D. L., and G. Schubert, 1996. Geodynamics: Application of Continuum Physics to Geological Problems, 450 pp., John Wiley, New York, 1982.

Watters T. R., 2003. Thrust faults along the dichotomy boundary in the eastern hemisphere of Mars, JGR 108, doi:10.1029/2002JE001934.

Watters, T. R., 1991. Origin of Periodically Space Wrinkle Ridges on the Tharsis Plateau of Mars, JGR 96, 15599-15616.

Watters, T. R. and F. Nimmo, 2010. The Tectonics of Mercury, Planetary Tectonics, Cambridget University Press, edited by T. R. Watters and R. A. Schutlz, pp. 15-80.

Watters, T. R. and M. S. Robinson, 1999. Lobate Scarps and the Martian Crustal Dichotomy, JGR 104, 18981-18990.

Watters, T. R. and R. A. Schultz, 2002. The Fault Geometry of Planetary Lobate Scarps: Listric Versus Planar, LPSC 33, Abs. #1668.

Watters, T. R., M. S. Robinson, A. C. Cook, 1998. Topography of Lobate Scarps on Mercury: New Constraints on the Planet's Contraction, Geology 26, 991-994.

Watters, T. R., P. C. Thomas, M. S. Robinson, 2011. Thrust faults and the near-surface strength of asteroid 433 Eros, Geophys. Res. Let. 38, L02202, doi:10.1029/2010GL045302.

Watters, T. R., R. A. Schultz, M. S. Robinson, 2000. Displacement-Length Relations of Thrust Faults Associated with Lobate Scarps on Mercury and Mars: Comparison with Terrestrial Faults, Geophys. Res. Let. 27, 3659-3662.

Watters, T. R., R. A. Schultz, M. S. Robinson, A. C. Cook, 2002. The Mechanical and Thermal Structure of Mercury's Early Lithosphere, Geophys. Res. Let. 29, doi:10.1029/2001GL014308.

Watters, T. R., S. C. Solomon, M. S. Robinson, J. W. Head, S. L. André, S. A. Hauck II, S. L. Murchie, 2009. The Tectonics of Mercury: the View after MESSENGER's First Flyby, Earth and Planetary Science Letters 285, 283-296.

Watters, T.R., 1988. Wrinkle ridge assemblages on the terrestrial planets. J. Geophys. Res. 93, 10236–10254.

Watters, T.R., 1992. A system of tectonic features common to Earth, Mars, and Venus. Geology 20, 609–612.

Watters, T.R., 2004. Elastic dislocation modeling of wrinkle ridges on Mars. Icarus 171, 284–294.

Watters, T.R., Robinson, M.S., Banks, M.E., Tran, T., Denevi, B.W., 2012. Recent extensional tectonics on the Moon revealed by the Lunar Reconnaissance Orbiter Camera. Nature Geosci. 5, 181-185.

Watters, T.R., Robinson, M.S., Beyer, R.A., Banks, M.E., Bell, J.F., Pritchard, M.E., Hiesinger, H., van der Bogert, C.H., Thomas, P.C., Turtle, E.P., Williams, N.R., 2010. Evidence of recent thrust faulting on the Moon revealed by the Lunar Reconnaissance Orbiter Camera. Science 329, 936-940.

Watters, T.R., Robinson, M.S., Collins, G.C., Banks, M.E., Daud, K., Williams, N.R., 2015. Global thrust faulting on the Moon and the influence of tidal stresses. Geology 43, 10, 851-854.

Watters, T.R., Johnson, C.L., 2010. Lunar tectonics. In: Watters, T.R., Schultz, R.A. (Eds.), Planetary Tectonics. Cambridge University Press, Cambridge, UK, 121–182.

Weber, R. C., B. G. Bills, C. L. Johnson, 2009. Constraints on Deep Moonquake Focal Mechanisms through Analyses of Tidal Stress, JGR 114, E05001.

Whitaker, E.A., 1981. The lunar Procellarum basin. In: Schultz, P.H., Berrill, R.B. (Eds.), Multi-ring Basins. Proc. Lunar Planet. Sci. Conf. 12A, 105-111.

White, J.D.L., Ross, P.-S., 2011. Maar-Diatreme Volcanoes: A Review. J. Volc. Geotherm. Res. 201, 1-29.

Whitford-Stark, J.L., 1981. Modification of multi-ring basins – the Imbrium model. In: Schultz, P.H., Berrill, R.B. (Eds.), Multi-ring Basins. Proc. Lunar Planet. Sci. Conf. 12A, 113-124.

Whitford-Stark, J.L., 1990. The volcanotectonic evolution of Mare Frigoris. Proc. Lunar Planet. Sci. Conf. 20, 175-185.

Wieczorek, M.A., Neumann, G.A., Nimmo, F., Kiefer, W.S., Taylor, G.J., Melosh, H.J., Phillips, R.J., Solomon, S.C., Andrews-Hanna, J.C., Asmar, S.W., Konopliv, A.S., Lemoine, F.G., Smith, D.E., Watkins, M.M., Williams, J.G., Zuber, M.T., 2013. The crust of the Moon as seen by GRAIL. Science 339, 671-675.

Wilcox, B. B., M. S. Robinson, P. C. Thomas, B. R. Hawke, 2005. Constraints on the Depth and Variability of the Lunar Regolith, Meteoritics and Plan. Sci. 40, 695-710.

Wilhelms, D.E., 1987. The Geologic History of the Moon. Washington, DC: U.S. Government Printing Office.

Williams, N.R., Watters, T.R., Pritchard, M.E., Banks, M.E., Bell, J.F., 2013. Fault dislocation modeled structure of lobate scarps from Lunar Reconnaissance Orbiter Camera digital terrain models. J. Geophys. Res. 118, 224-233.

Wohletz, K. H., 1986. Explosive Magma-water Interactions: Thermodynamics, Explosion Mechanics, and Field Studies. Bull. Volc. 48, 245-264.

Wohletz, K.H., Sheridan, M.F., 1983. Martian Rampart Crater Ejecta: Experiments and Analysis of Melt-Water Interaction. Icarus 56, 15-37.

Wojtal, S. F., 1996. Changes in Fault Displacement Populations Correlated to Linkage Between Faults, J. Struct. Geol., 18, 265–279, doi:10.1016/S0191-8141(96)80049-6.

Wood, C.A., Head, J.W., Cintala M.J., 1978. Interior Morphology of Fresh Martian Craters: The Effects of Target Characteristics. Proc. Lunar Planet. Sci. Conf. 9, 3691-3709.

Xiao, Z., Komatsu, G., 2013. Impact craters with ejecta flows and central pits on Mercury. Plan. Space Sci.. doi:10.1016/j.pss.2013.03.015.

Xiao, Z., Zeng, Z., Komatsu, G., 2014. A global inventory of central pit craters on the Moon: Distribution, morphology, and geometry. Icarus 227, 195-201.

Zieg, M.J., Marsh, B.D., 2005. The Sudbury Igneous Complex: Viscous emulsion differentiation of a superheated impact melt sheet. Geological Society of America Bulletin, 117(11-12), 1427-1450.

Zuber, M.T., Smith, D.E., Watkins, M.M., Asmar, S.W., Konopliv, A.S., Lemoine, F.G., Melosh, H.J., Neumann, G.A., Phillips, R.J., Solomon, S.C., Wieczorek, M.A., Williams,

J.G., Goossens, S.J., Kruizinga, G., Mazarico, E., Park, R.S., Yuan, D.-N., 2013. Gravity field of the Moon from the Gravity Recovery and Interior Laboratory (GRAIL) mission. Science 339, 668-671.

APPENDIX A

STATEMENT OF PUBLICATION COAUTHOR APPROVALS

Chapter 1 has been submitted for publication and is under peer review at the time of dissertation submission. Chapter 2 has been peer-reviewed and published in the *Journal of Geophysical Research*, volume 118, pages 224-233. Chapter 3 has been peer-reviewed and published in the journal *Icarus*, volume 252, pages 175-185. I, Nathan Williams, affirm that I am the principal author and that all subsequent coauthors approve of the publication of these works.